



Charge Transport and Recombination in Bulk Heterojunction Plastic Solar Cells

Dissertation zur Erlangung des akademischen Grades

Doctor Technicae

im *Doktoratsstudium der technischen Wissenschaften*

Angefertigt *am Linzer Institut für Organische Solarzellen*

Eingereicht von:

Dipl. Ing. Attila Janos Mozer

Betreuung:

o. Univ. Prof. Mag. Dr. Niyazi Serdar Sariciftci

a. Univ. Prof. Mag. Dr. Helmut Neugebauer

Beurteilung:

o. Univ. Prof. Mag. Dr. Niyazi Serdar Sariciftci

ao. Univ. Prof. Dr. Wolfgang Hei

Linz, November 2004

Eidesstattliche Erklärung

Ich erkläre an Eides statt, dass ich die vorliegende Dissertation selbstständig und ohne fremde Hilfe verfasst, andere als die angegebenen Quellen und Hilfsmittel nicht benutzt bzw. die wörtlich oder sinngemäß entnommenen Stellen als solche kenntlich gemacht habe.

Linz, November 2004.

Attila Janos Mozer

Die vorliegende Doktorarbeit entstand zwischen January 2002 und November 2004 am Linzer Institute für Organische Solarzellen der Technisch-Naturwissenschaftlichen Fakultät der Universität Linz unter Betreuung von Prof. N. S. Sariciftci und Dr. Helmut Neugebauer.

Abstract

Charge carrier mobility has been determined in conjugated polymers and bulk heterojunction solar cells using the time of flight (ToF), charge carrier extraction by linearly increasing voltage (CELIV) and the novel photo-CELIV technique. The intercorrelated properties of molecular structure – morphology – charge transport property have been investigated using UV-vis spectroscopy, photoluminescence and ToF experiments in a series of regioregular MDMO-PPVs (poly-[2-(3,7-dimethyloctyloxy)-5-methyloxy]-*p*-phenylene vinylene). It is demonstrated that increasing the regioregularity of conjugated polymers is a successful way to improve charge carrier mobility of these compounds, which is utilized in fabrication of bulk heterojunction solar cells with improved power conversion efficiency.

Negative electric field dependence of mobility has been observed in a regioregular poly(3-hexylthiophene) studied by the ToF and the CELIV technique. The comparative study revealed that these two principally different transient conductivity techniques are mutually consistent, and that the observed negative electric field dependence of mobility is not an experimental artifact, but an intrinsic property of the materials studied. Finally, the novel technique of photoinduced charge extraction by linearly increasing voltage (photo-CELIV) has been introduced to simultaneously determine the mobility (μ) and lifetime (τ) of the photogenerated charge carriers in bulk heterojunction solar cells. The measured μ and τ values are incorporated into a simple one diode model, which can qualitatively describe the measured current density versus voltage curves of bulk heterojunction solar cells with varying active layer thickness.

Preface

The research work presented in this thesis was carried out at the Linz Institute for Organic Solar Cells (LIOS) during the period January 2002 – November 2004.

I thank my supervisor Professor N. Serdar Sariciftci for giving my work continuous inspiration, support and criticism. I also thank Assistant Professor Helmut Neugebauer for fruitful discussions and for his strict and thorough manuscript readings. This work would not have been possible without collaborations with the coworkers of the LIOS group and Konarka Austria. I thank especially the senior students Markus Scharber and Antonio Cravino, fellow PhD students Gebi Matt, Harald Hoppe and Christoph Winder for introducing me to their work. The materials used for the studies were prepared by the group of Dirk Vanderzande and Laurence Lutsen (IMOMEC, Belgium), Marinella Catellani and Silvia Luzzati (ISMAL, Milan), and John Reynolds (Univ. of Florida). I also thank Vladimir Dyakonov and the members of the research training network EUROMAP.

I am grateful for Professor Henrik Stubb, Ronald Österbacka, Gytis Juška, Almantas Pivrikas for introducing me to CELIV and photo-CELIV technique and Markus Westerling for the recombination studies. I also thank Professor Heinz Bässler, Vladimir Arkhipov, and Andrey Kadashchuk to help me understanding the various experimental and theoretical aspects of charge transport in conjugated polymers, Roland Resel and Rosina Staneva for performing the XRD studies, Wolfgang Heinz for the help with the PL measurements, and Wim Geens with the FET fabrication and characterization.

Finally, I thank my wife Tomoko Murakami and my parents for their love and support.

Attila Mozer
Linz, November, 2004.

Contents

Eidesstattliche Erklärung	ii
Abstract	iii
Preface	iv
Table of Contents	v
1. Introduction.....	1
1.1 Background and Motivation	1
1.2 Bulk Heterojunction Solar Cells	4
1.2.1 Operational principles	4
1.2.2 Charge transport and recombination	6
1.2.3 Morphology-property relations	8
1.2.4 Improving the photon harvesting	11
1.3 Theory of Charge Transport in Organic Semiconductors	11
2. Experimental Setups and Materials.....	17
2.1 Mobility Techniques	17
2.2 Preparation of Bulk Heterojunction Solar Cells	21
2.3 UV-vis Absorption and Photoluminescence (PL).....	22
2.4 Materials	23
2.4.1 Regioregular MDMO-PPV polymers	23
2.4.2 Polythiophene – anthraquinone “double-cable” copolymers.....	24
2.4.3 Dithienothiophene copolymers	24
2.4.4 PProDot(Hx) ₂	25
3. Charge Transport in Conjugated Polymers.....	27
3.1 Charge Transport in Regioregular MDMO-PPVs	27
3.2 Charge Transport in Regioregular Poly(3-hexylthiophene)	39
3.2.1 Charge carrier mobility investigated by the ToF technique.....	39
3.2.2 Charge carrier mobility investigated by the CELIV technique	46
3.2.3 Temperature dependence of the mobility: A comparison.....	49
3.3 Summary	53

4. Mobility and Recombination in Bulk Heterojunction Solar Cells	54
4.1 Introduction.....	54
4.2 Photo-CELIV Measurements at RT.....	55
4.3 Temperature Dependence Studies.....	61
4.3.1 Delay time dependence of the mobility	61
4.3.2 Charge carrier concentration dependence of the mobility	68
4.3.3 Voltage (field) dependence of the mobility	72
4.4 Summary	75
5. Bulk Heterojunction Solar Cells.....	77
5.1 Regioregular MDMO-PPVs.....	77
5.2 Thickness Dependence Parameters of Bulk Heterojunction Solar Cells	80
5.3 Polythiophene – anthraquinone “Double-Cable” Copolymers	87
5.4 Dithienothiophene and Dithienothiophene-S,S-dioxide Copolymers.....	88
5.5 PProDot(Hx) ₂	93
6. Summary and Outlook.....	95
References	97
Curriculum Vitae	107

Chapter 1

1. Introduction

1.1 Background and Motivation

The idea of utilizing organic materials for solar energy conversion has been the subject of research for several decades. Organic materials are typically inexpensive, easily processable and their functionality can be tailored by molecular design and chemical synthesis. In 1985 Tang¹ has first demonstrated an organic solar cell exhibiting power conversion efficiency around 1% based on a bilayer-structure of two well known photoconductors Me-Ptcdi (N,N'-dimethyl-perylene-3,4,9,10-dicarboximide) / ZnPc (zinc-phtalocyanine). The photovoltaic effect of that cell was attributed to the efficient charge generation at interface formed between the two organic materials with dissimilar electronic levels.

Since their initial discovery in 1977, conductive polymers gained interest due to their metallic or semiconducting properties accompanied by easy processing and flexibility of common plastics.² The fabrication of the first diodes in 1987 based on a soluble poly(3-hexylthiophene) sandwiched between a transparent conductive oxide and evaporated aluminum contacts marked the beginning of the rapidly expanding field of plastic electronics.³ It is expected that several electronic devices, such as displays based on polymer light emitting diodes,⁴ integrated electronic circuits based on polymer field effect transistors,⁵ and plastic solar cells⁶ will enter the market in applications where flexibility and light weight is desirable ("throw-away electronics").

The most promising candidate of flexible plastic solar cells is based on the bulk heterojunction concept, which consists of an interpenetrating network of a

conjugated polymer and fullerene. Bulk heterojunction solar cells can be prepared by solution processing techniques, such as spin coating, doctor blading,⁷ screen printing⁸ and spray coating.⁹ The various printing technology enables roll-to roll fabrication of large area flexible devices. Although the preparation of bulk heterojunction solar cells is rather simple, the operation principles are complex and their understanding requires interdisciplinary research at different fields of material science.

One of the open questions is the effect of charge carrier mobility on the performance of bulk heterojunction solar cells. More specifically, the three main questions initiated this study were:

1. How to measure charge carrier mobility in bulk heterojunction solar cells?
2. How to correlate the measured mobility values to the microscopic and macroscopic properties of the materials?
3. How to increase the charge carrier mobility in bulk heterojunction solar cells?

To answer these questions systematically, the following strategy was followed, which is also reflected in the organization of this thesis:

1. To install experimental techniques to measure charge carrier mobility in conjugated polymers, and to test the suitability of these techniques to measure charge carrier mobility in bulk heterojunction solar cells.
2. To determine the temperature and electric field dependence of the mobility, and to correlate the measured charge transport properties to the chemical structure and the morphology of the materials by using theoretical models.
3. To introduce novel experimental techniques to determine charge carrier mobility and lifetime in bulk heterojunction solar cells.
4. To fabricate bulk heterojunction solar cells using materials with improved charge transport, and to test the relevance of the measured mobility and lifetime values in comparison with the performance of bulk heterojunction solar cells.

The study of charge transport in conjugated polymers and bulk heterojunction solar cells is the main topic of this thesis. The two most common conjugated polymers

used in bulk heterojunction solar cells were selected for this purpose: i) regiorandom and regioregular MDMO-PPV ii) regioregular poly(3-hexylthiophene) (P3HT).

In addition, the optical and morphological properties and the photovoltaic performance of several other promising materials were studied. These materials have been designed and supplied by the various collaborators, and have been selected to improve some specific parameters of bulk heterojunction solar cells. The materials discussed in this thesis are low band gap polymers for improved light harvesting (PProDot(Hx)₂ and dithienothiophene copolymers (P materials)), and “double-cable” polymers (polythiophene – anthraquinone copolymers).

1.2 Bulk Heterojunction Solar Cells

1.2.1 Operational principles

The efficiency of free charge carrier generation as a prerequisite for a photovoltaic effect is typically very low in organic materials due to the small mean free path (low mobility) of charge carriers, which is smaller than the Coulomb radius $r_c = e^2 / 4\pi\epsilon\epsilon_0 kT$ (small dielectric constant).¹⁰ Therefore primary photoexcitations are strongly bound neutral excited states (binding energy in excess of 0.5 eV). The generation of free charge carriers requires excess energy gained by for *e.g.*, electron transfer from the donor containing the excitation to lower lying molecular orbital of the electron acceptor moieties or to interfaces. The nature of primary photoexcitations in pristine conjugated polymers is still under discussions.^{11,12} Steady state and transient photoconductivity experiments showed that the yield of charge carrier generation in conjugated polymers can be significantly improved in their blends with a strong electron acceptor buckminsterfullerene.¹³ Various optical techniques, such as light induced electron spin resonance (LESR),^{14,15} photoinduced absorption (PIA),¹⁶ transient absorption (TA)¹⁷ and photoinduced absorption detected magnetic resonance¹⁸ verified that the charge carriers are generated via photoinduced electron transfer between the photoexcited state of the conjugated polymer and the fullerene with a quantum yield approaching unity. The photogenerated charges are metastable with lifetimes up to several microseconds at room temperature.

An immediate realization was that the application of selective electrical contacts to the above described system, an efficient photovoltaic device may be fabricated. First, bilayer devices of spin coated MEH-PPV layer and evaporated C60 layer sandwiched between ITO coated glass and Aluminum have been presented.¹⁹ These flat hetero-junction devices exhibit 4 orders of magnitude rectification in the current vs. voltage curves in the dark, and a few $\mu\text{A cm}^{-2}$ short circuit current and 0.5 V open circuit voltage under $\sim 1 \text{ mW cm}^{-2}$ monochromatic (514 nm) illumination through the ITO side. The spectral response of the diodes was minimal at the maximum of the absorption of the MEH-PPV layer, which showed that the majority

of photocurrent in such bilayer devices is generated within the thin interface between the MEH-PPV and C60 heterojunction. The real breakthrough was achieved by creating interpenetrating network of the electron donor and electron acceptor materials extending the interface area over the whole photoactive layer resulting in a device architecture often referred to as the bulk heterojunction.⁶

The concept of a bulk heterojunction is shown in Fig. 1.1. The schematic band structure at short circuit conditions displaying the highest occupied molecular orbital (HOMO) and the lowest unoccupied molecular orbital (LUMO) of the materials and the work function of the electrodes are also illustrated.

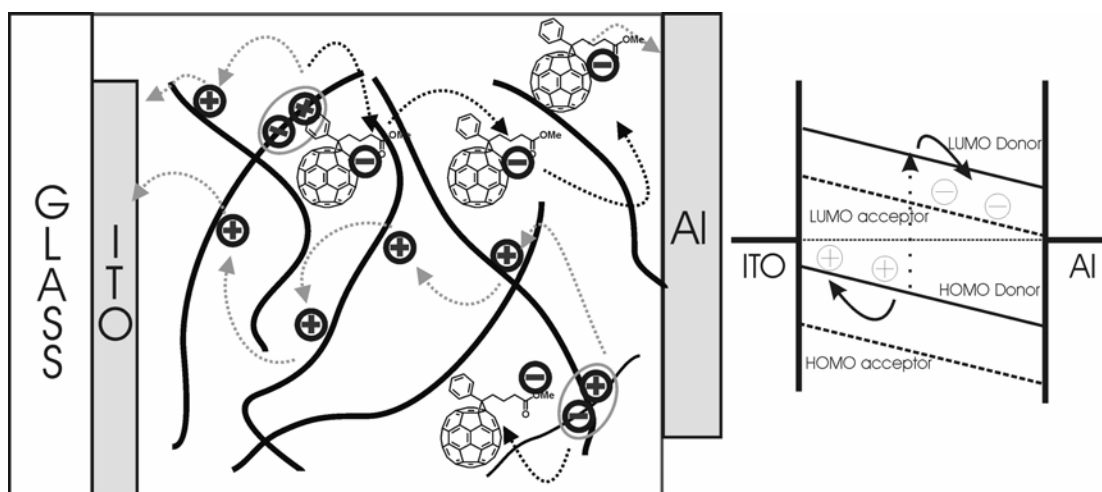


Figure 1.1: Schematic illustration of a bulk heterojunction based on the interpenetrating network of a conjugated polymer and PCBM. The electronic levels relevant to the device performance are also displayed.

The charge carriers are generated by photoinduced electron transfer from the LUMO of the electron donor (conjugated polymer) to the LUMO of the electron acceptor (PCBM). For efficient charge generation, an exciton photogenerated anywhere in the blend has to reach an acceptor interface within its lifetime; therefore the magnitude of the maximum allowed phase separation is determined by the exciton diffusion length. For intimately mixed blends, experiments showed that only a few weight% of the electron acceptor is sufficient to quench virtually all excitations.²⁰ For efficient photovoltaic devices, however, the created charge carriers need to be transported to the corresponding electrodes within their respective lifetimes, which depends on the charge carrier mobility of the materials.

As a last step, charge carriers are extracted from the device through two selective contacts. A transparent indium thin oxide (ITO) coated glass matching the

HOMO level of the conjugated polymer (hole contact) is used on the illumination side, and evaporated thin Lithium Fluoride / Aluminum metal contact matching the LUMO of PCBM (electron contact) is used on the other side. In the state-of-the-art devices, a thin (100 nm) hole injection layer, a highly doped PEDOT-PSS interfacial layer is used, which also serves to smoothen the surface of the ITO and to increase device stability.

Although the primary act of photogeneration has been studied in details by various optical techniques, the transport of the photogenerated charge carriers and their recombination has not been fully understood. This is partially due to lack of straightforward experimental methods to determine charge carrier mobility in operational devices.

1.2.2 Charge transport and recombination

The drift distance of the charge carriers photo-generated anywhere within the active layer is given as $l_d = \mu \times \tau \times E$, where μ is the mobility, τ is charge carrier lifetime and E is the electric field, which limits the maximum thickness of the active layer ($d_{\max} < l_d$). This equation assumes that the charge carriers are electric field driven.²¹ In order to reach competitive power conversion efficiencies of organic solar cells, a short circuit current density on the order of $\sim 10 \text{ mA cm}^{-2}$ is necessary. Due to the rather low mobility of organic materials, high concentration of photogenerated charge carriers is required to reach this short circuit current density, *e.g.* $n \sim 10^{16} \text{ cm}^{-3}$ if $\mu = 10^{-4} \text{ cm}^2 \text{ V}^{-1} \text{ s}^{-1}$. High charge carrier concentration generally leads to increased bimolecular recombination resulting in short lifetimes ($\tau(t) = [\beta n(t)]^{-1}$) and consequently, short drift and diffusion distances. Moreover, charge carrier mobility and the lifetime of the charge carriers are not independent in most organic materials. The bimolecular recombination coefficient of a Langevin-type recombination typical for low mobility organic materials is written as $\beta_L = e(\mu_e + \mu_h) / \epsilon \epsilon_0$, where μ_e (μ_h) is the electron (hole) mobility and e , ϵ , ϵ_0 are the elementary charge and the dielectric constants of the material and vacuum, respectively. The important questions are, therefore, how to measure charge carrier mobility and lifetime simultaneously in bulk heterojunction solar cells, and how μ and τ are correlated within the interpenetrating network of the electron donor and electron acceptor materials.

Charge carrier mobility in bulk heterojunction solar cells has been studied using a time of flight (ToF) technique,²² or calculated from the transfer characteristic of a field effect transistor (FET).²³ These results showed that the electron mobility (PCBM phase) and the hole mobility (conjugated polymer phase) in the photoactive blend is fairly balanced, which is counterintuitive to experiments performed on the pristine materials. Space charge limited current measurements showed that the mobility of injected holes in the pure MDMO-PPV thin films is several orders of magnitude lower than injected electrons in PCBM thin films.²⁴ Recent ToF studies performed on MDMO-PPV: PCBM (1:2) blends concluded that the mobility is unbalanced, the electron mobility being at least 2 orders of magnitude higher than the hole mobility.²⁵ The apparent discrepancy between the above examples shows that the straightforward experimental determination of mobility using currently available methods is problematic.

The recombination dynamics of the photogenerated charge carriers in the blend of electron donor and electron acceptor materials has been studied by various optical techniques, for *e.g.*, light induced electron spin resonance (LESR),²⁶ photoinduced absorption (PIA),²⁷ photoinduced reflection-/absorption (PIRA)²⁸ and transient absorption (TA).²⁹ In these optical techniques, the charge carrier-induced changes of the absorption of the films ($-\Delta T$) is monitored either by a modulation technique (PIA) or followed in real time (TA). The recorded signals are often very dispersive, especially at low temperatures and low frequencies or long timescales. Although the nature of these long-lived photoexcitations is of practical importance, optical techniques cannot directly distinguish between mobile or deeply trapped, immobile charges carriers. For *e.g.*, transient absorption experiments in the blend MDMO-PPV:PCBM showed power law decay of the $-\Delta T/T$ signal with an exponent of $\alpha=0.4$ in the μs to ms timescale.³⁰ Power law decay indicates a broad distribution of lifetimes due to strong dispersion. Moreover, optical techniques are typically applied on the films without electrodes; therefore operational devices cannot be easily studied. A major limitation of optical techniques is that the effect of electrodes and external electric fields cannot be easily studied.

Information on the recombination processes in operational bulk heterojunction solar cells is often obtained indirectly by the incident light intensity dependence of the short circuit current.³¹ Scaling factor close to 1 indicates that the short circuit current

is not limited by second-order recombination processes, such as bimolecular recombination. In the latter case, exponent close to 0.5 is expected. Unfortunately, this experiment provides little information on any first order recombination processes, which scales linearly with light intensity. Examples for such first order recombination processes are a trap mediated (quasi-) monomolecular recombination, or recombination due to accumulated space charge.

From the above description it is evident that novel techniques are necessary to study charge carrier mobility and recombination in operational bulk heterojunction solar cells.

1.2.3 Morphology-property relations

The power conversion efficiency of bulk heterojunction solar cells based on MDMO-PPV:PCBM (1:4) weight percent mixture could be improved from approximately 1 % (AM 1.5) to 2.5 % by simply changing the solvent from which the active layer has been cast.³² Atomic force microscopy (AFM) investigations showed that rather large, *i.e.* 100 – 200 nm clusters are formed in the toluene cast films, meanwhile a smooth surface morphology was observed for the chlorobenzene cast films. Transmission electron microscopy (TEM) and AFM studies³³ assigned the large clusters to a PCBM-rich phase. In a more detailed study, the phase separation in MDMO-PPV:PCBM blends with increasing PCBM content spin coated from chlorobenzene was followed in all three dimensions by a combination of AFM, TEM, and depth profiling experiments.³⁴ The study showed very smooth films by AFM and no observable contrast in the TEM experiments up to 50 - 60% PCBM content. The film surface is increasingly uneven at higher PCBM loads (>67 %), and correspondingly, two phases in the TEM images could be identified. The darker phase, which is growing with increasing PCBM content, was identified as a rather pure PCBM phase similarly to [33].

Fine details of the nano-scale morphology in the photoactive layer using AFM and scanning electron microscopy (SEM) has been recently reported by Hoppe et al.³⁵ The SEM images obtained for CB cast, 1:2, 1:4 and 1:6 ratio by weight MDMO-PPV:PCBM films are compared in Fig. 1.2 a, b, and c, respectively. In all cases, small (20-30 nm) bright nano-spheres embedded in a rather uniform matrix are observed,

except for the 1:6 films, in which larger clusters are also observed. These large clusters are clearly visible, and their size is dependent on the PCBM load in films cast from toluene (Fig. 6 d), therefore assigned to PCBM phase. The small bright spheres, however, can be found in all films studied, for *e.g.*, in the “thin skin” surrounding the large clusters in the toluene cast films, or uniformly distributed in the chlorobenzene cast films. The authors attribute the bright nano-spheres to an MDMO-PPV phase, in which the polymer chains attain a coiled conformation. This notion is supported by annealing experiments, in which the contrast between the different phases is improved due to the tendency of PCBM to diffuse and crystallize. Large holes appear instead of the PCBM clusters indicating the diffusive motion of PCBM towards crystallization centers. Interestingly, however, the small spheres remain at the same position. Consequently, the PL of the MDMO-PPV reappears upon annealing, which strongly support the assignment of the nano-spheres to the MDMO-PPV polymer.

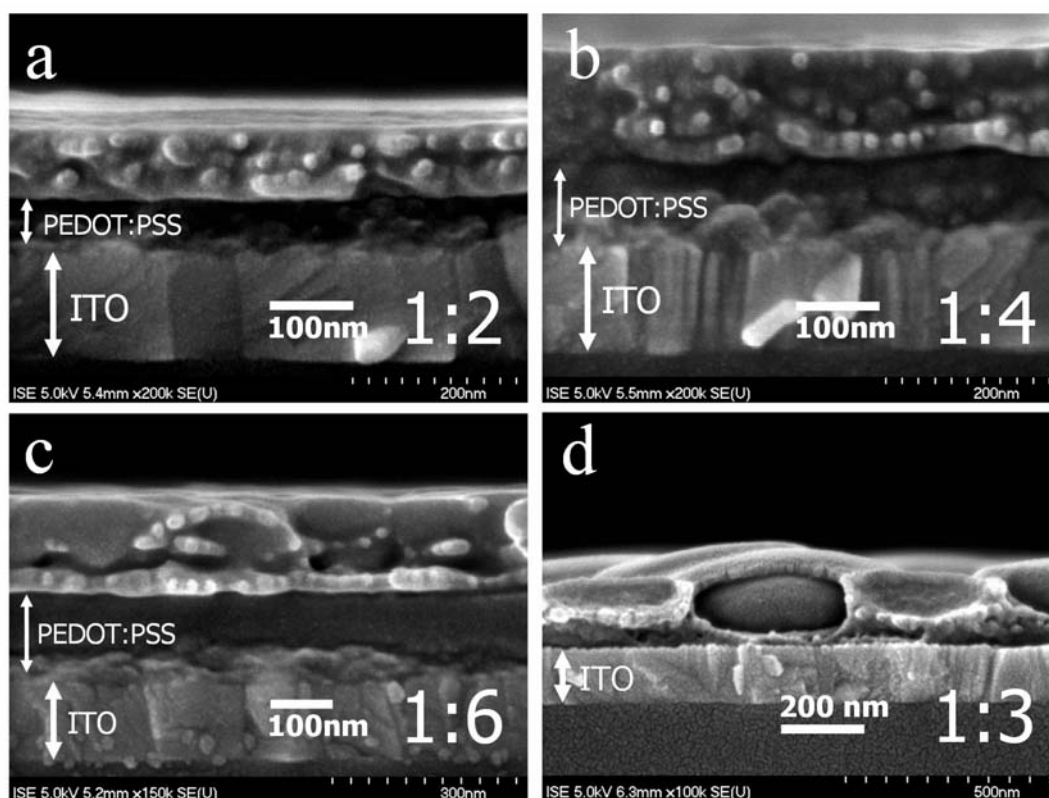


Figure 1.2 a,b,c: Cross section SEM images of MDMO-PPV:PCBM 1:2, 1:4, 1:6 weight ratio films spin coated from chlorobenzene solutions; d: 1:3 weight ratio MDMO-PPV:PCBM films spin coated from toluene solutions (images by H. Hoppe).

Another interesting finding of that paper is related to the dependence of the morphology on the preparation method as well as the total concentration of the

organic materials. Larger scale phase separation is observed in the films using more concentrated solutions, which is attributed to the longer drying times of thicker films. The effect of drying conditions on the morphology has been observed in other works,³⁶ and can influence the results of spectroscopic investigations.

The above morphology studies demonstrate that although the preparation of bulk heterojunction solar cells is very simple, the proper control of the processing parameters is complex, and involves detailed studies of the influence of many factors, *e.g.* the choice of solvent, the concentration of the solution, the weight ratio of the active components, *etc.* The optimum set of parameters may obviously change with different material combinations. In order to achieve control of the morphology at the molecular level, the concept of “double-cable” polymers has been introduced (see Fig. 1.3).³⁷ These latter materials are electron donor conjugated polymers carrying a number of adjacent electron acceptor moieties as covalently linked substituents. It is expected that the electron created by photoinduced electron transfer will travel by hopping between the acceptor moieties; meanwhile the rather high on-chain hole mobility as well as subsequent interchain hopping will transport the positive charge. Ideally, phase separation in these materials is prevented, or, in other words, the interface between the electron acceptor (n-type) and electron donor (p-type) materials is brought down to the molecular level. As such, double cable polymers can be viewed as molecular heterojunctions. Major criterion for the application of these materials in photovoltaic elements is the absence of ground state interaction between the electron donor and acceptor moieties (the “cables” must not short). This can be achieved by introducing an insulating spacer between the n-type and p-type “cable”. The spacer may also increase the solubility of the macromolecule; however, its length must be appropriate not to hinder photoinduced electron transfer.³⁸

Most “double-cable” polymers contain covalently linked fullerene moieties. Unfortunately, it is difficult to achieve significant load of fullerenes due to reduced solubility of the “double-cable” polymer. The results obtained for the well soluble polythiophene – anthraquinone copolymers are discussed in chapter 5.3.

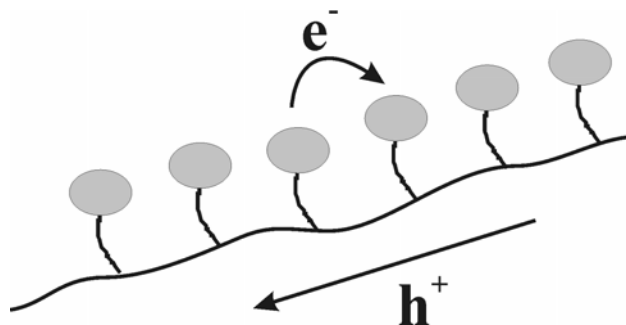


Figure 1.3: Ideal representation of “double-cable” polymers. The charge carriers generated by photoinduced charge transfer can be transported within one molecule, therefore viewed as a “molecular heterojunction”.

1.2.4 Improving the photon harvesting

The absorption of the MDMO-PPV:PCBM blend is limited in spectral regions where the spectral photon flux from the sun is more intense (~ 1.8 V).³⁹ The limited light harvesting of bulk heterojunction solar cells is their most important deficiency, and although some improvements are expected by incorporating for *e.g.*, light trapping, anti reflection coating or solar light concentration elements, the real breakthrough towards improved power conversion efficiency can only be achieved using novel materials with optical absorption at the longer wavelength range. The onset of the absorption of the conjugated polymer corresponds to the π - π^* energy gap. To improve the spectral sensitivity of bulk heterojunction solar cells, materials with lower π - π^* band gaps are required. The photovoltaic properties of two novel low band gap polymers, namely polydithienothiophene copolymers (P materials) and PProDot(Hx)₂ are discussed in Chapter 5.4 and 5.5, respectively.

1.3 Theory of Charge Transport in Organic Semiconductors

The interest in experimental and theoretical aspects of charge transport in organic disordered materials is dated back to the development of organic photoconductors for xerography and printing technology.⁴⁰ In these applications, inorganic chalcogenide glasses, such as As, S, Se, Te and related alloys, and organic amorphous materials, such as molecularly doped polymers and amorphous molecular glasses were studied as charge generation and transport layers. The main requirements

for xerographic applications are the low dark conductivity, high charge carrier mobility and the absence of charge carrier trapping. Due to their specific application, the time of flight technique and a xerographic discharge technique were the most commonly used to study the charge transport properties of these amorphous materials. The results showed that in contrary to crystalline materials,⁴¹ charge carrier mobility values are typically lower, and exhibit strong temperature and electric field dependence. The pioneering work of Scher and Montroll has introduced a phenomenological model to explain the frequently observed universality of the shape of the recorded photocurrent transients according to:⁴²

$$j(t) \sim t^{-(1-\alpha_i)}, \quad t < t_{tr} \quad (1.1)$$

$$j(t) \sim t^{-(1+\alpha_j)}, \quad t > t_{tr} \quad (1.2)$$

where α is a parameter related to the dispersivity of the transients, and t_{tr} is the transit time defined as the intersect of the straight lines in a logarithm photocurrent versus logarithm time plots. The prediction of that formalism is that the slopes prior ($1-\alpha_i$) and after ($1+\alpha_j$) the transit time should sum up to 2, and the transients recorded at various electric fields and thicknesses can be superimposed when normalized to t_{tr} .

The temperature and electric field dependence of mobility in molecularly doped polymers has been frequently analyzed in the framework of Gill's model⁴³ according to:

$$\mu(T, E) = \mu_0 \exp \left[- \left(\frac{\Delta - \beta_{PF} E^{1/2}}{k_B T_{eff}} \right) \right] \quad (1.3)$$

where $T_{eff}^{-1} = T^{-1} - T_0^{-1}$, T [K] is the temperature, Δ [eV] is the zero field activation energy, β_{PF} [$\text{eV}(\text{Vcm}^{-1})^{-1/2}$] is the Poole-Frenkel coefficient, T_0 is the temperature at which the Arrhenius plots of mobility at various electric fields intercept, μ_0 is the mobility at T_0 , and k_B is the Boltzmann constant. The model predicts square root dependence of the log mobility versus the electric field, which is attributed to the reduction of the activation energy barrier for charge carrier hops by $\beta E^{1/2}$ as illustrated in Fig. 1.4.

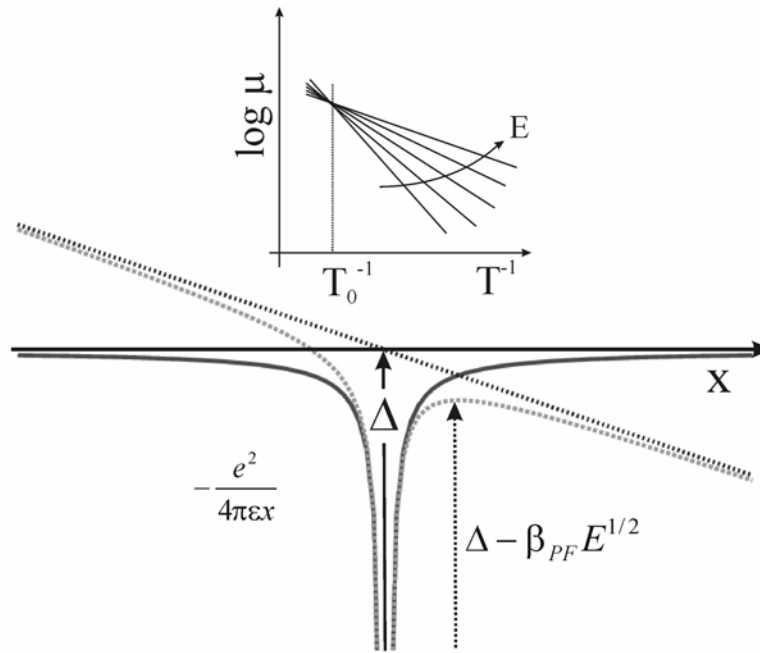


Figure 1.4: The reduction of the activation energy for charge carrier hops by the application of an external electric field according to the Gill's model. The inset shows the predicted temperature dependence of the logarithm of mobility at various electric fields.

Interesting prediction of this model that the mobility at various electric fields should intercept at a temperature T_0 , above which the electric field dependence should change its sign. Such negative electric field dependence of mobility has been observed in several disordered materials, such as molecularly doped polymers^{44, 45} and molecular glasses.⁴⁶ The Gill's model although predicts the occurrence of negative electric field dependence of mobility, it does not discuss the underlying physical nature of it, nor attributes any meaning to T_0 . Although eq. 1.3 was widely used due to its relative simplicity, it failed to account for several properties intrinsic to disordered semiconductors, for *e.g.*, the energetic disorder of the charge transport sites and/or the structural relaxation of charge carriers leading to self-localization (polaronic effects).

The disorder formalism developed by Bässler and coworkers⁴⁷ has been frequently used to analyze the temperature and electric field dependence of mobility in disordered organic materials. This model postulates that the main contribution to the activation energy in disordered organic semiconductors is due to the fluctuation of the site energies, and it neglects polaronic effects. Monte Carlo simulations showed that charge carriers generated initially with random energies tend to relax toward the tail states of a density of states distribution described by a Gaussian distribution.

Disorder formalism uses the master equation of asymmetric hopping rates of the Miller-Abrahams form:⁴⁸

$$v_{ij} = v_0 \exp\left(-2\gamma a \frac{\Delta R_{ij}}{a}\right) \begin{cases} \exp\left(-\frac{\varepsilon_j - \varepsilon_i}{kT}\right) & \varepsilon_j > \varepsilon_i \\ 1; & \varepsilon_j < \varepsilon_i \end{cases} \quad (1.4)$$

where v_{ij} is the hopping rate between site i and j with energy ε_i and ε_j , a is the average lattice distance. The first exponential in eq. 1.4 describes the electronic wavefunction overlap, and the second exponential describes a Boltzmann factor for sites upwards in energy. Eq 1.4 postulates that only charge carrier hops to sites higher in energy are thermally activated, therefore only these jumps are accelerated by the electric field. The rate for downward jumps is 1, which assumes that energy can be always dissipated via the large number of high frequency phonons typical for organic conjugated materials. According to eq. 1.4, a dynamic equilibrium is attained when the number of even lower laying sites is so low, that on average all the jumps will be thermally activated upward jumps. Simulations showed that the mean energy $\langle\varepsilon_\infty\rangle$ of an ensemble of relaxing charge carriers asymptotically approaches a constant value of $-\sigma^2/kT$ below the center of the distribution. The time to reach this quasi-equilibrium is expected to decrease with decreasing temperature as:⁴⁹

$$\frac{t_{rel}}{t_0} = 10 \exp\left[\left(1.07 \frac{\sigma}{kT}\right)^2\right] \quad (1.5)$$

where t_0 is the dwell time of a carrier without disorder, and σ is the width of the Gaussian distribution of states. The temperature and electric field dependence of mobility in quasi-equilibrium conditions is described as:

$$\mu(T, E) = \mu_0 \exp\left[-\frac{2}{3}\left(\frac{\sigma}{kT}\right)^2\right] \exp\left\{C \left[\left(\frac{\sigma}{kT}\right)^2 - \Sigma^2\right] E^{1/2}\right\} \quad (1.6)$$

where Σ is a parameter characterizing positional disorder, μ_0 is a prefactor mobility in the energetically disorder-free system, E is the electric field, and C is a fit parameter. C contains no adjustable parameters; therefore provide a test of the theory. Disorder formalism predicts non-Arrhenius temperature dependence of the mobility,

which has been verified by numerous experiments. Deviations from the temperature dependence predicted by eq. 1.6 have been also observed by the ToF technique, which was attributed to non-dispersive to dispersive (ND→D) transition.⁵⁰ Since the time to reach the quasi-equilibrium level according to eq. 1.5 is increasing faster than the transit time of charge carriers with decreasing temperature, eventually charge carriers without quasi-equilibrium will be probed. The temperature at which the transition (T_c) occurs depends on the energetic disorder parameter, and exhibit sample thickness dependence according to

$$\left(\frac{\sigma}{kT_c}\right)^2 = 44.8 + 6.7 \log d \quad (1.7)$$

where d is a parameter related to the thickness in cm units. The ND→D transition is manifested by the appearance of a kink in the $\log \mu(E=0)$ versus $1/T^2$ plots accompanied by photocurrent transients that no longer exhibit a plateau.

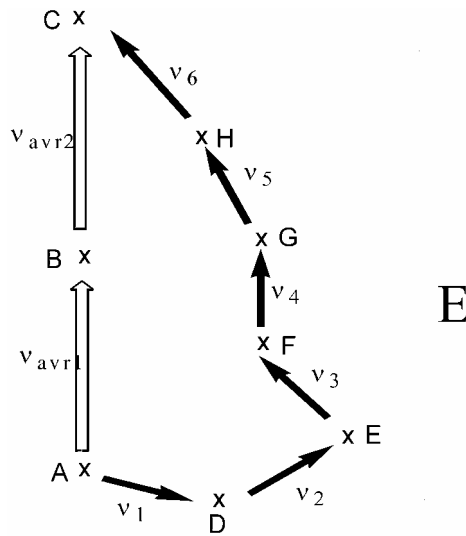


Figure 1.5: The effect of positional disorder on the motion of a charge carrier under an external electric field. The hops from A to C via site B are characterized as “difficult” due to weak electronic coupling. The alternative route via D-E-G-H-C is considered more favorable, yet hops against the electric field (A-D) are gradually diminished with increasing electric fields resulting in negative electric field dependence of the mobility.

According to eq. 1.6, the slope of the electric field dependence of the mobility is decreasing with increasing electric field and may turn to negative when $\sigma/kT < \Sigma$. The negative electric field dependence of mobility is attributed to large positional disorder

equivalent to large fluctuation of the electronic coupling between the charge transport sites. Large positional disorder creates faster routes as well as dead ends for charge carriers executing their random walk. At higher fields, detour routes around such dead ends are gradually diminished resulting in negative electric field dependence of the mobility as illustrated in Fig 1.5.

The disorder formalism has been recently applied to describe the temperature and electric field dependence of mobility in conjugated, semiconducting polymers.^{51,52} The electronic structure of conjugated polymers is quite different than that of the above mentioned inorganic or organic amorphous glasses, or other small π -conjugated molecules. Conjugated polymers can be viewed as one dimensional semiconductors, in which the semiconducting properties are attributed to the extended π -electron systems formed by the π_z electrons of the carbon atoms of the backbone.⁵³ Although microwave conductivity techniques^{54,55} showed that the on-chain mobility can reach very high values, the macroscopic transport properties are controlled by the orders of magnitude slower interchain hopping process. The solubility and processability of conjugated polymers are achieved by attaching side chains to the conjugated backbone. Naturally, the length of the insulating side chain affects the interchain electronic coupling therefore influence mobility, as it is evidenced by the decreasing charge carrier mobility in a series of regioregular polyalkylthiophenes with increasing side chain length.⁵⁶ Furthermore, the regularity of the side chain attachment plays an important role in the solid state morphology and ordering. For *e.g.*, regioregular poly(3-hexylthiophene) (P3HT), in which the solubilizing side chains are attached in a regular pattern forms crystalline phases,⁵⁷ meanwhile regiorandom P3HT is typically amorphous. The electronic properties of these two materials are also quite different. Regioregular P3HT exhibits one of the highest mobility among conjugated polymers in the FET structure, meanwhile mobility in the regiorandom P3HT is 3 to 4 orders of magnitude lower.^{5,58} The effect of side chain substitution on charge carrier mobility was investigated for a series of alkoxy-PPVs in the work of Martens et al.⁵² The charge carrier mobility of the symmetrically substituted OC₁₀C₁₀ PPV is one order of magnitude higher than the asymmetrically substituted, regiorandom MDMO-PPV (also known as OC₁C₁₀ PPV). From temperature and electric field dependence of mobility studies it was concluded that the increased on-chain and interchain disorder is mainly responsible for the lower mobility of regiorandom MDMO-PPV.

Chapter 2

2. Experimental Setups and Materials

2.1 Mobility Techniques

Charge carrier mobility techniques in organic materials can be classified according to *e.g.*, the mode of charge generation (photogenerated, doping induced, electrostatic, or injected by electrical contacts) or as transient or (quasi-) steady state (Table 2.1).

Table 2.1: Experimental techniques used to determine charge carrier mobility.

		<i>Transient</i>	<i>(Quasi-) Steady State</i>
Mode of charge generation	<i>Photo-induced</i>	Time of Flight (ToF) ⁴⁰ Photo-CELIV ⁵⁹	Photoconductivity ⁶⁰ Photo-impedance ⁶¹
	<i>Doping-induced</i>	CELIV ⁶²	Conductivity ^{63,64}
	<i>Electrostatic</i>		Field Effect Transistor ⁶⁵
	<i>Injected (from contacts)</i>	DI SCLC ^{66,67} tr-EL ⁶⁸	SCLC ^{63,69} Time-resolved optical detection ^{70,71}

CELIV: charge extraction by linearly increasing voltage; DI SCLC: dark injection space charge limited current; tr-EL: transient electroluminescence

The time of flight technique (ToF), and the complimentary technique of charge extraction by linearly increasing voltage (CELIV) are used in this study to

measure charge carrier mobility in conjugated polymers, meanwhile the novel photo-CELIV technique is introduced to determine charge carrier mobility and recombination in bulk heterojunction solar cells. The measurement principles and the schematic responses of these transient conductivity techniques are illustrated in Fig. 2.1.

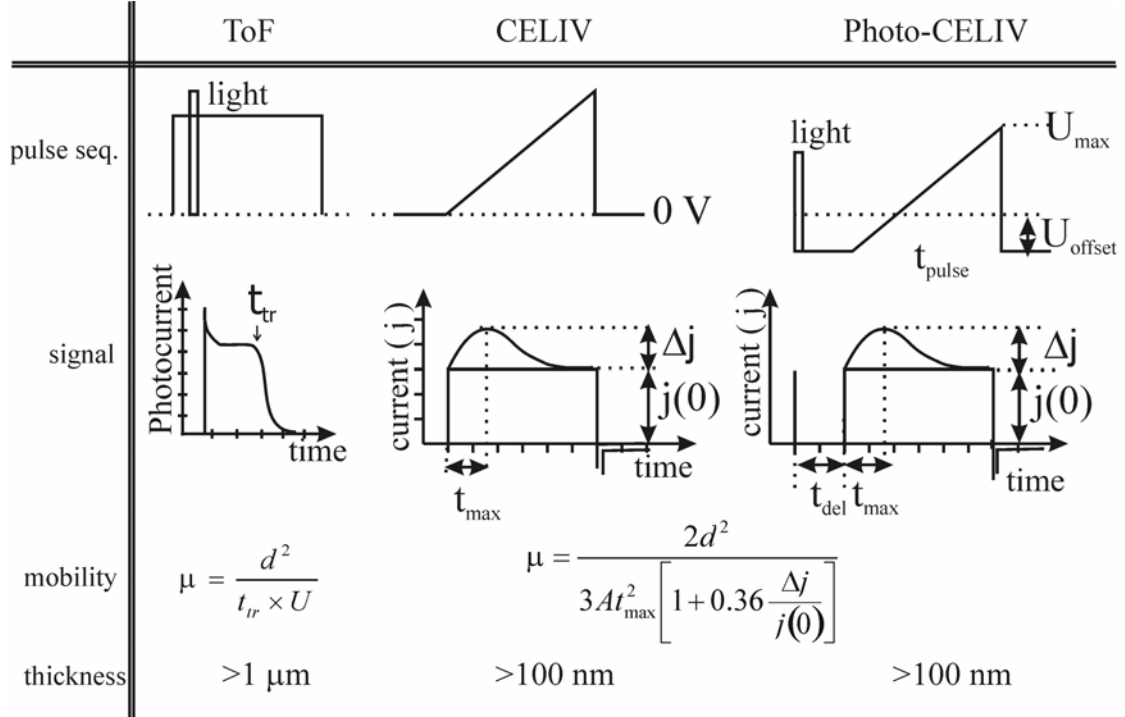


Figure 2.1: The pulse sequence and schematic response of the ToF, CELIV and photo-CELIV technique. The calculation of mobility and the typical thickness of the device are also displayed for comparison.

In the time of flight technique, the transit time (t_{tr}) of a two dimensional sheet of photogenerated charge carriers drifting through a sample of know thickness (d) is determined under an applied external electric field ($E=U/d$). The ToF mobility is then calculated as $\mu=d^2/(U \times t_{tr})$. The condition of surface photogeneration of charge carriers in a ToF technique requires large film thicknesses with high optical density ($OD>10$). Photocurrent transients can be characterized as non-dispersive exhibiting a well developed plateau, in which case the transit time is defined as the intersect of the plateau with the tail of the photocurrent transient as it is shown in Fig. 2.1. In the presence of strong dispersion, the recorded photocurrent transients do not exhibit a plateau, but decrease constantly. In dispersive cases the transit time is defined as the intersect of the two linear regimes in the log photocurrent versus log time plots.⁴² The

electric field is assumed to be uniformly distributed over the sample, which condition is maintained by i) limiting the number of photogenerated charge carrier to less than 10% of the capacitive charge (CU) ii) that the dielectric relaxation time (τ_σ) is larger than the transit time $\tau_\sigma = \epsilon\epsilon_0/\sigma_c \gg t_{tr} = d^2/\mu U$, where σ_c [$\Omega \text{ cm}^{-1}$] is the conductivity. Otherwise the number of equilibrium or doping induced charge carriers (ep_0d , where p_0 is the charge carrier concentration) are sufficient to screen and redistribute the electric field prior to the arrival of the photoexcited charge carriers at the electrode.⁷²

In conductive samples with short τ_σ , the complementary technique of CELIV can be used. In the CELIV technique the equilibrium charge carriers are extracted from a dielectric under a reverse bias voltage ramp ($A = dU_{max}/dt_{pulse}$).⁷³ The mobility of extracted charge carriers is calculated from the time when the extraction current reaches its maximum (t_{max}). The CELIV measurement is most conveniently performed when the current due to the capacitance displacement current ($j(0) = A \times \epsilon\epsilon_0/d$) equals to the extraction current at its maximum Δj . This experimental condition is achieved by *e.g.*, selecting the proper thickness of the sample. In contrary to ToF, the CELIV technique can be used to determine charge carrier mobility in samples with only a few hundred nanometer thickness.

Due to the rather large band gap of most organic materials, the amount of equilibrium charge carriers is very low to be determined by CELIV, but can be increased by chemical doping. Alternatively, charge carriers can be photogenerated by a short laser flash. The photogenerated charge carriers undergo recombination or extracted under the built-in field through the external circuit (short circuit condition). The built-in field can be compensated by applying a DC offset bias (U_{offset}) leading to flat band condition, in which case the photogenerated charge carriers are forced to meet and recombine. The remaining charge carriers can be extracted under a reverse bias voltage ramp after an adjustable delay time (t_{del}) determining their lifetime (photo-CELIV). The calculation of the mobility in the photo-CELIV technique shown in Fig. 2.1 assumes bulk generation of charge carriers, which limits the active layer thickness to approximately 300 - 400 nm depending on the absorption coefficient at the excitation wavelength. The photo-CELIV technique offers the possibility to study charge relaxation phenomena (density relaxation) by varying t_{del} , the determination of the concentration dependence of the mobility by changing the incoming light intensity,

and the voltage (electric field) dependence of the mobility by changing the maximum of the applied voltage pulse (U_{\max}).

Sample preparation and the experimental arrangements:

The samples for the ToF and CELIV studies were prepared by the doctor blade technique on pre-structured ITO coated glass substrates (typical size: 3 cm by 6 cm). The doctor blade technique was found to be superior to drop casting in preparing micrometer thick, pinhole-free films. Then, 1.5 cm by 1.5 cm size samples were cut out from the larger substrates and Aluminum as cathode was evaporated under reduced pressure through a shadow mask. The devices were fixed in a temperature controlled, liquid nitrogen cooled cryostat (Oxford Optistat DN-V, ITC 503 temperature controller, precision ± 0.1 Kelvin). The experimental arrangement for the mobility studies is illustrated in Fig. 2.2.

ToF measurement:

The samples were illuminated using the second harmonic (532 nm) 3 ns pulses of a Nd:YAG pulsed laser (Coherent Infinity 40 – 100). The photogenerated charges drifted through the sample under the external electric field applied by a Brandenberg 477-303 voltage supply, and were recorded by a Tektronix TDS 754 C Digitizing Oscilloscope using either a set of variable resistances or a Femto DLPCA low noise current amplifier.

CELIV measurement:

The samples were kept in the dark, and the doping induced charge carriers were extracted by linearly increasing voltage pulses applied by a digital function generator (Stanford Research DS 345). The CELIV transients were recorded using Tektronix TDS 754 C Digitizing Oscilloscope using a set of variable resistances.

Photo-CELIV technique:

The delay time between the light pulse and the voltage pulse was varied using a digital delay generator (Stanford Research DG 535). The exact time of the light pulse was monitored by a biased photodetector (rise time > 50 ps). The signals were transferred from the computer using either a commercially available software Wavestar for Oscilloscopes (CELIV, Photo-CELIV), or a homebuilt visual basic program (ToF).

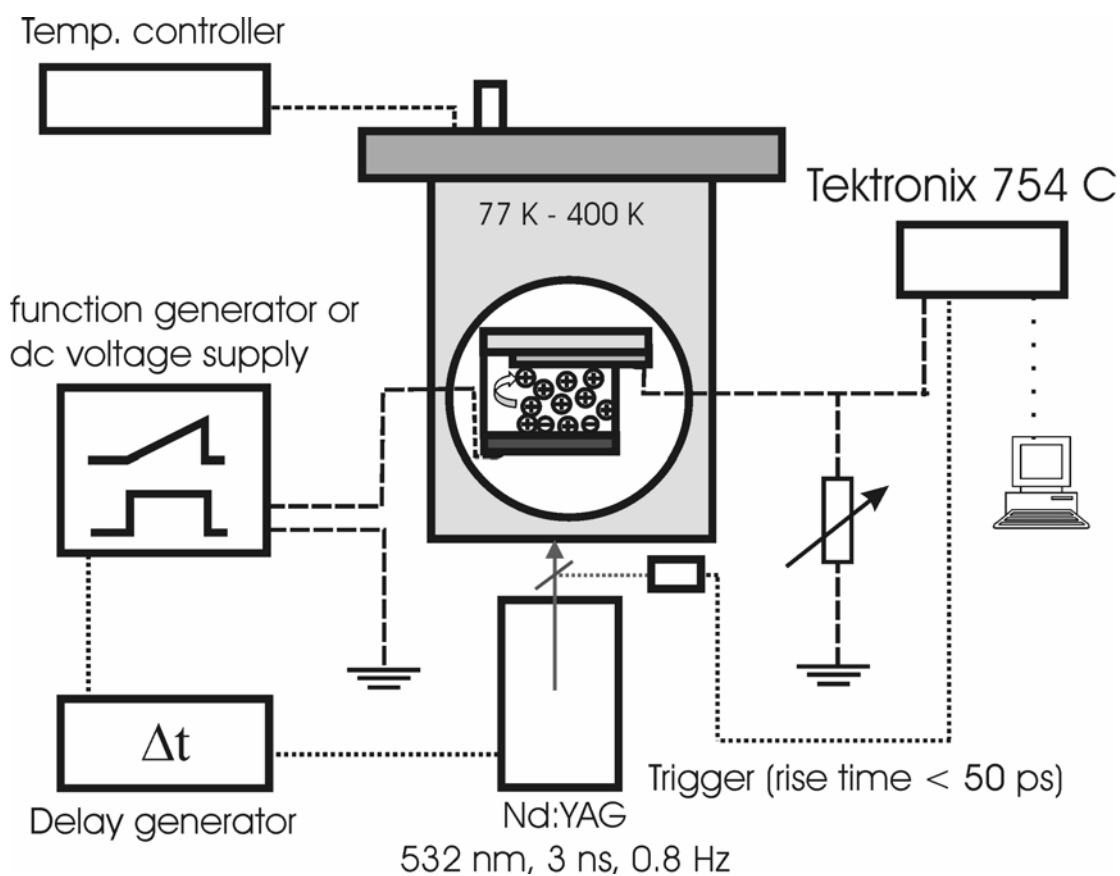


Figure 2.2: Experimental arrangement of the ToF, CELIV and Photo-CELIV technique. The dashed lines represent the signal path, and the dotted lines represent the TTL signals used for triggering the instruments.

2.2 Preparation of Bulk Heterojunction Solar Cells

Bulk heterojunction solar cells unless otherwise mentioned were prepared on pre-structured ITO coated glass substrates. On the top, typically 80-100 nm highly doped PEDOT-PSS layer was spin coated, and dried in reduced pressure for several

hours. The active layer was formed by spin coating. Finally, the cathode was evaporated at reduced pressure through a shadow mask defining the active area. The current voltage characteristics were recorded with a Keithley SMU 2400 unit. The devices were illuminated from the transparent ITO side using a Steuernagel solar simulator simulating AM (air mass) 1.5 sun spectrum. The power conversion efficiency of the solar cells under simulated AM 1.5 conditions were calculated as:

$$\eta_{AM1.5}[\%] = \left(\frac{P_{out} \times m}{P_{in}} \right) \times 100 = \frac{FF \times V_{oc} \times J_{sc} \times m}{P_{in}} \times 100 \quad (2.1)$$

where P_{out} [mW cm^{-2}] is the output electrical power of the device under illumination, P_{in} [mW cm^{-2}] is the light intensity incident on the sample as measured by a calibrated photodiode, and m is the spectral mismatch factor that accounts for deviations in the spectral response to that of the reference cell. Furthermore, FF is the filling factor defined as

$$FF = \frac{V_{mpp} \times J_{mpp}}{V_{oc} \times J_{sc}} \quad (2.2)$$

where V_{mpp} [V], and J_{mpp} [mA cm^{-2}] are the maximum voltage and maximum current density at the maximum power point, respectively, V_{oc} [V] is the open-circuit voltage, J_{sc} [mA cm^{-2}] is the short-circuit current density.

2.3 UV-vis Absorption and Photoluminescence (PL)

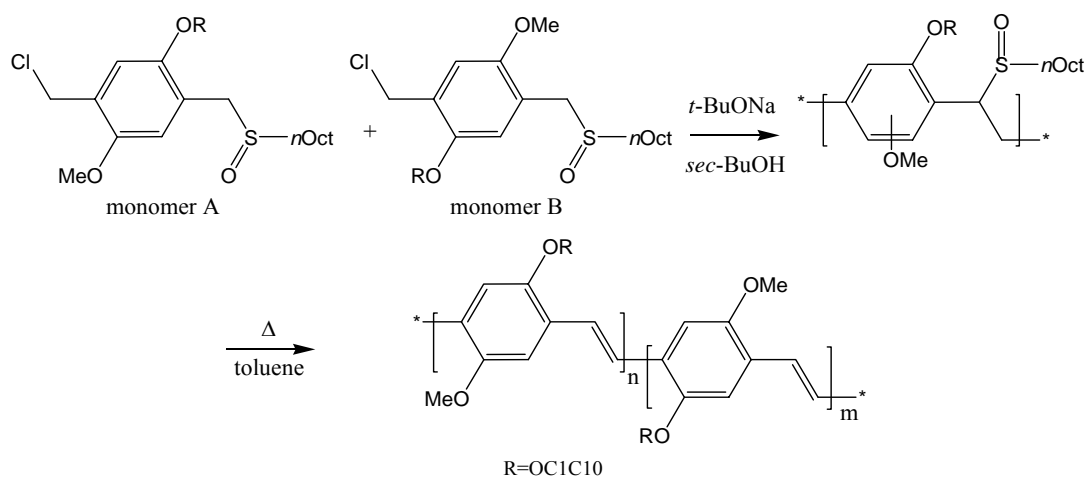
UV-vis absorption spectra in solutions were recorded by a HP 8453 UV-Visible System. PL of the thin film samples was measured as follows: The samples were mounted into a cryostat and placed in the focus of a 5 cm diameter collecting lens. The samples were illuminated from the front side by the 514 nm line of an Ar^+ laser with 0.3 mW intensity. A lowpass filter was used to block the Ar^+ excitation line, and the collected light was coupled to an optical fiber, dispersed by a $L=1/8$ monochromator and detected by a Si photodetector array.

2.4 Materials

Regiorandom MDMO-PPV was purchased from Covion GmbH. Regioregular P3HT was purchased from Rieke Metals, Inc, and further purified according to the procedure described in ref [74], or received from H. C. Starck GmbH, and used without further purification. PCBM was purchased from J. C. Hummelen.

2.4.1 Regioregular MDMO-PPV polymers

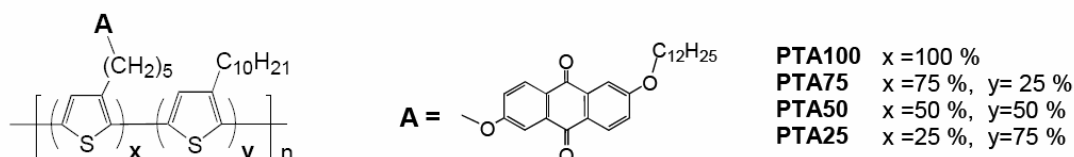
Lutsen et al.⁷⁵ has recently developed a novel regio-controlled synthetic route to alkoxy-PPVs using asymmetrically substituted monomers. Unfortunately, the fully regioregular MDMO-PPV is insoluble, which limits the processability of otherwise promising substances. More recently, a series of soluble regioregular MDMO-PPV polymers were synthesized⁷⁶ based on the sulphonyl precursor route (Scheme 2.1). The ratio of the isomer monomer A and B was varied in the reaction mixture defining n and m in the copolymer.



Scheme 2.1: Synthesis of the regioregular MDMO-PPV copolymers via the sulphonyl precursor route.

2.4.2 Polythiophene – anthraquinone “double-cable” copolymers

Catellani et al. has synthesized a series of well soluble polyalkylthiophene copolymers containing anthraquinone molecules as electron acceptor in the side chains according to scheme 2.2.



Scheme 2.2: Synthesis of the polythiophene – anthraquinone copolymers.

Their photophysical investigations showed that these “double-cable” materials fulfill the major criterion for application in bulk heterojunction solar cells. UV-vis absorption as well as electrochemical techniques showed that no significant interaction occurs between the p-type conjugated chain and the n-type electron acceptor in the ground state. Upon photoexcitation, the occurrence of photoinduced electron transfer was evidenced by FTIR photoinduced absorption and LESR. The photovoltaic response of these polymers is discussed in Chapter 5.3.⁷⁷

2.4.3 Dithienothiophene copolymers

A series of electropolymerized poly(dithienothiophene)s (PDTTs) exhibit low band gaps (~1.1 eV), and peculiar features of the doped or photoexcited positive and negative charge carriers.⁷⁸ Their low band gap makes them a perfect candidate for photovoltaic application; however their insolubility is a serious shortcoming. Catellani et al. [79] has synthesized a series of soluble PDTTs, in which the dithienothiophene moiety is copolymerized with an alkylthiophene monomer. Their chemical structure, weight averaged molecular weight and absorption spectra recorded in dilute chloroform solution are shown in Fig 2.3. The band gap of the resulting copolymers is significantly increased as compared to the electropolymerized, insoluble PDTTs, which is probably due to the extra rotational freedom, therefore reduced conjugation between the dithienothiophene and the thiophene monomers. This effect is even more

pronounced in the P2 polymer, in which 2 additional solubilizing chains are attached to the alkylthiophene monomer. The sterical hindrance, therefore decreased planarity of the conjugated backbone may be the origin of its blue shifted absorption. The band gap is reduced and the optical absorption is red shifted by introducing S,S-dioxide groups on the center thiophene ring of the dithienothiophene moiety. This partially due to the electron withdrawing effect of S,S-dioxide groups.

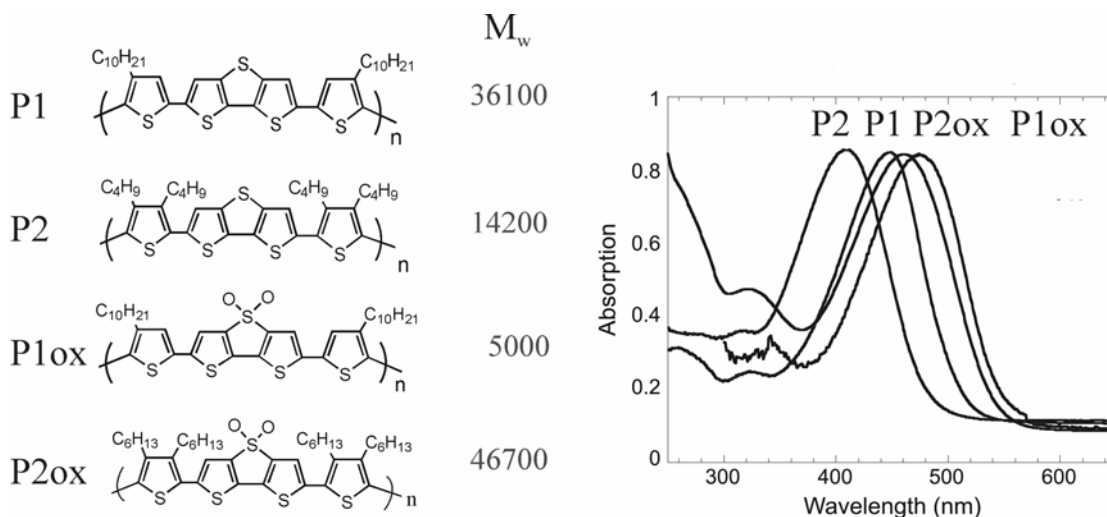


Figure 2.3: The chemical structure, the weight averaged molecular weight (M_w (g mol⁻¹)) and the absorption spectra recorded in dilute chloroform solution of the polydithieno-thiophene copolymers: P1: poly[5,5'-Bis(3-decyl-2-thienyl)-dithieno[3,2-b:2',3'-d]thiophene]; P2: poly[5,5'-Bis(3,4-dibutyl-2-thienyl)-dithieno[3,2-b:2',3'-d]thiophene]; P1ox: poly[5,5'-Bis(3-decyl-2-thienyl)-dithieno[3,2-b:2',3'-d]thiophene-4,4-dioxide]; P2ox: poly[5,5'-Bis(3,4-dihexyl-2-thienyl)-dithieno[3,2-b:2',3'-d]thiophene-4,4-dioxide].

2.4.4 PProDot(Hx)₂

A novel class of conjugated polymers based on disubstituted propylenedioxythiophene polymers has been synthesized by the group of John R. Reynolds. These polymers are promising candidates in applications for electrochromic displays, due to their color change from dark blue-purple to a transmissive sky blue upon p-doping. They also exhibit high quantum yield of luminescence, and have relatively low band gaps. The latter property together with excellent solubility in common organic solvents motivated their study for application in photovoltaic devices, which is discussed in Chapter 5.5. The chemical structure of poly(3,3-

Dihexyl-3,4-dihydro-2*H*-thieno[3,4-*b*][1,4]dioxepine) PProDot(Hx)₂ polymer and HOMO-LUMO levels are displayed in Fig 2.4.⁸⁰ The HOMO level was determined by cyclic voltammetry, and the LUMO level was calculated from the HOMO and the onset of the optical absorption.

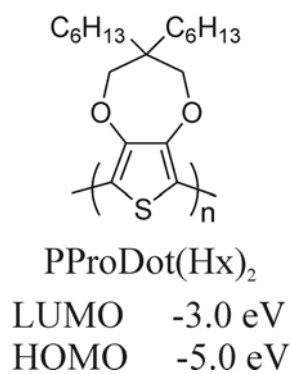


Figure 2.4: Chemical structure and the HOMO and LUMO levels of poly(3,3-Dihexyl-3,4-dihydro-2*H*-thieno[3,4-*b*][1,4]dioxepine) (PProDot(Hx)₂).

Chapter 3

3. Charge Transport in Conjugated Polymers

3.1 Charge Transport in Regioregular MDMO-PPVs

The regiorandom MDMO-PPV (RRa-MDMO-PPV) polymer is a random copolymer of the two stereoisomers of the same monomer. The two isomers differ in the attachment of the shorter methoxy (OC_1) and the longer dimethyloxy (OC_{10}) chain to the backbone phenyl unit. A series of MDMO-PPV copolymer has been synthesized by mixing the two stereo isomers 1-chloromethyl-5-(3,7-dimethyloctyl)-2-methoxy-4-octylsulphoxymethylbenzene (monomer A) and 1-chloromethyl-2-(3,7-dimethyloctyloxy)-5-methoxy-4-octylsulphoxy-methylbenzene (monomer B) via the sulphonyl precursor route as illustrated in Chapter 2, Scheme 2.1.

The solubility of the MDMO-PPV copolymers is greatly reduced as the ratio of either of the isomers is increased above 80 %, which is attributed to aggregation of the conjugated chains in solution. This is further supported by XRD powder diffraction measurements of the MDMO-PPV polymers shown in Fig. 3.1.⁸¹ The numbers in the bracket indicates the weight percent of the two isomers in the reaction mixture, for *e.g.*, 0:100 MDMO-PPV stands for the 100 percent homopolymer, meanwhile 50:50 MDMO-PPV means the 50:50 mixture of the two isomers. As the regioregularity increases, a clearly distinguished reflection peak develops at around 3 degrees, corresponding to an intermolecular distance of 28.5 Å. The exact position of this peak was determined by small angle x-ray scattering measurement. It corresponds to the repeating distance between the polymer backbones separated by side chains. The broad maximum at ~20 degrees is assigned to the amorphous halo of the polymer.

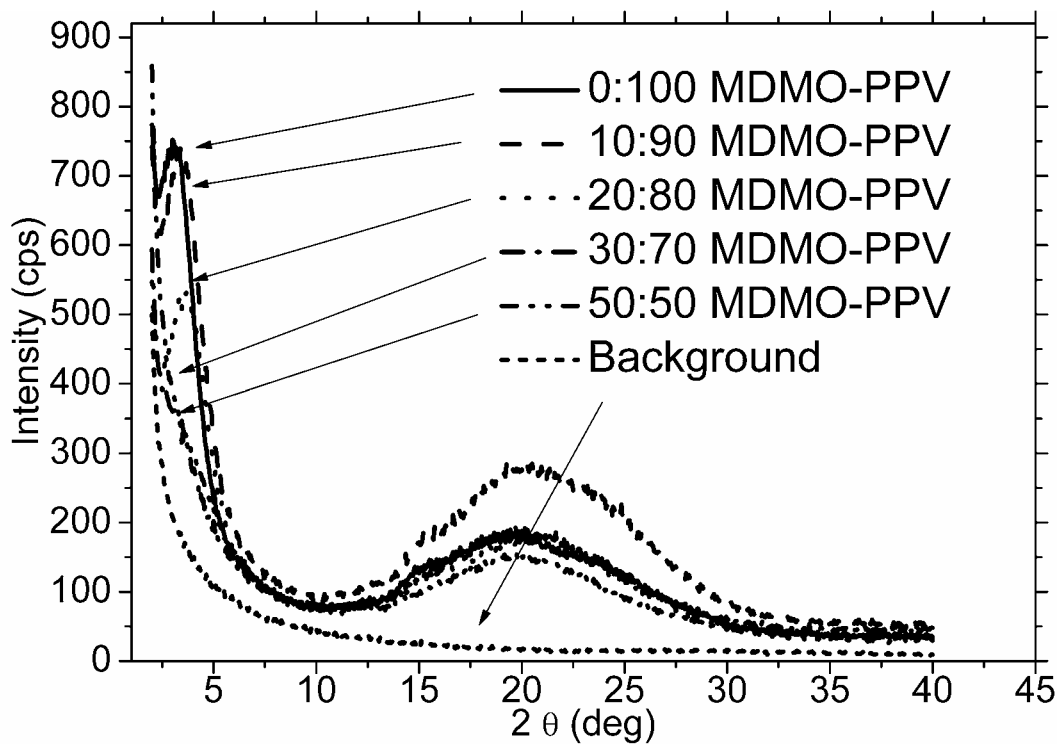


Figure 3.1: $\theta / 2\theta$ -scans of the regioregular MDMO-PPV polymer powders. (by R. Resel)

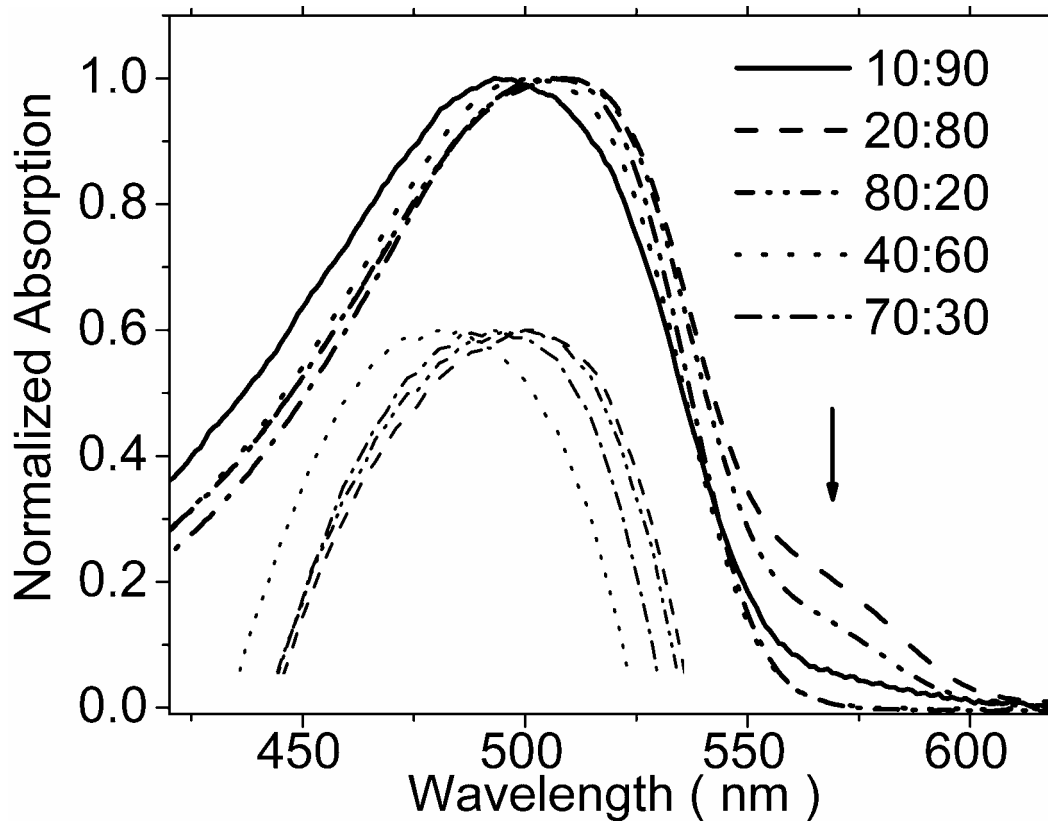


Figure 3.2: UV-vis absorption of various regioregular MDMO-PPV copolymers in dilute chlorobenzene solution.

The UV-vis absorption spectrum recorded in dilute chlorobenzene solution is shown in Fig. 3.2. As the weight percent of either one of the isomers is increased in the reaction mixture above 80%, an additional absorption feature appears (indicated with an arrow) at wavelengths longer than the π - π^* gap absorption of the isolated conjugated chain, which is attributed to aggregate formation. In addition, the absorption maximum of the conjugated polymers is red shifted as the weight percent of either one of the isomers is increased, which is indicative of longer effective conjugated length attributed to the enhanced regioregularity of the conjugated backbone. Since the preparation of devices for the mobility measurement requires well soluble materials, the conjugated polymer resulting from the polymerization of the 70:30 weight percent mixture of monomer A and monomer B (referred to as “70:30 MDMO-PPV”) was selected, and its charge transport and photovoltaic properties are compared to the regiorandom MDMO-PPV (referred to as “RRa-MDMO-PPV”).

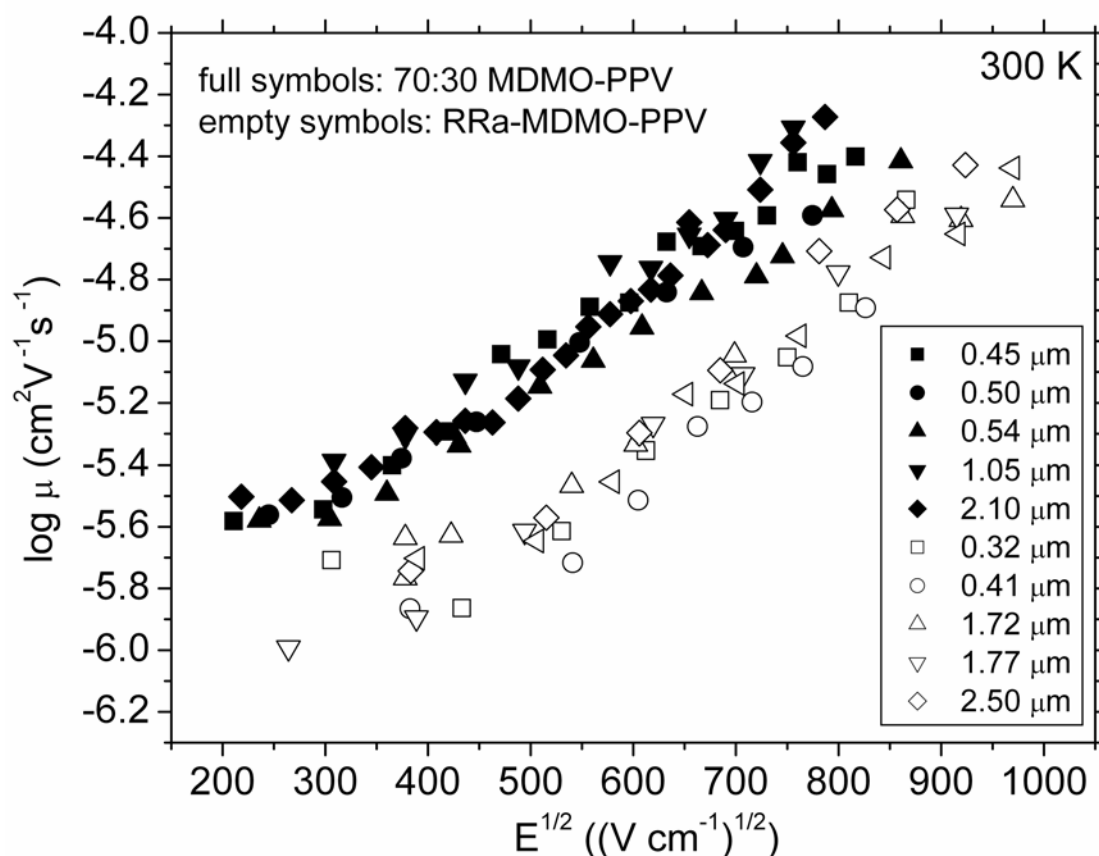


Figure 3.3: Charge carrier mobility of 70:30 MDMO-PPV (full symbols) and RRa-MDMO-PPV (empty symbols) determined by the ToF technique for films with various thickness.

Fig. 3.3 shows the room temperature mobility values determined by the ToF technique for both polymers for various film thicknesses. The room temperature mobility of the 70:30 MDMO-PPV is app. 3.5 times larger at all measured electric fields for all film thicknesses as compared to the RRa-MDMO-PPV. The shape of the photocurrent transients becomes more dispersive as the thickness of the films decreases (Fig. 3.4), yet there is no significant difference in the determined mobility values even for samples with 0.32 μm thickness. The thickness independent mobility values for both polymers has the following implications to our experiments: i) the asymptotic determination of the mobility from the logarithm photocurrent vs. logarithm time plots gives acceptable values even when the photocurrent transients are strongly dispersive. ii) it suggest that the film morphology using doctor blade technique does not change significantly by changing the film thickness within 0.32 μm to 2.3 μm as far as charge carrier mobility is concerned.

Fig. 3.5 a and b shows the plot of logarithm mobility versus square root of the electric field determined at several temperatures for 70:30 MDMO-PPV and RRa-MDMO-PPV, respectively. For the temperature dependence of mobility, samples with larger thickness ($\sim 2 \mu\text{m}$) were selected. The slope of the field dependence of mobility is decreasing, and the zero field mobility – the mobility extrapolated to zero electric field – is increasing with increasing temperature. Such a tendency is predicted by the disorder formalism (Chapter 1.3, eq. 1.6). The mobility could not be determined below $\sim 220 \text{ K}$ because of the absence of a clearly distinguished kink in the logarithm photocurrent versus logarithm time plots.

Fig. 3.6 shows the temperature dependence of the mobility values extrapolated to zero electric field ($\mu(E=0)$) determined by linear regression in Fig. 3.5 for both conjugated polymers. According to disorder formalism, the ordinate intercept of the lines determines the value of the prefactor mobility (μ_0); meanwhile the slope is related to the width of the Gaussian distribution of density of states (σ). The measured experimental data can be fitted using disorder formalism reasonably well; therefore it may provide a framework for further discussion of the charge transport properties of the MDMO-PPV polymers.

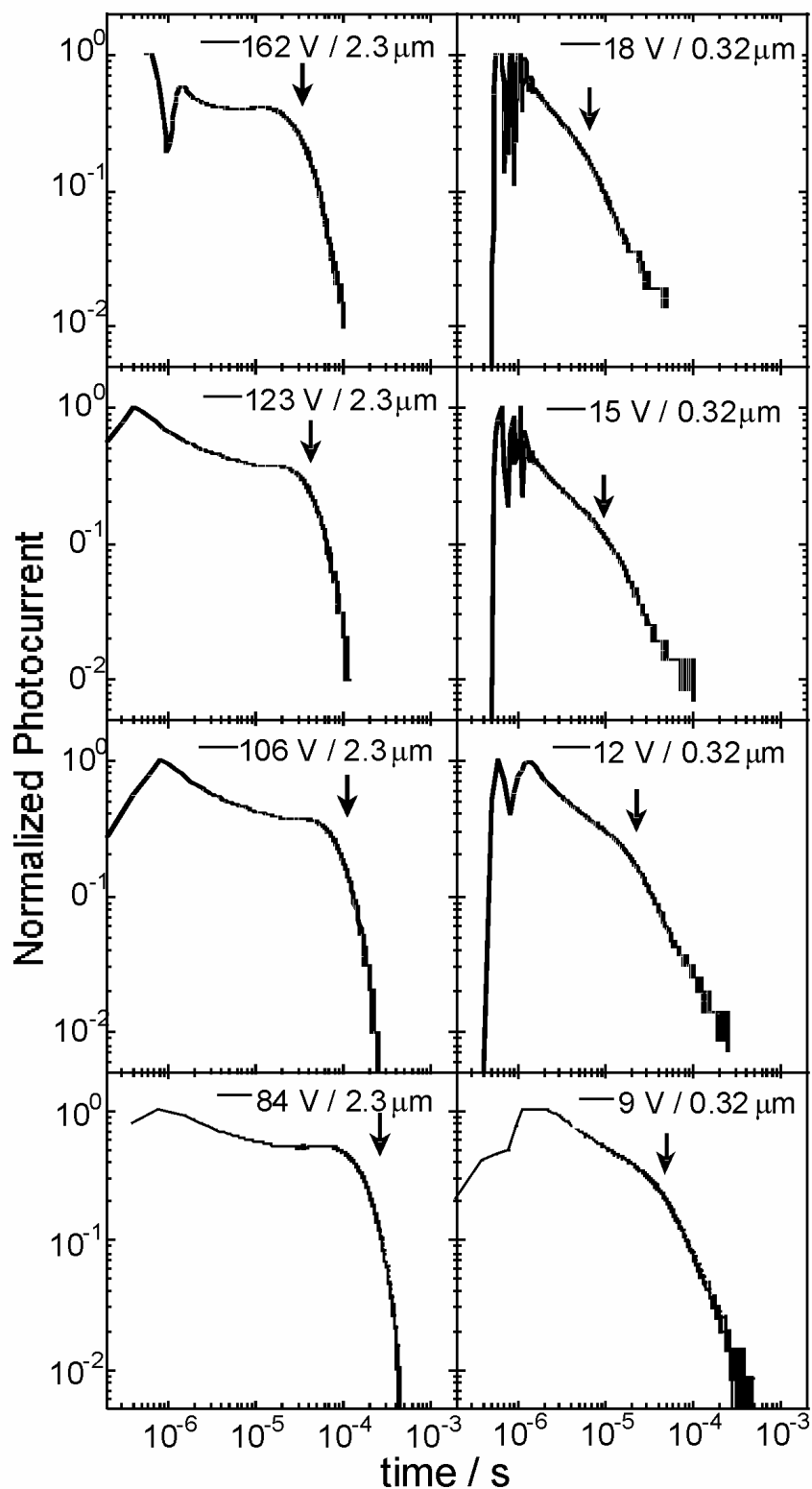


Figure 3.4: Recorded photocurrent transients for a 2.3 μm (left side) and a 0.32 μm (right side) RRa-MDMO-PPV device at various applied electric fields. The arrows indicate the transit time of the charge carriers.

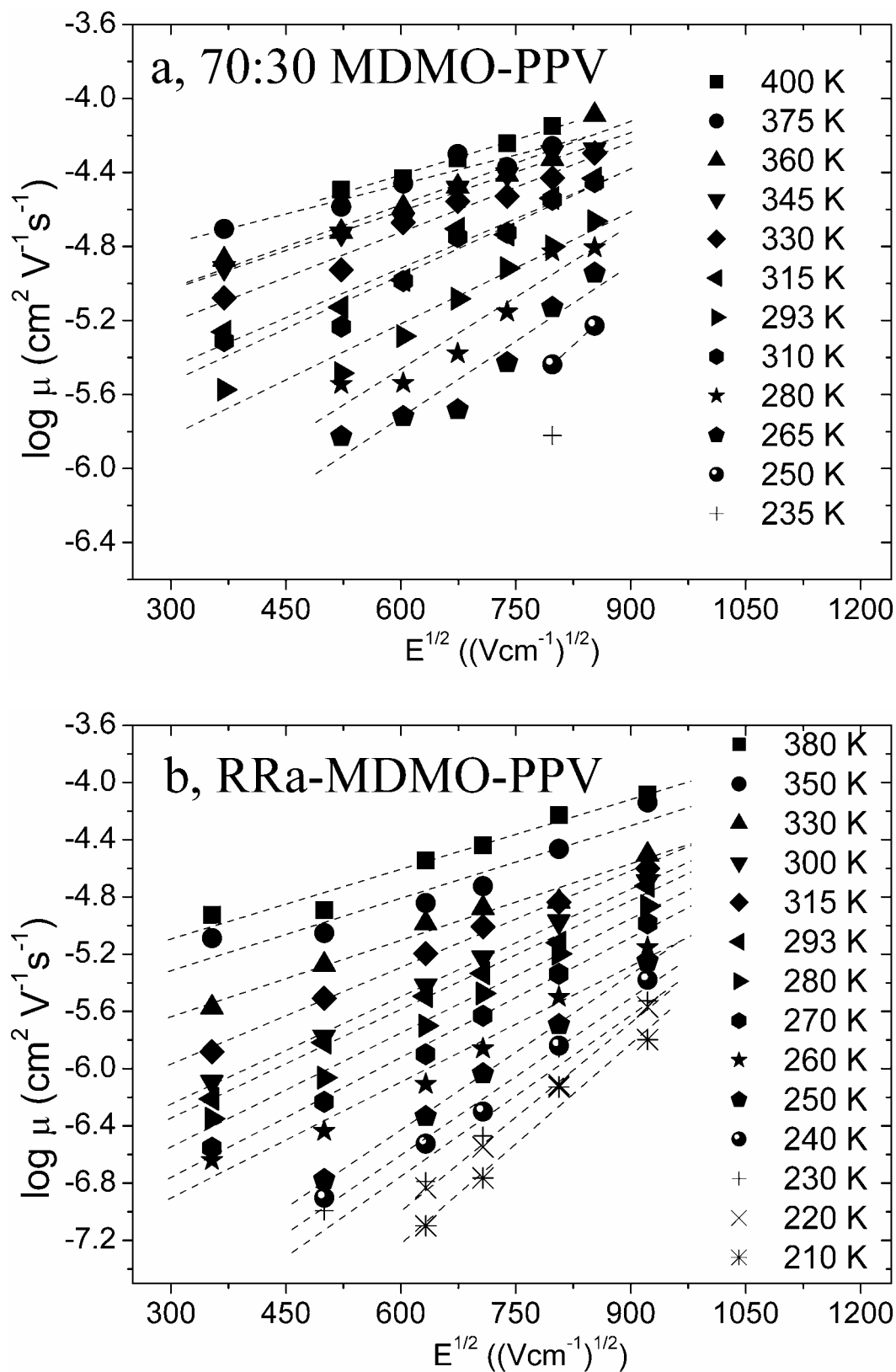


Figure 3.5: Temperature and electric field dependence of mobility determined for a) 70:30 MDMO-PPV; b) RRa-MDMO-PPV. The lines represent linear fits if the data.

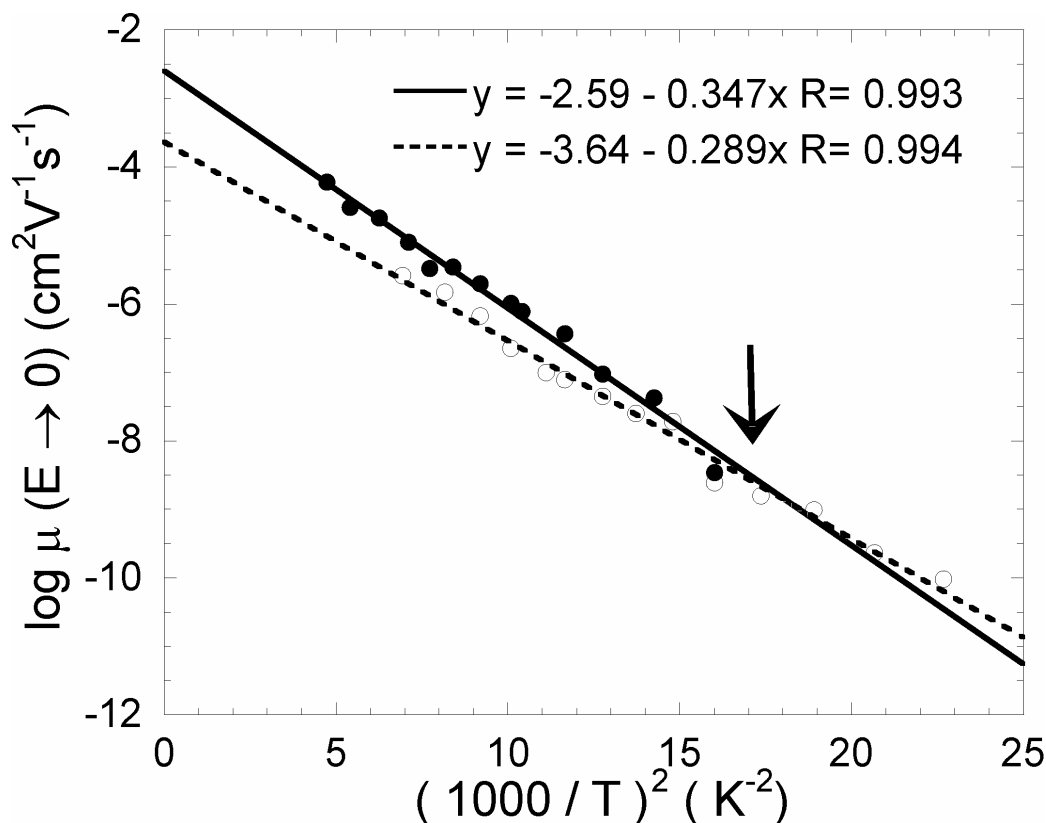


Figure 3.6: Logarithm of the zero field mobility versus $(1000/T)^2$ for 70:30 MDMO-PPV (full symbols) and RRa-MDMO-PPV (empty symbols). The lines represent linear fit of the data.

The parameters μ_0 , σ , and C of eq. 1.6 have been calculated, and summarized in Table 3.1. The fitting constant C was calculated from the slope of the field dependence of mobility versus $(\sigma/kT)^2$. The prefactor mobility (μ_0) is one order of magnitude higher for 70:30 MDMO-PPV, and σ also increases slightly. Interestingly, the zero field mobility of 70:30 MDMO-PPV in Fig. 3.6 is only higher above ~ 230 K indicated by the arrow, but decreasing faster due to the larger energetic disorder, and eventually gets lower than that of RRa-MDMO-PPV below 230 K. Furthermore, the field dependence of mobility characterized by parameter C is slightly larger for the 70:30 MDMO-PPV. The determined value of C agrees well within a factor of only 2 with the theoretically calculated value ($C = 2.9 \times 10^{-4} [(\text{cm V}^{-1})^{1/2}]$).

The prefactor mobility is primarily governed by the amount of electronic coupling between neighboring transport sites, which is a sensitive function (exponential) of the intersite distance. The slight increase of the energetic disorder of the 70:30 MDMO-PPV may originate from lower lying energy states of ordered nano-

aggregates as compared to the amorphous matrix acting as energetic deep traps for overall charge transport.

TABLE 3.1: Determined values of μ_{RT} (room temperature mobility), and parameters μ_0 (prefactor mobility), σ (energetic disorder) and C of the disorder formalism (eq. 1.6).

<i>Sample</i>	$\mu_{RT} [cm^2 V^{-1}s^{-1}]$	$\mu_0 [cm^2V^{-1}s^{-1}]$	$\sigma [meV]$	$C [(cmV^2)^{1/2}]$
70:30 MDMO-PPV	2.8×10^{-5}	2.6×10^{-3}	115	1.54×10^{-4}
RRa-MDMO-PPV	0.85×10^{-5}	0.22×10^{-3}	105	1.35×10^{-4}

The above model is schematically illustrated in Fig. 3.7. The graph on the top of the page illustrates charge motion in the amorphous regions of the films, in which the energy of the transport sites experience a statistically varying environment giving rise to a Gaussian distribution of density of states. The graph on bottom of the page, on the other hand, depicts regions, where the conjugated chains are partially aligned with a better interchain interaction. These regions are expected to create preferential paths (“highways”) for the charge carriers, therefore increase the mobility. In the framework of disorder formalism, the major source of disorder of the charge transport sites is assumed to originate from the variations of dipole - induced dipole interactions between the charge carrier and the surrounding polarizable matrix. Since the more extended electronic wavefunctions of the ordered regions are thought to be more polarizable, the extent of the dipole-induced dipole interactions are expected to be higher in the ordered regions of the films, which lowers the site energy. Since the ordered regions in our model are embedded in an amorphous matrix, these lower lying energy states may act as traps and broaden the distribution of the density of states. Charge hopping at the end of these “highways” (indicated by the large arrow in Fig. 3.7, right) requires sufficient thermal energy and/or tilting the barrier by an external electric field. Therefore, at high temperatures and high electric fields, films of 70:30 MDMO-PPV with better interchain packing shows higher charge carrier mobility. At low temperatures and low electric fields, however, charges might be trapped at the lower lying energy sites of the aligned regions hence causing stronger temperature and electric field dependence of mobility.

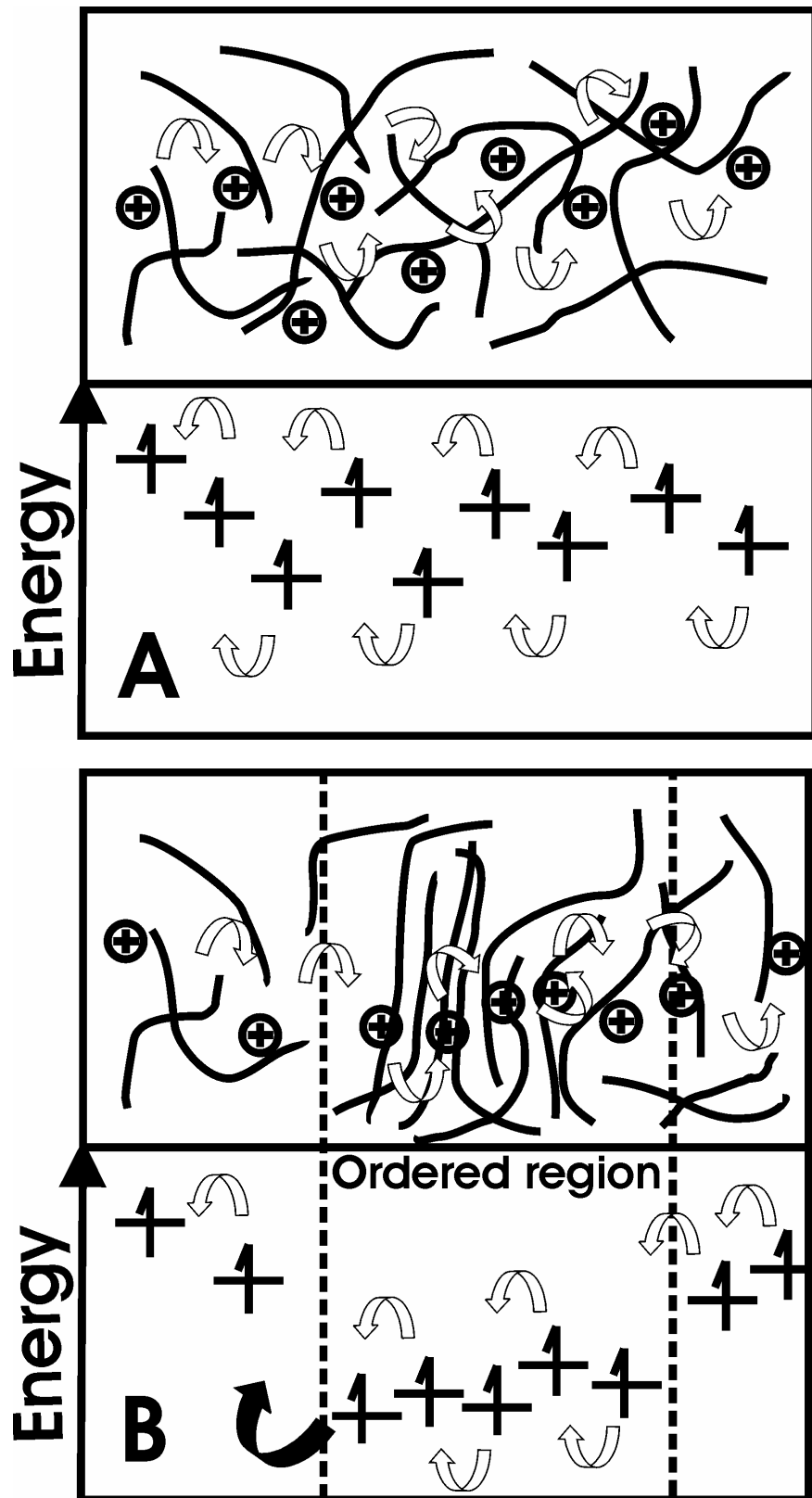


Figure 3.7: Schematic illustration of charge motion and the energy of hopping sites in case when the conjugated chains are randomly oriented (top); when local ordering of the conjugated chains takes place (bottom).

Based on the above model, it is emphasized that three-dimensional ordering, when it would spread over the entire bulk, is expected to increase the mobility significantly. However, in partially ordered cases when the ordered nano-domains are embedded in an amorphous matrix, the competitive interplay between increased energetic disorder and improved charge transport within these ordered regions is expected to control the charge carrier transport.

The proposed increased interchain interactions between the conjugated chains of the regioregular MDMO-PPV is supported by the increased tendency to aggregate as the regioregularity increases (Fig. 3.2). Further indication is given by photoluminescence (PL) and thermally stimulated luminescence (TSL) studies.

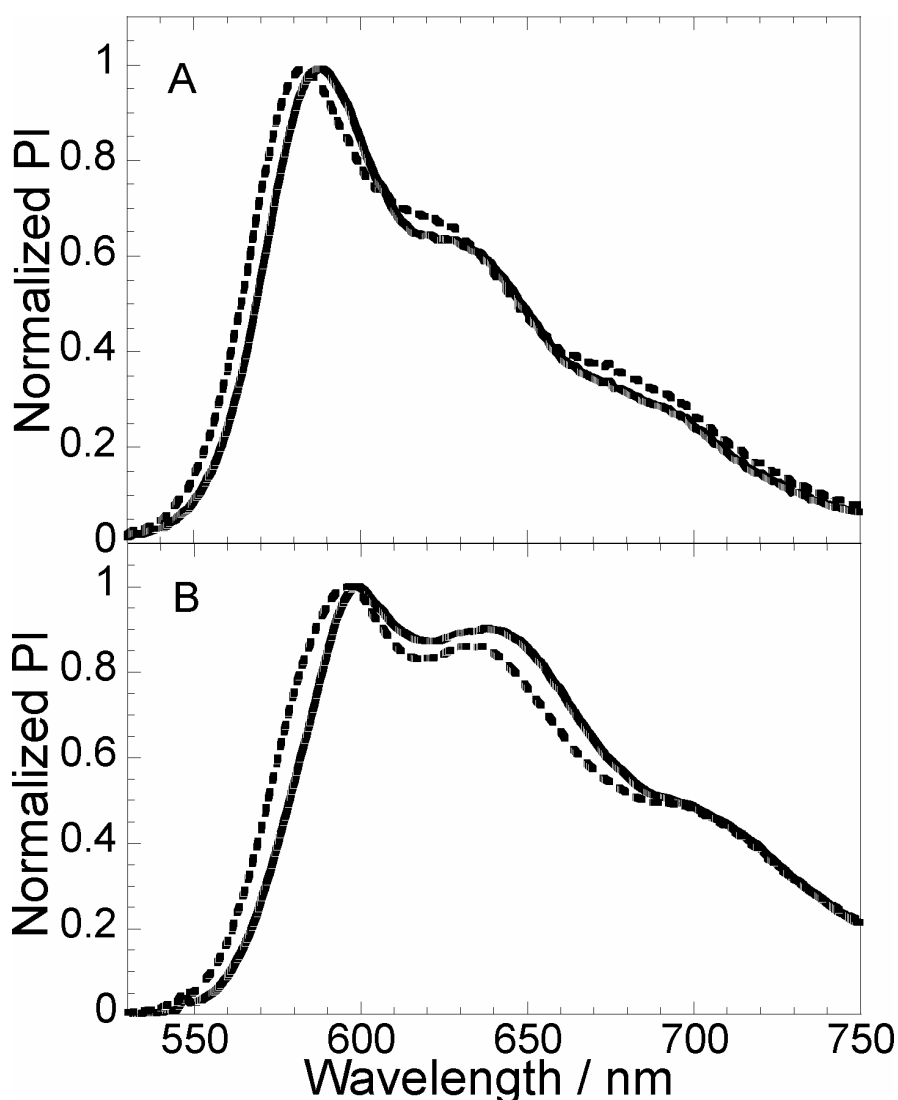


Figure 3.8: PL spectra of 70:30 MDMO-PPV (solid line) and RRa-MDMO-PPV (dashed line) recorded from films prepared by doctor blading of A. 0.25 weight% chloroform solutions; B. 1 weight% chloroform solutions.

The PL spectra recorded for 70:30 MDMO-PPV (solid line) and RRa-MDMO-PPV (dashed line) films prepared from 0.25 weight% chloroform solutions and from 1 weight% chloroform solutions are shown in Fig. 3.8. A and B, respectively. The PL bands of the 70:30 MDMO-PPV films are slightly red shifted in both films indicating that the conjugated chains attain more stretched conformation. Moreover, the peaks in the PL spectra of the films prepared from the more concentrated solutions are red shifted, and the features at 650 nm and 700 nm are selectively enhanced. The selective enhancement of these features is highly indicative of the formation of interchain species in the films of these conjugated polymers.⁸²

Thermally stimulated luminescence experiment (TSL) is a spectroscopic tool frequently used to investigate the effect of electronic traps in luminescent organic materials. In this experiment, the thin film samples were placed in a temperature controlled helium cryostat. After cooling down to 4.2 K, the films were illuminated (typically for 30 sec) by a high-pressure 500 W mercury lamp using an appropriate set of glass optical filters for light selection. Then the samples were heated at a constant rate $\beta = 0.15$ K/s, and luminescence due to radiative recombination of thermally excited electron and holes was recorded in a photon-counting mode with a cooled photomultiplier.

Fig. 3.9 shows the measured TSL curves of the RRa-MDMO-PPV and the 70:30 MDMO-PPV copolymers. The TSL curves were deconvoluted into two Gaussian distributions shown by the solid lines. In the case of the 70:30 MDMO-PPV polymer, the high temperature band at ~ 100 K is relatively increased with respect to the 50 K band. The higher temperature peak in this class of polymers has been previously assigned to recombination of charge carriers thermally liberated from lower lying structural traps.⁸³ The selectively increased higher energy TSL peak measured for the 70:30 MDMO-PPV copolymer suggests the presence of higher concentration of structural traps in accordance with the finding of the charge transport studies.

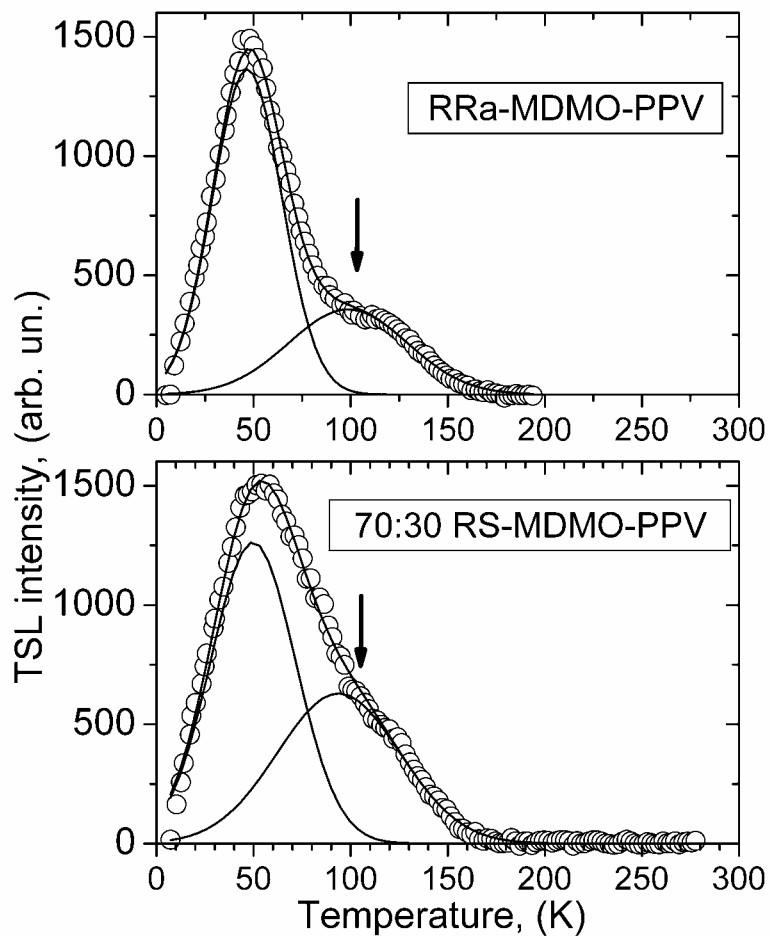


Figure 3.9: Thermally Stimulated Luminescence (TSL) curves recorded for RRa-MDMO-PPV (upper) and 70:30 MDMO-PPV (lower). The solid lines represent fits of Gaussian line shapes to the experimentally measured curves. (Measured by A. Kadashchuk).

3.2 Charge Transport in Regioregular Poly(3-hexylthiophene)

3.2.1 Charge carrier mobility investigated by the ToF technique

A recent improvement of the performance of bulk heterojunction solar cells was achieved using regioregular poly(3-hexylthiophene) P3HT.^{84,85} The state-of-the-art P3HT based devices show incident photon to converted electron efficiency (IPCE) close to 75 % at the absorption maximum, which indicates nearly 100 percent collection of the photogenerated charges at the electrodes. Charge carrier mobility in P3HT is often investigated in an FET structure; however detailed temperature and electric field dependence of mobility studies by ToF was not available. This is partially due to the large dark conductivity of poly(alkylthiophenes) attributed to oxygen⁸⁶ or moisture⁸⁷ doping when exposed to air. Dark conductivity generally limits the applicability of ToF.

The effect of volatile dopants on the conductivity of regioregular P3HT is illustrated by a series of CELIV curves in Fig. 3.10. The sandwich-type device (ITO/P3HT/AL) was exposed to air for a few hours to increase conductivity, and then placed into a temperature controlled nitrogen cooled cryostat, and evacuated. A typical CELIV curve upon the application of a reverse bias, $A=10 \text{ V} / 16,66 \text{ } \mu\text{s}$ linearly increasing voltage pulse just after evacuation is shown in Fig. 3.10 a. The initial current step $j(0)=A \times \epsilon \epsilon_0 / d$ corresponds to the capacitive displacement current of a dielectric with a thickness d and dielectric constant ϵ . The extraction current Δj is due to the extraction of mobile carriers from the dielectric. The conductivity from a CELIV curve can be calculated according to⁷²

$$\sigma_c = \frac{3\epsilon\epsilon_0\Delta j}{2t_{\max}j(0)} \quad (3.1)$$

The conductivity value of $\sigma_c=1.9 \times 10^{-7} \text{ } \Omega^{-1} \text{ cm}^{-1}$ was calculated shortly after the sample was evacuated. The conductivity gradually decreases during evacuation ($1.7 \times 10^{-7} \text{ } \Omega^{-1} \text{ cm}^{-1}$ 10 minutes after evacuation (note the smaller Δj in Fig. 3.10 b), which is faster at elevated temperatures ($\sigma_c=1.65 \times 10^{-7} \text{ } \Omega^{-1} \text{ cm}^{-1}$ after 5 min at 340 K).

The Δj cannot be determined after the devices were kept for ~ 10 min at 340 K, which indicates very low conductivity (Fig. 3.10 d), and proves that the doping of P3HT is reversible, and related to the influence of volatile dopants, probably oxygen and / or water.

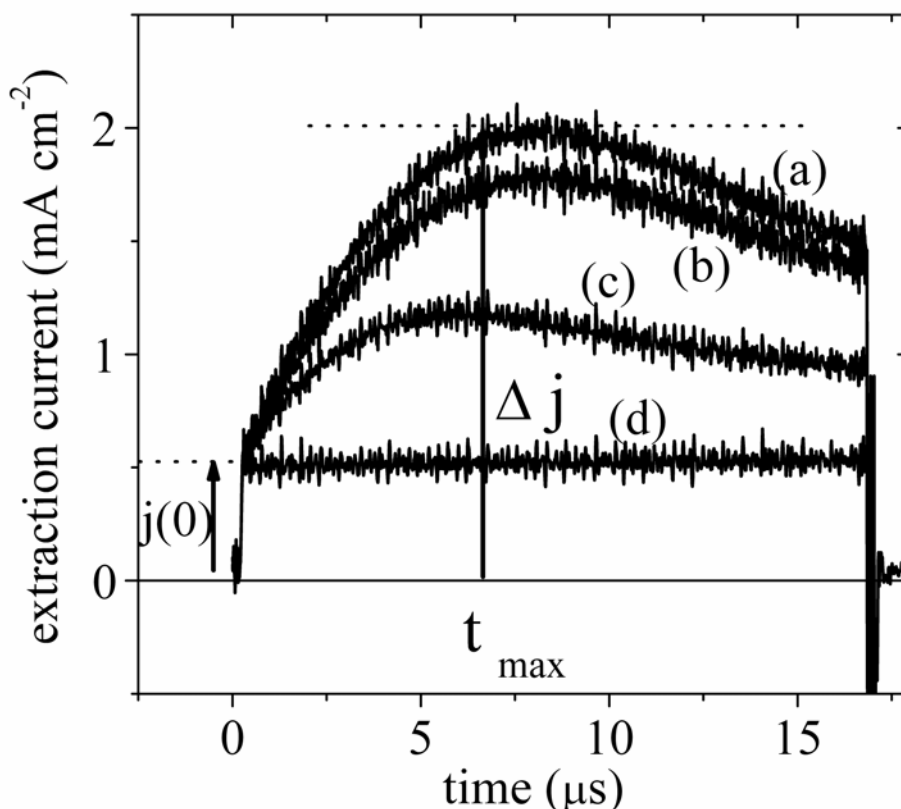


Figure 3.10: A series of CELIV curves recorded for an ITO/P3HT/Al device exposed to air a) shortly after evacuation in a cryostat; b) after 10 min; c) after 5 min at 340 K; d) after 10 min at 340 K.

The temperature and electric field dependence of mobility in low conductivity, purified samples of P3HT was investigated by the time of flight technique. The low conductivity of the samples is achieved by the purification procedure described in ref.[74]. In addition, the devices were prepared, stored and characterized in a dry, inert atmosphere. The photocurrent transients recorded at 293 K and 180 K in regioregular P3HT purchased from Rieke, Inc. is shown at various applied voltages in Fig. 3.11. The sandwich type device (ITO/P3HT/AL), thickness $4.6 \mu\text{m}$, was illuminated by 3 ns laser pulses at 532 nm excitation wavelength through the Aluminum side. The transit time of charge carriers indicated by the arrows is decreasing at every temperature as the voltage is increased.

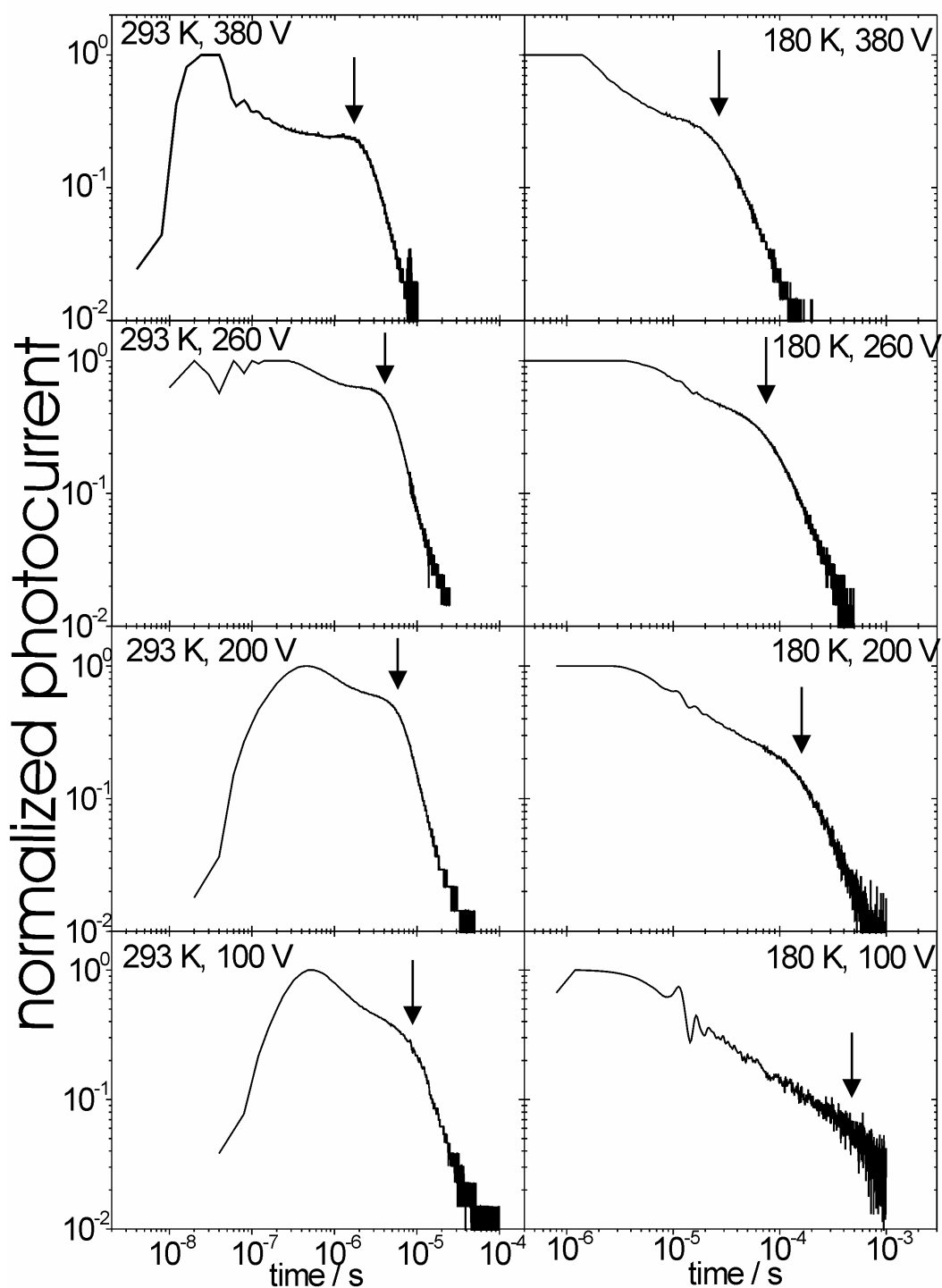


Figure 3.11: Time of flight transients of a low dark conductivity, 4.6 μm thick P3HT sample sandwiched between ITO and Al recorded at various applied voltages and at 293 K and 180 K. The transit time is indicated by the arrows.

The photocurrent transients are non-dispersive with a well developed plateau and a rather short post transit time tail at room temperature. At lower temperatures

(<180 K) the plateau region disappears, which indicates the dispersive motion of the photogenerated charge carriers.

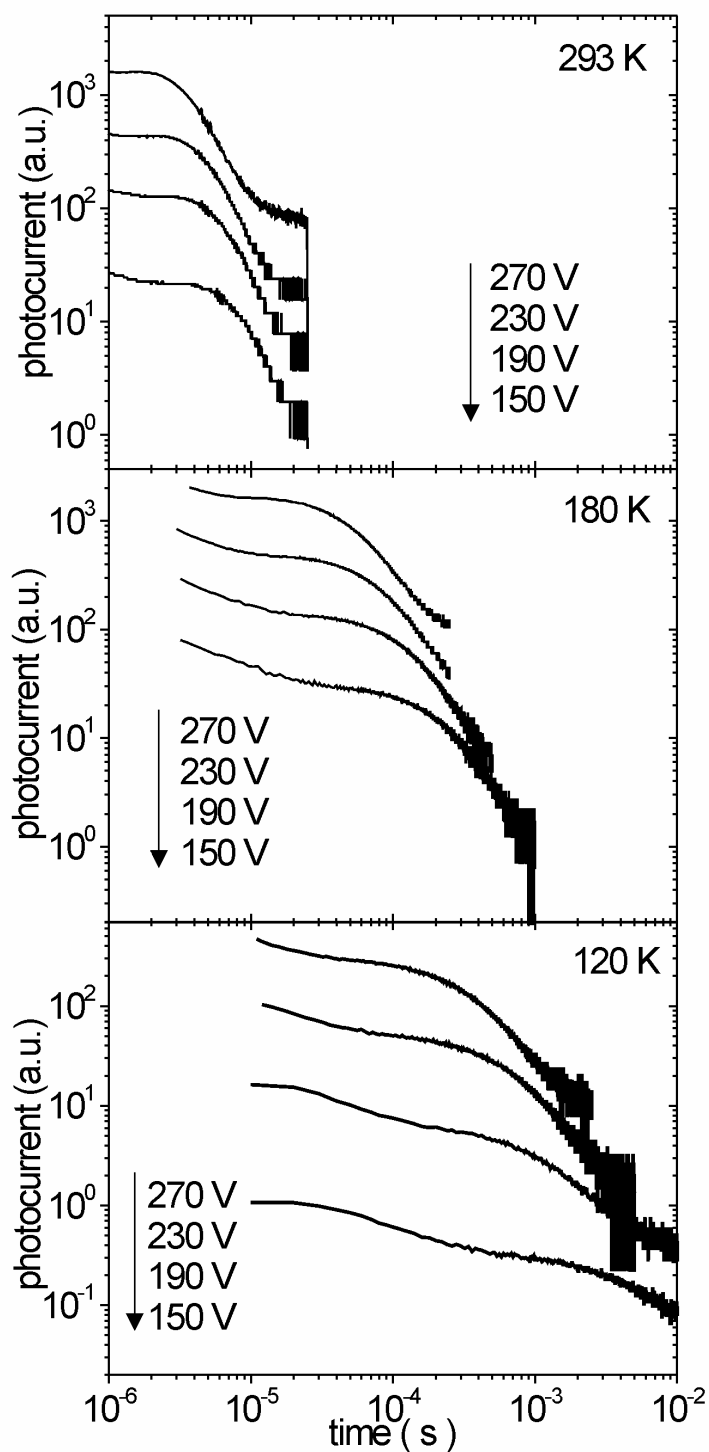


Figure 3.12: Time of flight transients recorded for a low dark conductivity P3HT sample (thickness $3.6 \mu\text{m}$) at various applied voltages and at 293 K and 180 K and 120 K.

Regioregular P3HT sample received from different commercial source was also investigated (H. C. Starck GmbH). The recorded photocurrent transients for a 3.6 μm thick sample are shown in Fig. 3.12. The transients recorded for this polymer were reproducibly more non-dispersive at all temperature as compared to the one purchased from Rieke, Inc. The origin of the improved properties has not been clarified yet, but maybe related to the higher purity of this material as compared to the Rieke P3HT. The increasing dispersion with decreasing temperature for both P3HT samples has important implications. Dispersive photocurrent transients can be analyzed in the framework of the formalism developed by Scher and Montroll (Chapter 1.3, eq. 1.1-1.2). That formalism predicts that the slope parameters (α) prior and after the transit time should sum up to 2.

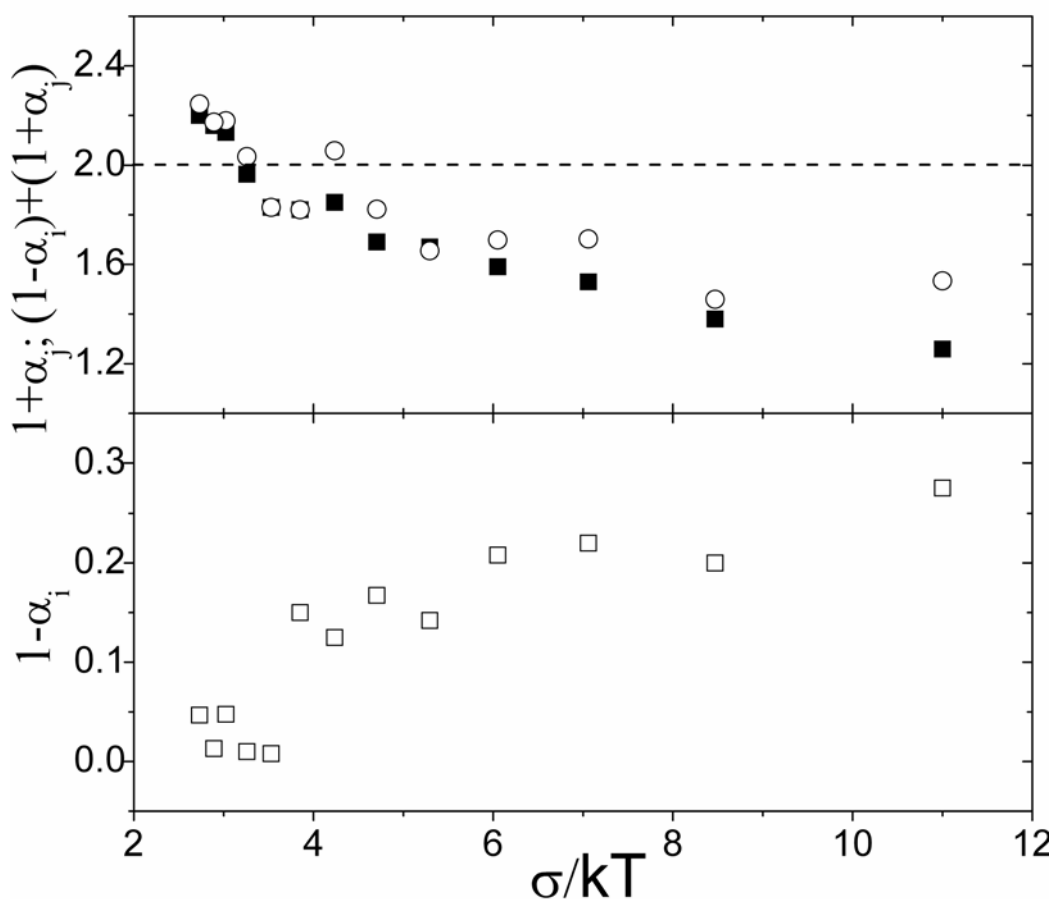


Figure 3.13: Temperature (σ/kT) dependence of the slope of the photocurrent transients prior (□): ($1 - \alpha_i$), and after (■): ($1 + \alpha_j$) the transit time, and their sum (○): ($1 - \alpha_i$) + ($1 + \alpha_j$) at an electric field $E = 7 \times 10^{-5} \text{ V cm}^{-1}$.

The calculated values of the slope parameters $(1-\alpha_i)$, $(1+\alpha_j)$ and their sum $(1-\alpha_i)+(1+\alpha_j)$ are plotted versus σ/kT in Fig. 3.13. It is evident that the sum of the slope parameters deviates from 2. In other words, α calculated prior and after the transit time is not identical indicating that the Scher - Montroll formalism is not applicable to describe charge transport in our samples.⁸⁸ Nevertheless, the parameters $(1-\alpha_i)$ and $(1+\alpha_j)$ can be used to describe the shape of the photocurrent transients in an operational way to delineate the occurrence of dispersion.⁸⁹ The determined slope parameter $(1-\alpha_i)$ is nearly 0 at higher temperatures corresponding to non-dispersive transients, but increasing with decreasing temperatures and reaches a value of 0.25 at around 180 K indicating a nondispersive to dispersive (ND→D) transition. Since the time required to reach quasi-equilibrium at low temperatures is increasing faster than the transit time, charge carrier motion without quasi-equilibrium is probed at lower temperatures.

The mobility versus the electric field squared is plotted in Fig. 3.14 calculated for both P3HT polymers. The mobility follows a $\log \mu \propto \beta E^{1/2}$, $\beta < 0$ Poole-Frenkel-like dependence at lower temperatures, and β turns to negative at higher temperatures ($>250\text{K}$) and at lower electric fields. Such negative electric field dependence of mobility has been observed in various organic semiconductors, including molecularly doped polymers,^{44,45} molecular glasses⁴⁶ and a polysilane derivative,⁹⁰ yet first time clearly observed in a conjugated, semiconducting polymer.⁹¹ The occurrence of negative electric field dependence of mobility is understood as the effect of superimposed energetic and positional disorder as it is expressed by disorder formalism. Negative electric field dependence of mobility has only been observed using the ToF technique, and several groups have argued that it is an experimental artifact rather than the intrinsic property of the materials.

It was argued that screening of the electric field⁷² in conductive samples may result in higher apparent mobility values that strongly increase with decreasing electric field below a critical electric field $E < 4 \times 10^4 \text{ V cm}^{-1}$.⁹² Clearly, the rather weak negative electric field dependence of mobility observed in low dark conductivity samples shown in Fig. 3.14 cannot be attributed to such spurious electric field effect.

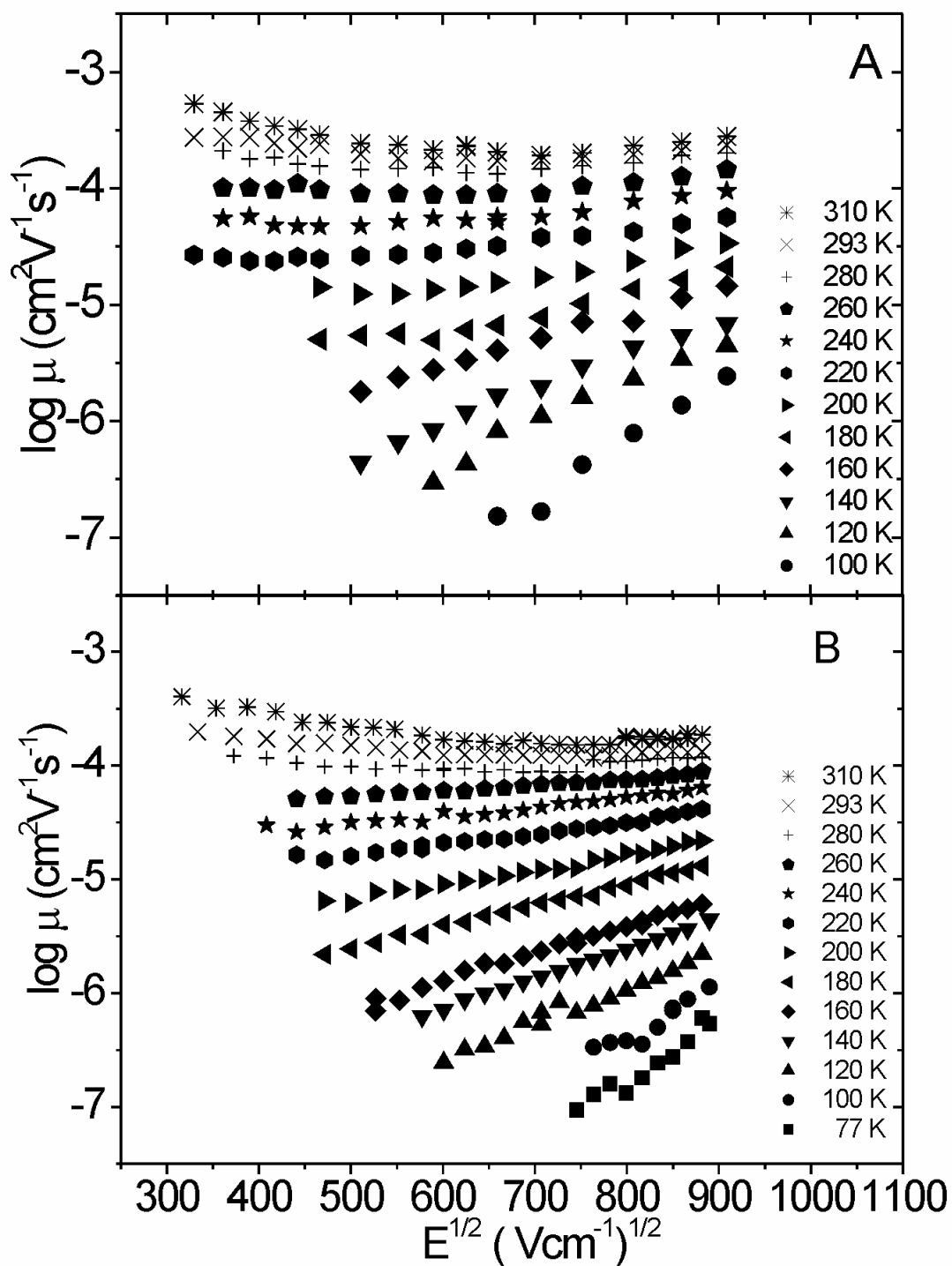


Figure 3.14: Electric field dependence of the mobility determined by the ToF technique in A, P3HT purchased from Rieke, Inc.; B, obtained from H. C. Starck GmbH.

3.2.2 Charge carrier mobility investigated by the CELIV technique

Hirao et al. argued the negative electric field dependence of mobility may be caused by electric field independent carrier diffusion that may become dominant at electric fields weaker than $2 \times 10^4 \text{ V cm}^{-1}$.⁹³ A straightforward experimental check of the effect of diffusion on the transit time and therefore mobility is the application of the CELIV technique, because there is no diffusion current at $t=0$ due to thermodynamic equilibrium established prior to the application of the voltage pulse. The charge carriers are distributed homogeneously throughout the dielectric prior charge extraction provided that the delay time between subsequent voltage pulses is sufficiently long. Moreover, the CELIV technique was shown to yield the proper electric field dependence in moderately conductive samples. The reversible oxygen or moisture doping demonstrated in Fig. 3.10 provides the opportunity to determine the CELIV mobility in the same P3HT used for the ToF studies exposed to air.

Fig. 3.15 shows CELIV transient measured in a sandwich type device (ITO/P3HT/Al, 1.3 μm thickness) by applying reverse bias voltage pulses with varying U_{max} at A) 293 K, and B) 130 K. The time when the extraction current reaches its maximum (t_{max}) is changing by 4 orders of magnitude upon cooling down from 293 K to 130 K. The shift of the t_{max} to longer times is related to the temperature dependence of the mobility. The t_{max} is longer as the speed of the voltage rise $A=dU/dt$ decreases, thus indicating the voltage (electric field) dependence of the drift velocity of the charge carriers. The electric field in a CELIV measurement is not constant, but depends on both space and time coordinate. It is calculated at the extraction maximum according to $E=(A \times t_{\text{max}})/d$.⁷²

Dispersion in a CELIV transient can be characterized by the half width of the extraction current to time t_{max} as $t_{1/2}/t_{\text{max}}$.⁹⁴ The theoretically calculated value of a non-dispersive CELIV transient is $t_{1/2}/t_{\text{max}}=1.2$. This empirical parameter, which describes the shape of the transient (how fast it rises and decays after reaching its maximum value) has been determined for the transients in Fig. 3.15, and values between 1.6 – 2.5 have been obtained at 293 K and it is around 2.6 at 130 K. These values are considered moderate when compared to other systems (for e.g. $\mu\text{c-Si:H}$).⁹⁴

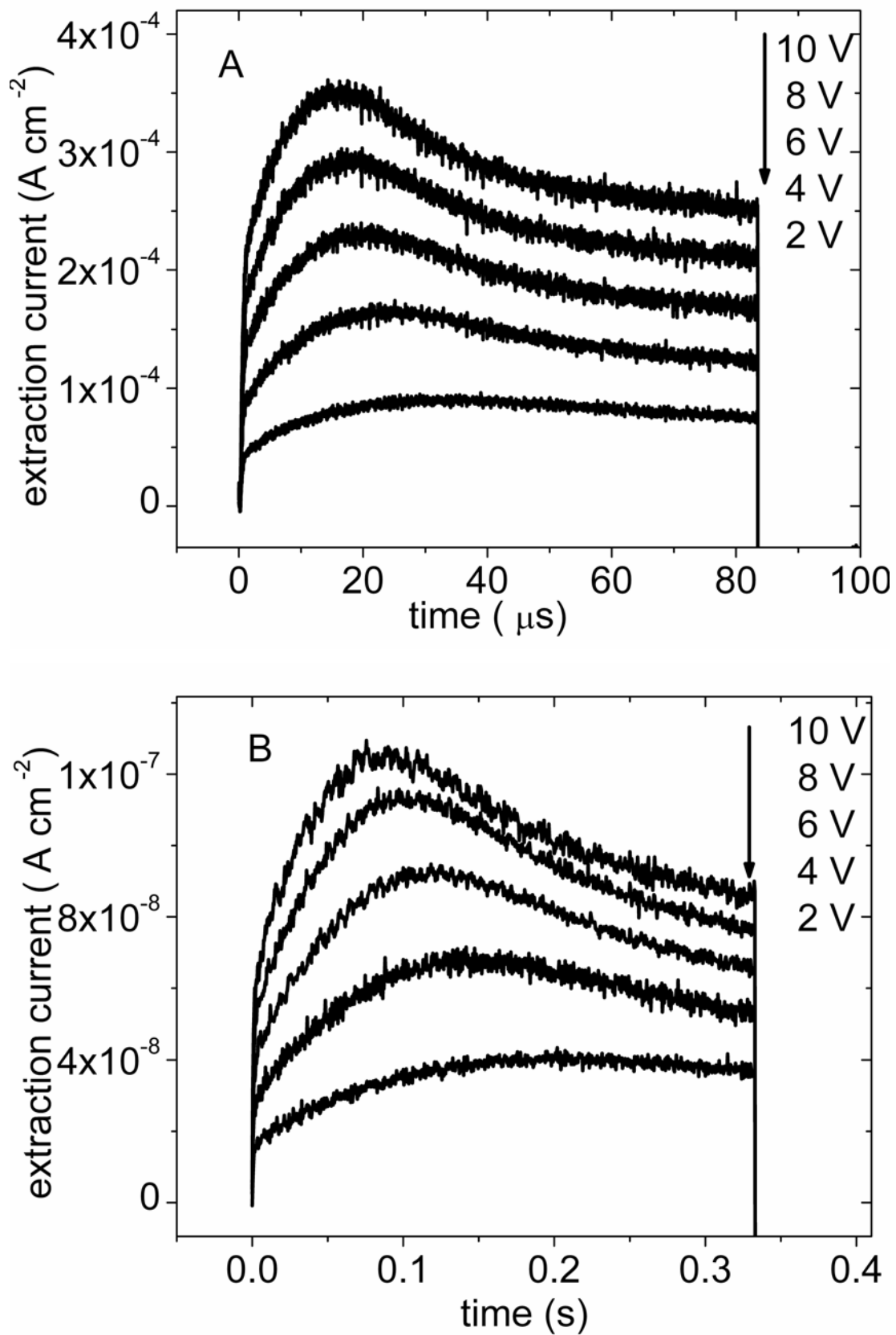


Figure 3.15: A, B. Recorded CELIV curves in regioregular P3HT samples at 293 K, and 130 K, respectively.

The temperature and electric field dependence of mobility determined by the CELIV technique is plotted versus $(E=(A \times t_{\max})/d)^{1/2}$ in Fig. 3.16. The mobility is well approximated with a $\log \mu \propto \beta(E)^{1/2}$ electric field dependence at all measured temperatures. The slope β decreases with temperature, becomes 0 at ~ 250 K, and turns to negative at higher temperatures. The amount of extracted charge carriers calculated from CELIV curves recorded at the beginning of the measurements (300 K) was $n=3 \times 10^{14} \text{ cm}^{-3}$, which is decreased by $\sim 50\%$ towards the end of the experiment *e.g.*, $n=1.75 \times 10^{14} \text{ cm}^{-3}$ measured at 293 K due to evaporation of volatile dopants in vacuum as it was demonstrated in Fig. 3.10. Nevertheless, the mobility value and its electric field dependence measured at 293 K are not affected by this change.

In principle, the CELIV technique probes the mobility of the more mobile charge carriers. If both carriers are mobile, two extraction peaks corresponding to extraction of both carriers may be observed. The extraction current in our experiment is dominated by holes rather than electrons due to the orders of magnitude higher mobility of the former. This is confirmed by the ToF technique, in which the photocurrent transients of electrons featured a fast exponential decay without clear transit time indicative of efficient electron trapping.⁹⁵

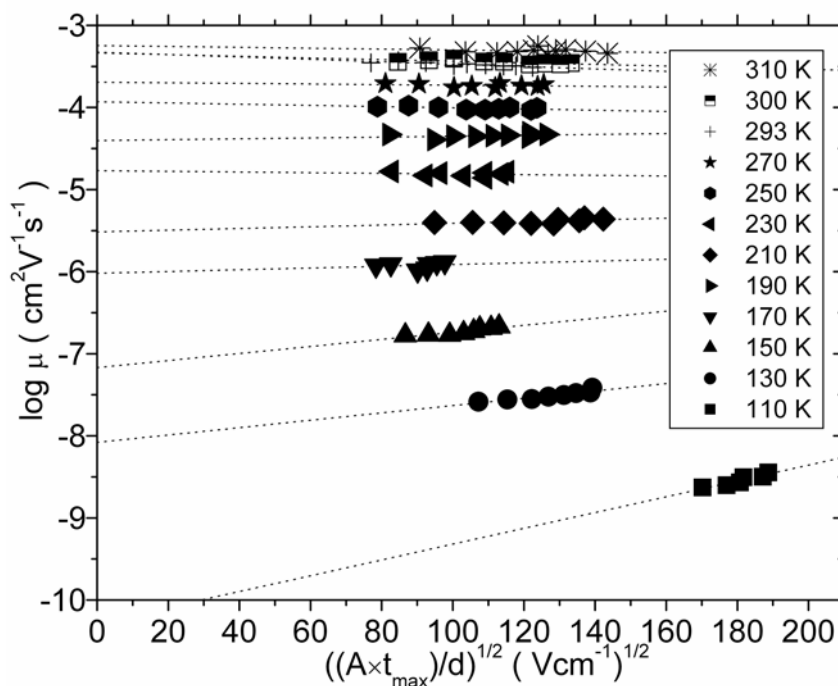


Figure 3.16: CELIV mobility values versus square root of electric field at various temperatures. The devices were measured first at 300 K, cooled to 110 K, and measured at subsequent heating steps.

The temperature and electric field dependence of the hole mobility obtained by both experimental techniques is plotted in Fig. 3.17. The overall agreement obtained by these principally different techniques, and particularly, the negative electric field dependence of mobility at temperatures above ~ 250 K implies that it is not an experimental artifact of the ToF technique caused by either dark conductivity or the effect of charge carrier diffusion. The latter can be excluded, since photocurrent transients due to diffusion current are expected to be highly dispersive, electric field independent and thickness dependent, which is in direct contradiction to experimental observations. The observed negative electric field dependence, therefore, may be an intrinsic property of the P3HT samples studied at least in this low charge concentration regime, and can be explained as the influence of positional disorder on the motion of charge carriers.⁹⁶

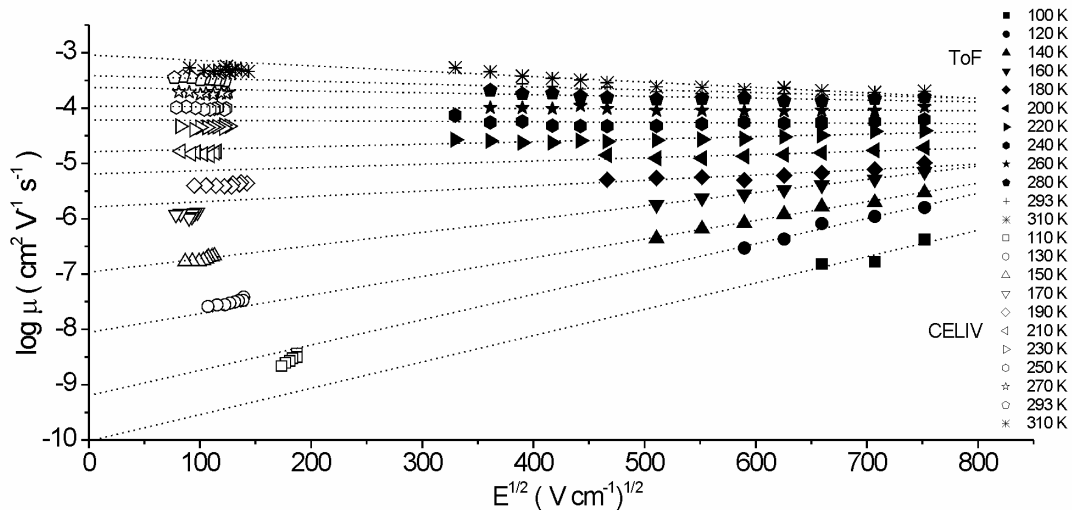


Figure 3.17: Temperature and electric field dependence of the mobility determined by both time of flight (ToF) and CELIV experiments.

3.2.3 Temperature dependence of the mobility: A comparison

Fig. 3.18 shows the Arrhenius plots of the mobility at various applied voltages calculated for the P3HT polymer obtained from H. C. Starck. The Arrhenius plots of the logarithm mobility intercept at $T_0 \sim 270$ K, following the prediction of Gill's model (Chapter 1.3, eq. 1.3). A linear relationship is found at higher temperatures, yet the low temperature mobility tends to deviate from the $1/T$ dependence. From the higher temperature range, the zero field activation energy (Δ) and the fit constant (β_{PF})

is calculated. The effective activation energy ($E_{\text{act}} = \Delta - \beta_{\text{PF}} E^{1/2} (1000k_B)^{-1}$) was calculated from the slope of the temperature dependence at each electric field, and plotted versus squared electric field in the inset of Fig. 3.18.

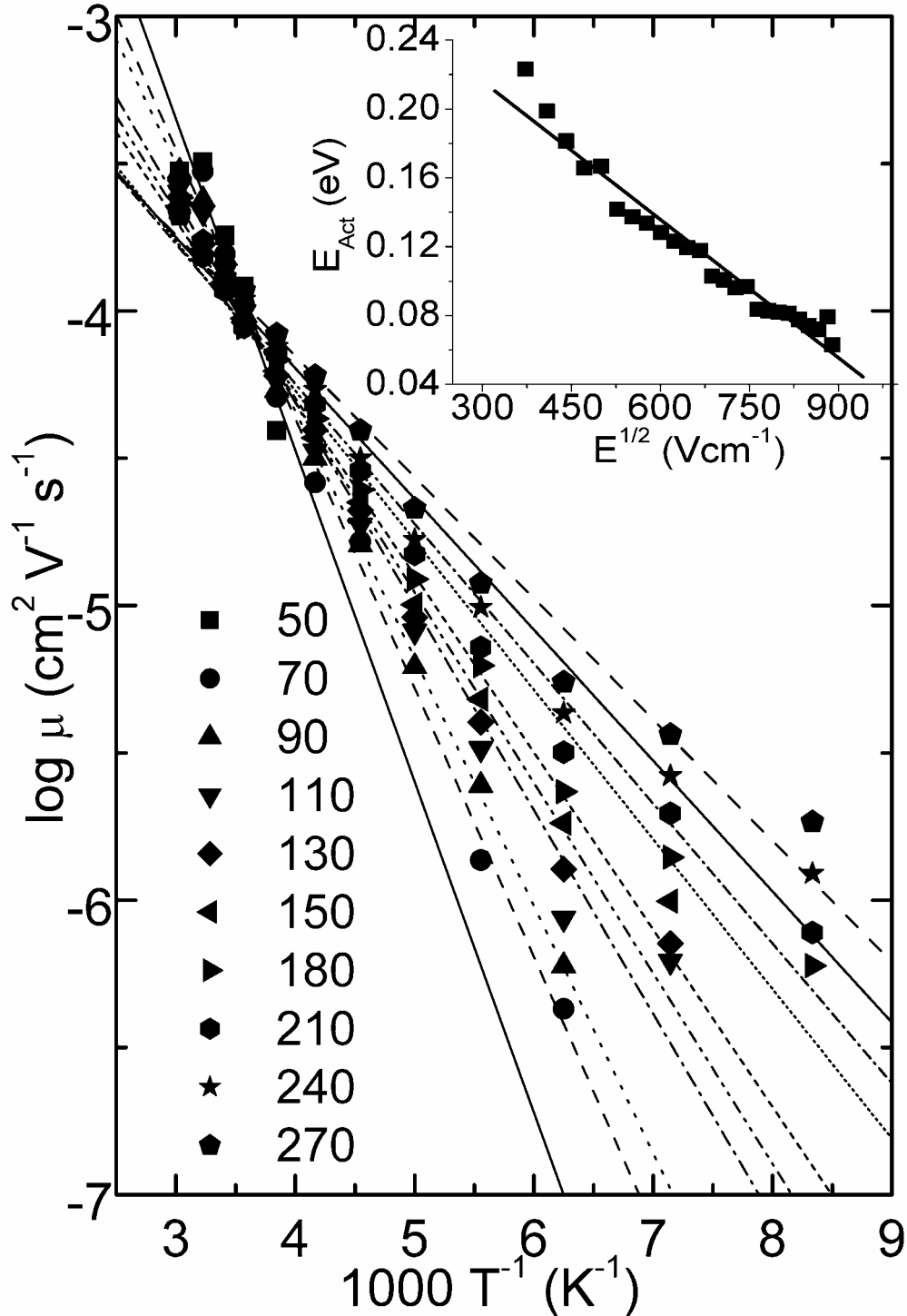


Figure 3.18: Arrhenius plots of mobility at various applied voltages determined for the H. C. Starck P3HT polymer. The inset shows the apparent activation energy versus squared electric field according to Gill's model.

The parameters of the Gill's model for P3HT from different sources are compared in Table 3.2.

TABLE 3.2: Determined values of μ_0 (prefactor mobility), T_0 , Δ (zero field activation energy) and β_{PF} of the Gill's model (eq. 1.3).

<i>Sample</i>	$\mu_0 [cm^2 V^{-1} s^{-1}]$	$T_0 [K]$	$\Delta [eV]$	$\beta [eV(Vcm^{-1})^{-1/2}]$
H. C. Starck P3HT	9.3×10^{-5}	270	0.29	2.7×10^{-4}
Rieke P3HT	7.6×10^{-5}	250	0.29	2.9×10^{-4}

Generally, the values are comparable for both polymers, and they are within the determination limit of the fitting procedure. The calculated fitting parameter β_{PF} fits well to the theoretically calculated one ($\beta_{PF}=4 \times 10^{-4} eV(Vcm^{-1})^{-1/2}$).⁵¹ The above phenomenological description seems to provide reasonable description of the measured experimental data at least at higher temperatures; however the physical meaning of the parameters, particularly T_0 and μ_0 has been questioned. It was argued that the prefactor mobility (μ_0) of the Gill's model, which is a hypothetical value at infinitely high temperatures, is orders of magnitude lower than expected if compared to the mobility in crystalline organic materials, and T_0 has no physical meaning.

The logarithm of mobility extrapolated to zero electric field obtained for various P3HT samples by both CELIV and ToF technique is plotted versus $(1000/T)^2$ according to disorder formalism in Fig. 3.19. Mobility obtained for several samples yield consistent values for $T > 130K$ ($(\sigma/kT)^2 < 60$). The low temperature mobility values obtained by the ToF technique, on the other hand, tend to be higher at lower temperatures. The deviation from the predicted linear dependence of $\log \mu(E=0)$ vs. T^{-2} at lower temperatures observed by the ToF technique may be attributed to non-dispersive to dispersive transition at low temperatures. The temperature where the transition is expected to occur (T_c) can be calculated according to eq. 1.7, and using a value of $\sigma=70$ meV, $T_c=180$ K is calculated. This value corresponds well with the observed ND \rightarrow D transition indicated by photocurrent transients that no longer feature a plateau (see Fig. 3.11 and 3.12).

The CELIV values follow the $\log \mu(E=0) \propto T^{-2}$ temperature dependence at all temperatures as predicted by disorder formalism. From linear regression, parameters

μ_0 , σ , are calculated, and shown in Table 3.3 together with Σ and C calculated from linear fit of the field dependence of mobility versus the energetic disorder parameter $(\sigma/kT)^2$. The zero field mobility values as well as the electric field dependence obtained by the ToF technique were fitted above 180 K, where the relationship is well approximated by a linear relationship.

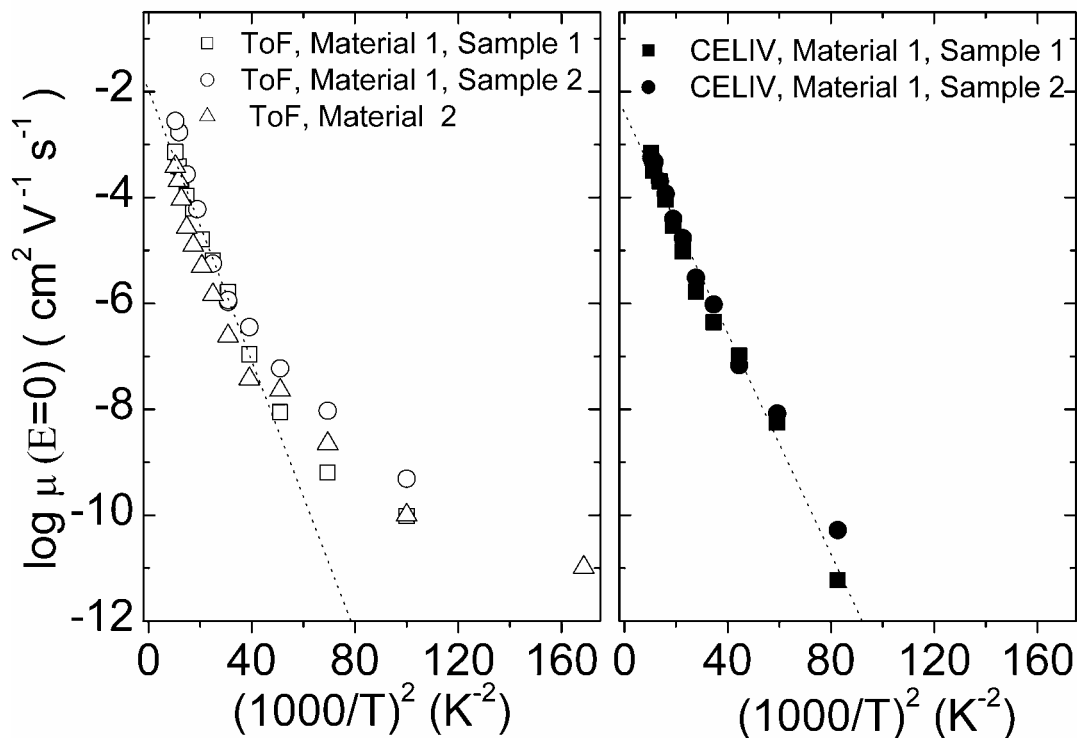


Figure 3.19: Temperature dependence of the mobility extrapolated to zero electric field determined by the CELIV (full symbols) and ToF technique (empty symbols) for P3HT obtained from different commercial sources, and with different film thickness. See Table 3.3 for more details.

The calculated values of σ are in good agreement between the measurements, which indicates that the mode of charge generation (photogeneration in the ToF, and doping induced charge carriers in P3HT) does not alter the density of states distribution significantly, at least in this regime, where the conductivity ($\sim \sigma_c = 10^{-8} \text{ } \Omega^{-1} \text{ cm}^{-1}$) and the carrier concentration ($\sim n = 10^{14} - 10^{15} \text{ cm}^{-3}$) is considered to be rather low. Furthermore, the calculated prefactor mobility values agree reasonably well between the two experiments. Considering the principal differences by the two applied methods, this finding suggests that charge carrier motion does not depend on the mode of charge generation in the regioregular P3HT samples under the presented experimental conditions.

TABLE 3.3: Determined values of μ_0 (prefactor mobility), σ (energetic disorder), C (fit constant) and Σ (positional disorder parameter) of the disorder formalism (eq. 1.6) obtained by CELIV and ToF techniques for samples with various thickness.

<i>Material / Sample</i>	<i>Method</i>	μ_0 ($cm^2V^{-1}s^{-1}$)	σ (meV)	C ($(cmV^2)^{1/2}$)	Σ	<i>Thickness</i> (μm)
1/1	CELIV	4×10^{-3}	63	3.6×10^{-4}	3	1.3
1/2	CELIV	4×10^{-3}	61	3.6×10^{-4}	3.15	1.3
1/1	ToF ^a	1×10^{-2}	70	1.5×10^{-4}	3.4	4.6
1/2	ToF ^a	5×10^{-2}	74	2.1×10^{-4}	3.9	6.4
2/1	ToF ^a	5×10^{-3}	73	1.4×10^{-4}	3	3.6
2/2	ToF ^a	7×10^{-3}	75	1.4×10^{-4}	3	6.5

^aCalculated between 310 K – 180 K temperature region.

3.3 Summary

In summary, the temperature and electric field dependence of the mobility has been studied in conjugated polymers. The film morphology is shown to influence the charge transport properties as it is indicated by the factor of 3.5 higher room temperature mobility of a regioregular MDMO-PPV polymer. It is suggested that the ordered nano-aggregates embedded in an otherwise amorphous matrix is responsible for the improved charge transport properties. The same ordered regions, on the other hand, may serve as charge carrier traps at lower temperatures resulting in stronger temperature dependence of the mobility.

Negative electric field dependence of mobility has been first time clearly demonstrated in conjugated, semiconducting polymers. The comparative study of the temperature and electric field dependence of mobility reveals that such phenomena is not related to artifacts of the ToF technique, but rather an intrinsic property of the materials studied. The overall agreement between the ToF and CELIV technique shows that these experimental techniques are mutually consistent, even though the mode of charge generation is principally different.

Chapter 4

4. Mobility and Recombination in Bulk Heterojunction Solar cells

4.1 Introduction

The aim of this study to determine the charge carrier mobility (μ) and lifetime (τ) of the photogenerated charge carriers in operational bulk heterojunction solar cells. The experimental techniques (ToF and CELIV) that were used to measure charge carrier mobility in conjugated polymers are not suitable for this purpose. The ToF technique is limited to rather thick samples, *i.e.* $\sim 1 \mu\text{m}$ at the absorption maximum, which is at least 3-10 times higher than the optimum performance of bulk heterojunction solar cells requires. Both mobility and solar cell performance may exhibit strong morphology dependence. The morphology may vary depending on the film preparation conditions, *e.g.* concentration of the solution, drying time, *etc.* In addition, the concentration of charge carriers in a ToF technique is limited to 10% of the capacitive charge, which limits the concentration in a typical device configuration to $n \sim 10^{14} \text{ cm}^{-3}$. This concentration is 2-3 orders of magnitude lower than charge carrier concentration in a solar cell under AM 1.5 illumination conditions.

The CELIV method can be applied to films that have a comparable thickness as used in the state-of-the-art bulk heterojunction solar cells (100 – 300 nm). The CELIV technique, on the other hand, requires significant amount of free charge carriers in the dark, which is undesired in organic photovoltaic devices (the devices should not short). Therefore, the novel photo-CELIV technique has been introduced,

in which charge carriers are photogenerated by a short laser flash, and extracted under a reverse bias voltage pulse.

4.2 Photo-CELIV Measurements at RT

The three different stages during the photo-CELIV technique are illustrated in Fig. 4.1. Initially (stage 1), charge carriers are photogenerated via photoinduced charge transfer. During the second, equilibration stage, the charge carriers recombine under zero electric field condition. The zero field condition is achieved by compensating the built-in field of the device by the application of a forward bias offset voltage (U_{offset}). Simultaneously, the charge carriers may relax towards the tail states of the distribution via energy relaxation. In stage 3, the remaining charge carriers are extracted by a reverse bias voltage pulse, and from the time when the extraction current reaches its maximum, the mobility can be calculated.

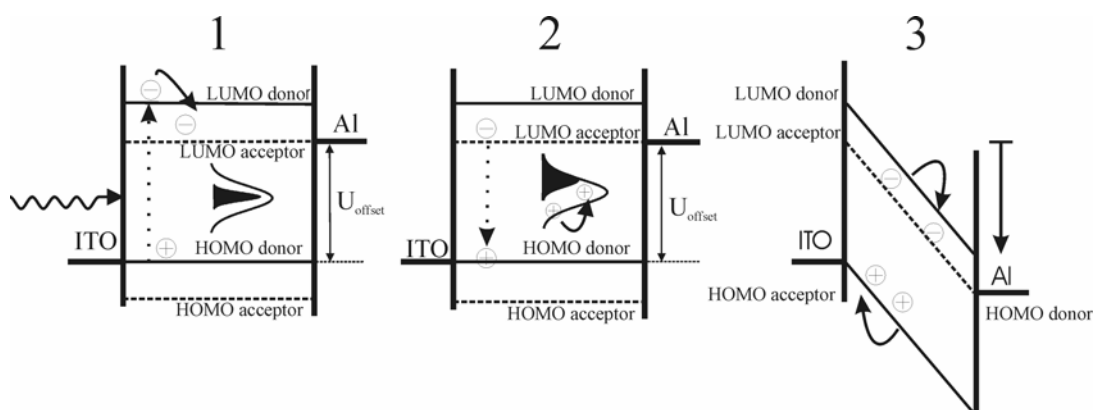


Figure 4.1: The three main stages during a photo-CELIV technique: 1 charge generation; 2 charge recombination and energy relaxation; 3 charge extraction.

The effect of U_{offset} on the recorded photo-CELIV curves is shown in Fig. 4.2. The sandwich type device was a typical of a bulk heterojunction solar cell (ITO/PEDOT-PSS/MDMO-PPV:PCBM (1:4)/ Al), and the thickness of the active layer was 265 nm. The absorption coefficient of the photoactive layer at 532 nm excitation wavelength is $4 \times 10^4 \text{ cm}^{-1}$, corresponding to OD ~ 1 , thus bulk generation of charge carriers. The RC constant of the setup was around $2 \times 10^{-8} \text{ s}$. The delay time (t_{del}) between the light pulse and the linearly increasing voltage ramp ($A=4 \text{ V}/20 \mu\text{s}$) was 5 μs . At short circuit conditions (0 V applied voltage), most of the photogenerated charge carriers exit the device prior to the reverse bias voltage pulse under the

influence of the built-in field of the device (photoconductivity). Applying 0.9 V, the photocurrent upon photoexcitation is minimal (flat band conditions), and the extraction current due to the reverse bias voltage pulse is increased. Finally, the photocurrent turns to negative when $U_{\text{offset}} > 0.9$ V, which indicates that the charge carriers are electric field driven. In addition, significant injection current flows shown by the non-zero offset current. The injected charge carriers are also extracted under the CELIV pulse together with the photogenerated ones. Experimentally, U_{offset} is chosen close to the built-in field of the device, yet slightly smaller in order to avoid dark injection, which complicates the evaluation of the photo-CELIV curves. It is worth mentioning that the built-in field could be more precisely compensated in devices without PEDOT-PSS hole injection layer. Nevertheless, no significant difference in the mobility values and its time and concentration dependence has been observed between devices with or without PEDOT-PSS.

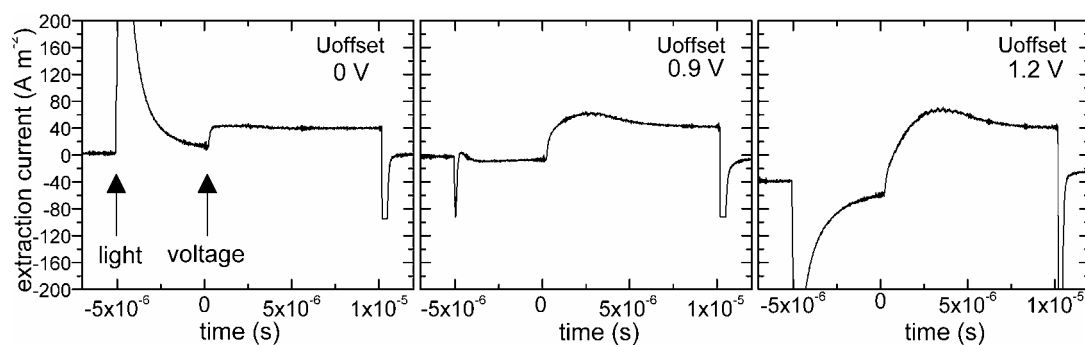


Figure 4.2: The effect of U_{offset} on the recorded photo-CELIV curves at 5 μs fixed delay time.

Figure 4.3 A, shows recorded photo-CELIV curves as a function of delay time. The U_{offset} during these measurements were 0.75 V. The maximum of the extraction current (Δj) is decreasing with increasing delay time indicative of charge carrier recombination, and t_{max} shift slightly to longer times. In Fig. 4.3 B, the photo-CELIV transients recorded at varying light intensity and at fixed 5 μs delay time are shown. The maximum of the extraction current is constant until the threshold light intensity of $\sim 1 \mu\text{J}/\text{cm}^2/\text{pulse}$, and decreases constantly at lower light intensities. In contrary to the results obtained by the delay time dependent measurements, the t_{max} at various light intensities remain almost constant. Finally, in Fig. 4.3 C, the photo-CELIV curves recorded as a function of the maximum of the applied voltage pulse (U_{max}) at fixed 15 μs delay time, and fixed light intensity are shown. The t_{max} is shorter when the

maximum of the voltage pulses is increased indicating the voltage (field) dependence of the mean charge carrier velocity.

The obtained mobility values are plotted versus delay time in Fig. 4.4 A. The mobility is decreasing with t_{del} till 10 μs , and remains almost unchanged for longer delays. In Fig. 4.4 B, the mobility is plotted as a function of the concentration of extracted charge carriers obtained by the intensity dependent photo-CELIV measurement. Clearly, the rather strongly increasing mobility at short time delays in Fig. 4.4 A, does not correspond to the weak concentration dependence of the mobility in Fig. 4.4 B. Figure 4.4 C shows the voltage (field) dependent of mobility for two different delay times i) 5 μs and ii) 15 μs . The electric field dependence of mobility at longer delay times is a typical positive dependence as expected for an amorphous semiconductor, yet at short delays show an anomalous negative dependence.

The number of extracted charge carriers is calculated from the delay time dependent photo-CELIV curves, and plotted versus t_{del} (top x axis) or $t_{\text{del}} + t_{\text{max}}$ (bottom x axis) in Fig 4.5. The concentration decay was fitted according to:

$$\frac{dn}{dt} = -\frac{n}{\tau} - \beta n^2 \quad (4.1)$$

where τ is the monomolecular lifetime, β is the bimolecular recombination coefficient, and n the density of photogenerated charge carriers. The solution to eq. 4.1 is written as $n(t) = ([\beta\tau + 1/n_0] \exp[t/\tau] - \beta\tau)$, with n_0 being the initial photogenerated charge carrier density. The obtained fitting parameters were $\beta=5.96 \times 10^{-11} \text{ cm}^3/\text{s}$ and $\tau=130\mu\text{s}$ using t_{del} as x axis, and $\beta=3.83 \times 10^{-11} \text{ cm}^3/\text{s}$ and $\tau=30\mu\text{s}$ using $t_{\text{del}} + t_{\text{max}}$. Plotting the number of charge carriers versus t_{del} , the recombination during extraction is neglected; therefore β and τ may be overestimated if t_{del} and t_{max} is comparable. In the second case ($t_{\text{max}}+t_{\text{del}}$), the same recombination mechanism is assumed during equilibration (stage 2 in Fig. 4.1) and extraction (stage 3). Thus β and τ may be underestimated because during extraction, the charge carriers are pulled away from each other towards the corresponding electrodes reducing the probability to meet and recombine. Based on the above arguments, the realistic β and τ values are expected to be within the range of $5.96 \times 10^{-11} \text{ cm}^3/\text{s} > \beta > 3.83 \times 10^{-11} \text{ cm}^3/\text{s}$, and $130\mu\text{s} > \tau > 30\mu\text{s}$.

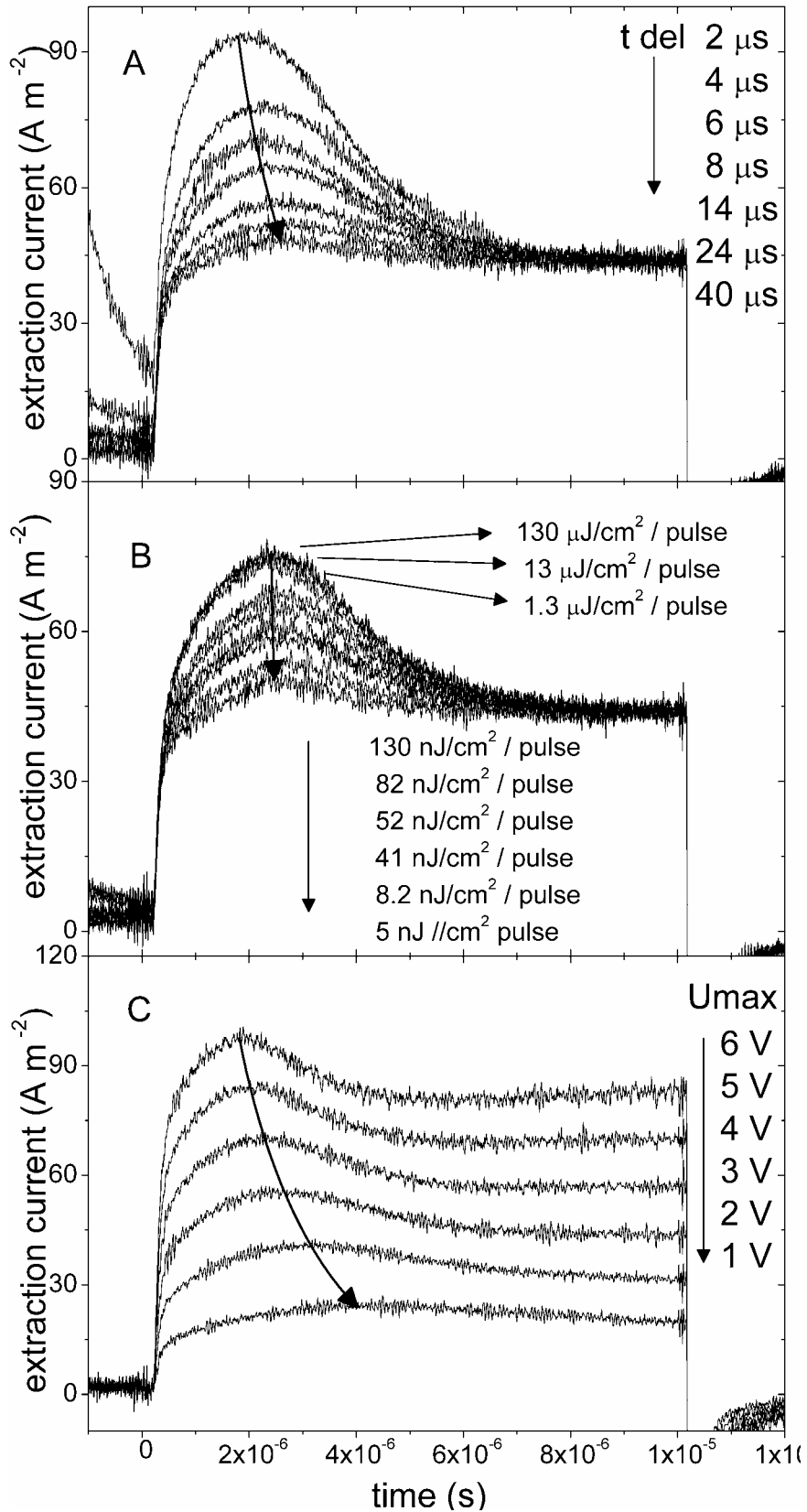


Figure 4.3: Recorded photo-CELIV curves as a function of a) delay time b) incoming light intensity at fixed 5 μ s delay time c) applied maximum voltage (U_{max}) at fixed 15 μ s delay time and fixed light intensity.

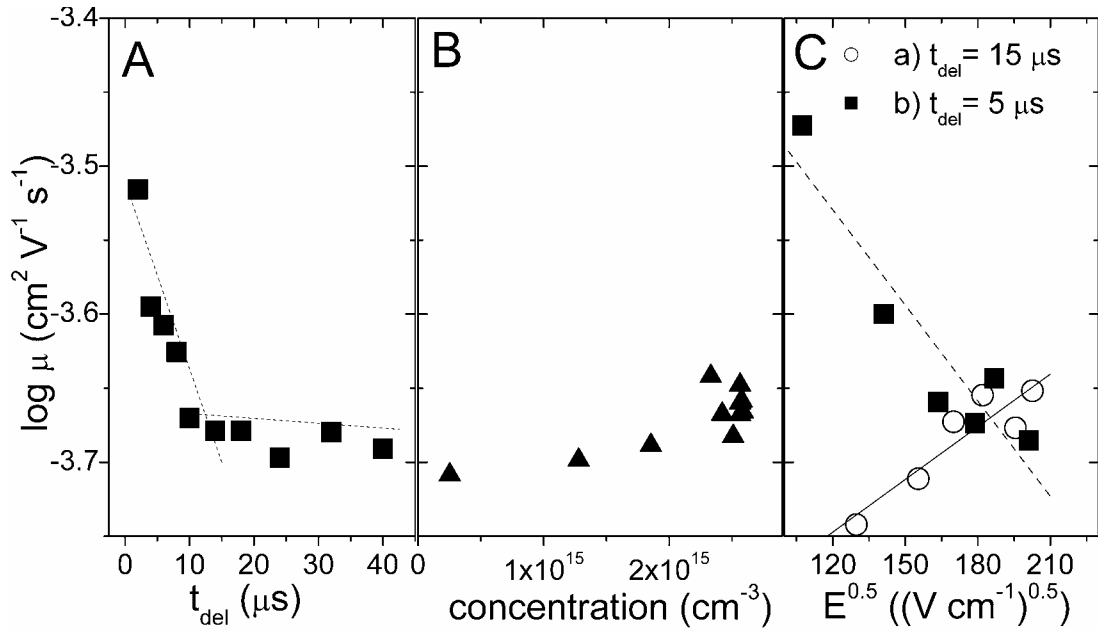


Figure 4.4: The mobility values versus A) delay time B) charge carrier concentration determined from intensity dependent measurement C) and square root of the electric field at a) 15 μs delay time b) 5 μs delay time.

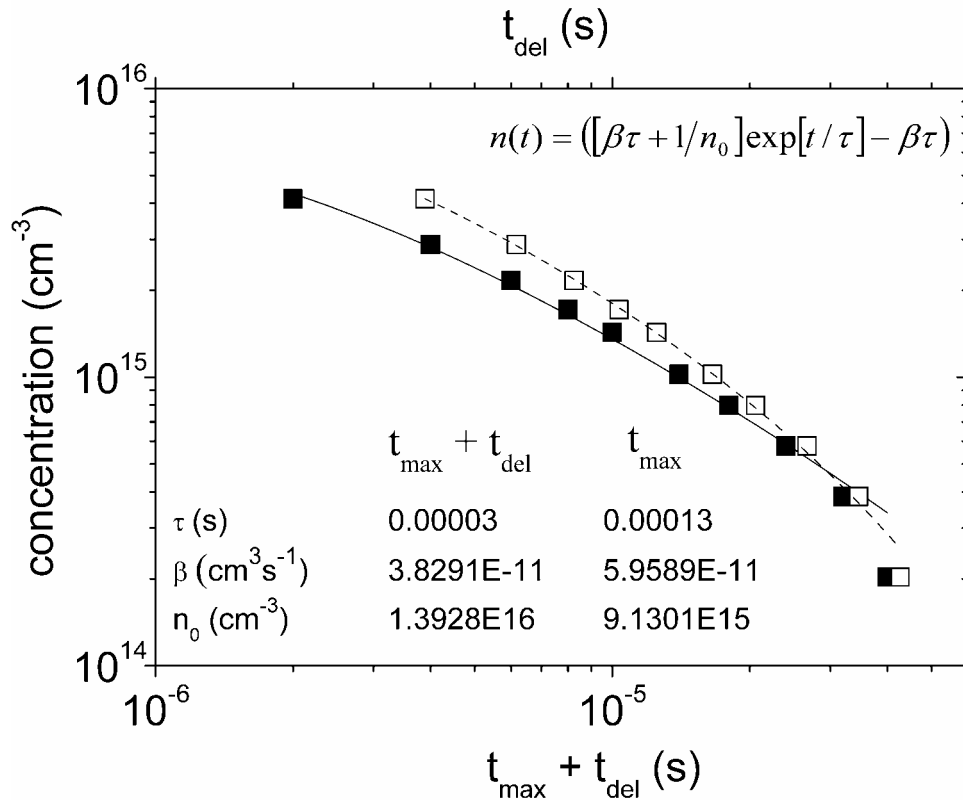


Figure 4.5: Concentration of the charge carriers calculated from delay time dependent photo-CELIV curves versus t_{del} (■) or $t_{\text{del}} + t_{\text{max}}$ (□). The inset shows the fit parameters according to eq 4.1.

The decreasing mobility at short time scales cannot be attributed to the concentration (occupational density) dependence of mobility, which is expected to play a role in amorphous semiconductors due to for *e.g.* trap filling effects. It may be related to the time dependent energy relaxation of the charge carriers. Further indication that energy relaxation may play a role in the delay time dependent photo-CELIV measurements are given by the temperature dependence studies.

4.3 Temperature Dependence Studies

4.3.1 Delay time dependence of the mobility

Figure 4.6 shows the photo-CELIV curves recorded as a function of delay time at 300 K and at 150 K. The thickness of the active layer of the sandwich type device (ITO/MDMO-PPV : PCBM (1:4)/Al) was 360 nm. The active layer was spin coated directly on the ITO coated glass substrates (without PEDOT-PSS interfacial layer) for this temperature dependence studies, which structure was found to be more suitable at low temperature measurements due to better blocking contacts. The applied U_{offset} voltage was 0.7 V at both temperatures. This value is very close to the open circuit voltage of the device at 300 K (note the negligible photoconductivity upon photoexcitation). The photoconductivity is slightly increased at 150 K, which indicates that the V_{oc} is slightly higher at lower temperatures. The t_{max} shifts to longer times as the delay time is increased at both temperatures. Moreover, the photogenerated charge carriers can be extracted even after 20 ms at 150 K, which shows that the lifetime of the charge carriers is significantly increased. The photo-CELIV transients are non-dispersive at room temperature, and the majority of the photogenerated charge carriers can be extracted by the extraction pulse at all delay times. This is not the case at 150 K, when the extraction current does not reach the capacitive current value at the end of the extraction pulse. This shows that some portion of the charge carriers is trapped at lower temperatures, and could not be extracted within the applied time (frequency) window. Moreover, the photo-CELIV transients are generally more dispersive at lower temperatures.

Figure 4.7 A shows the determined mobility versus delay time (t_{del}) at various temperatures. The mobility is decreasing with increasing delay time. At short times, the decay is faster, and a “kink” is observed. The “kink” moves towards longer times at lower temperatures, and the difference between the slopes prior and after the kink seems to smear out at lower temperatures. The “kink” appears at around 2 μs at room temperature, 30 μs at 180 K and 115 μs at 120 K.

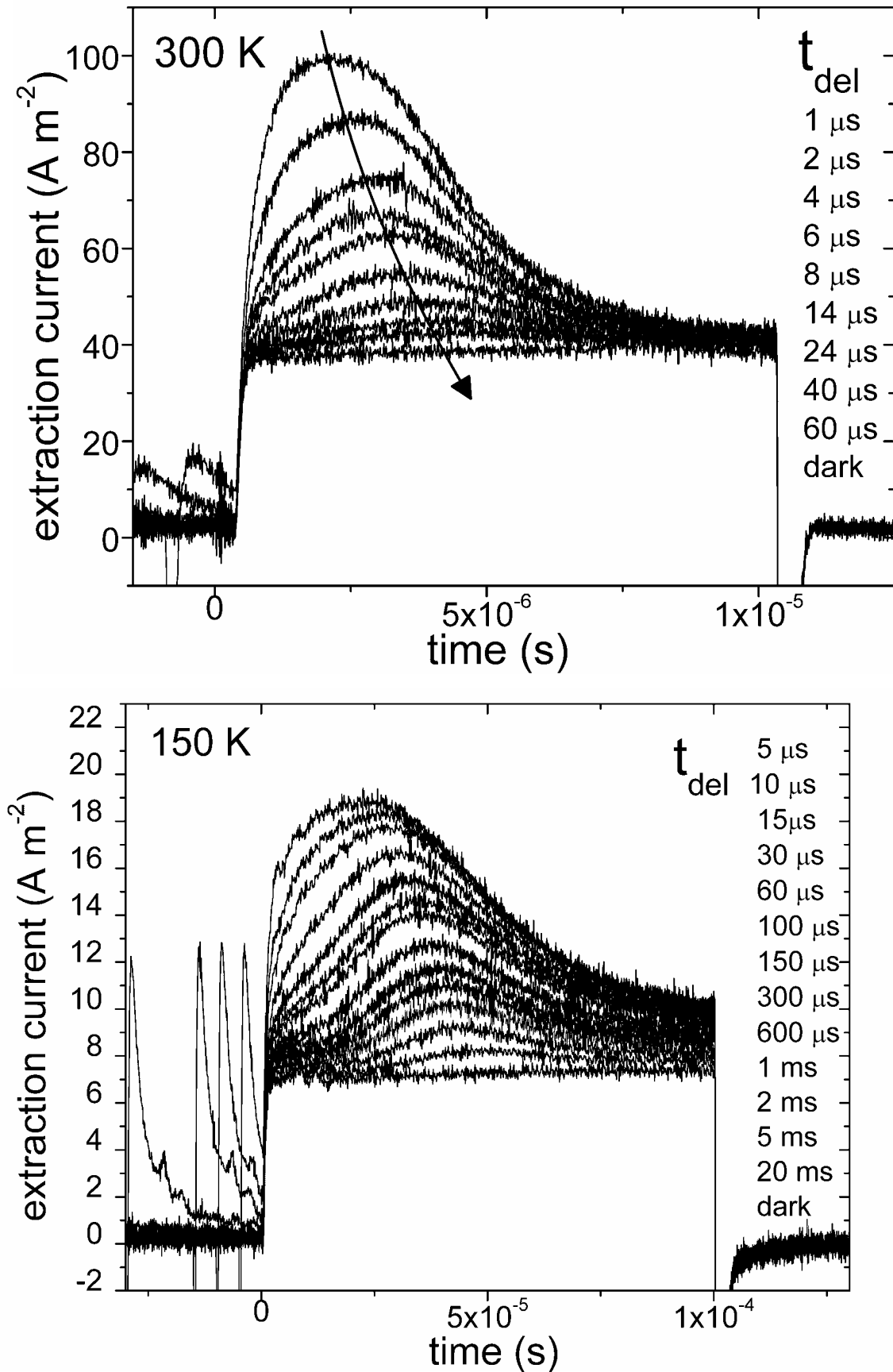


Figure 4.6: Delay time dependent photo-CELIV curves recorded at 300 K and 150 K.

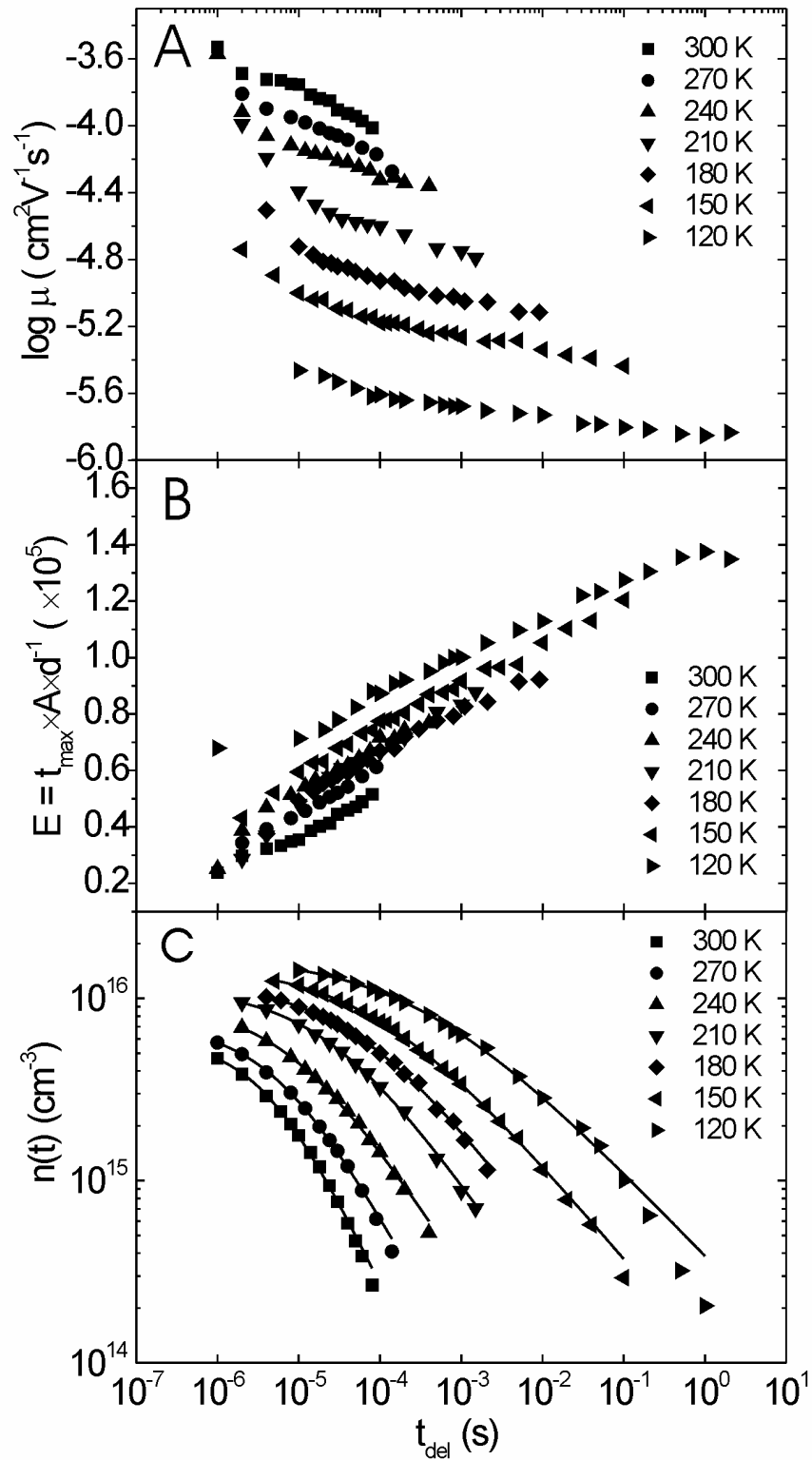


Figure 4.7: A, The mobility; B, the electric field; and C, the charge carrier concentration versus delay time determined at various temperatures.

Figure 4.7 B shows the electric field calculated during the delay dependent photo-CELIV measurements as $E=(A \times t_{\max})/d$. The electric field increases with increasing time delays at all temperatures due to the shift of t_{\max} to longer times. Fig. 4.7 C shows the concentration decay of the photogenerated charge carriers calculated from the delay time dependent photo-CELIV curves at various temperatures. At room temperature, the non-dispersive bimolecular rate equation (eq 4.1) gives a meaningful fit, however, at low temperatures the quality of the fit strongly degrades. The observed time dependent mobility in Fig. 4.7 A suggests that a time dependent (dispersive) bimolecular recombination should be more appropriate.

The time dependent (dispersive) bimolecular rate equation used further on is written as:

$$\frac{dn}{dt} = -\beta(t)n^2 \quad (4.2)$$

If a power law decay of the $\beta(t)$ is assumed in the form:

$$\beta(t) = \beta_0 \times t^{-(1-\gamma)} \quad (4.3)$$

The solution to 4.2 is given as:

$$n(t) = \frac{n_0}{1 + \left(\frac{t}{\tau_B}\right)^\gamma} \quad (4.4)$$

where $n(0)$ is the initial photogenerated charge carrier density, and τ_B is the bimolecular lifetime expressed as:

$$\tau_B = \left(\frac{\gamma}{n(0) \times \beta_0}\right)^{\frac{1}{\gamma}} \quad (4.5)$$

The parameter γ , ($0 < \gamma < 1$) describes dispersion. A meaningful fit is obtained at all temperatures as shown by the solid lines in Fig. 4.7 C, which is remarkable considering the concentration decay measured within almost 6 decades of time. The $n(0)$ as well as the obtained dispersion parameter (γ) is calculated according to eq. 4.4, and plotted versus temperature in Fig. 4.8.

The calculated $n(0)$ decreases with increasing temperatures almost linearly. The dispersion parameter γ is close to 1 at room temperature, which corresponds to a non-dispersive (time independent) bimolecular recombination rate and it is decreasing with decreasing temperatures to around 0.45 at 120 K. The increasing dispersion with decreasing temperatures is supported by the observed change of the shape of the photo-CELIV transients (Fig. 4.6).

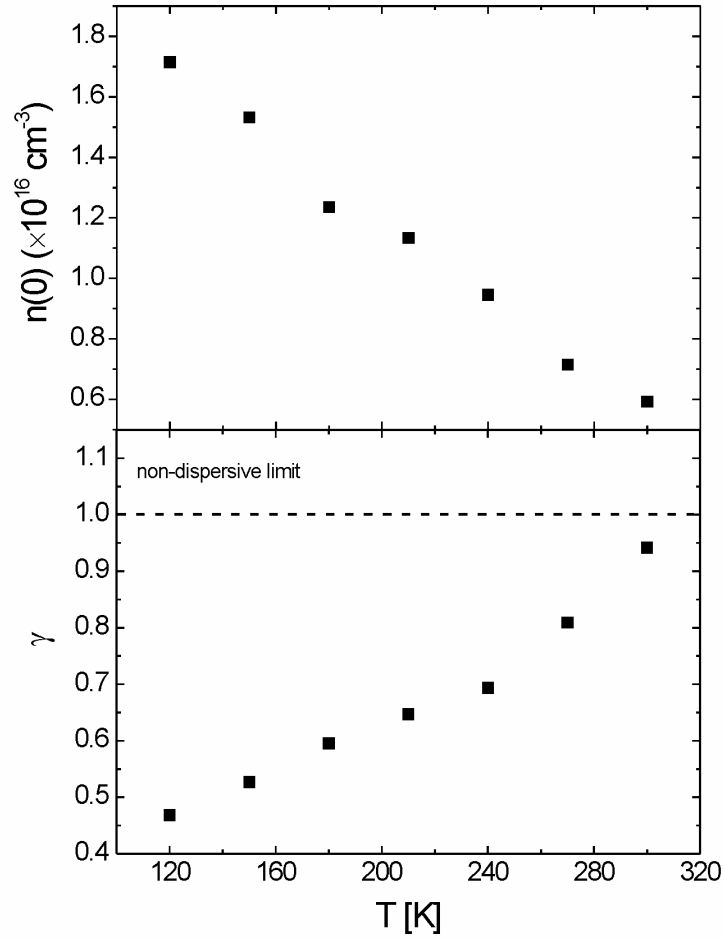


Figure 4.8: The temperature dependence of $n(0)$ and the dispersion parameter γ .

Substituting the determined γ values into eq. 4.3, the time dependent bimolecular recombination rate $\beta(t)=\beta_0 \times t^{-(1-\gamma)}$ is calculated, and plotted versus time in Fig. 4.9 (solid lines).

The functional dependence of $\beta(t)$ can also be directly determined from the measured concentration decay. After rearrangement of eq. 4.2, $\beta(t)$ is written as:

$$\beta(t) = -\left(\frac{dn}{dt}\right)/n^2 \quad 4.6$$

Both dn/dt and n^2 can be directly calculated from Fig. 4.7 C, and the obtained $\beta(t)$ values according to eq. 4.6 are plotted as the scattered data in Fig. 4.9. The scattered data correspond well with the power law decay according to Eq. 4.3.

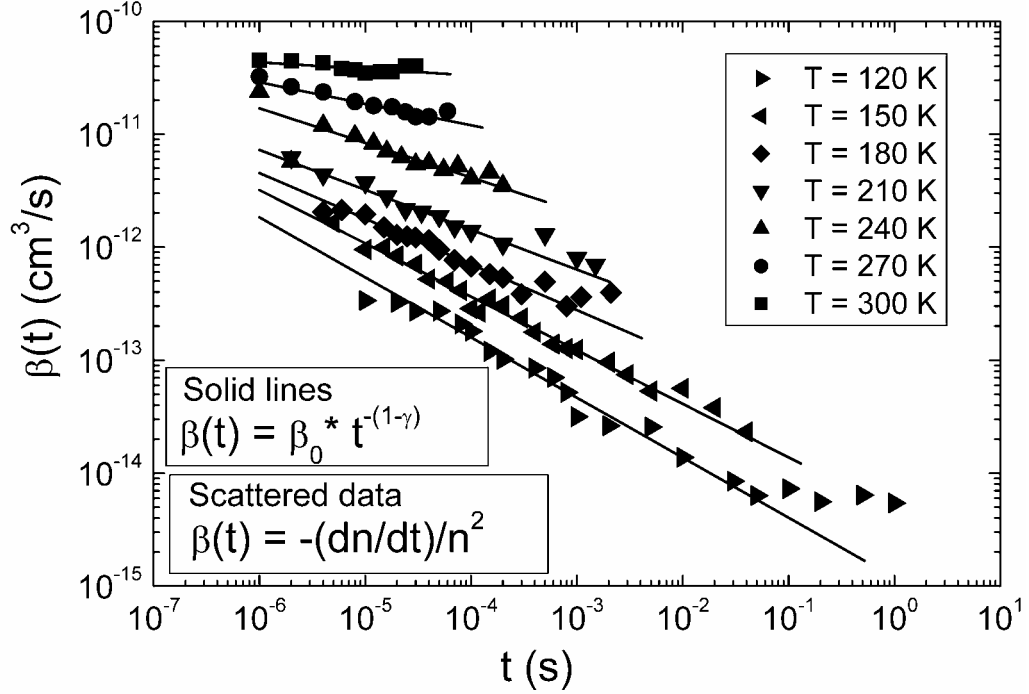


Figure 4.9: The bimolecular recombination coefficient versus delay time. The solid lines and the scattered data are calculated according to eq. 4.3, and eq. 4.6, respectively.

Although the general features of the time dependence of the mobility $\mu(t)$ is recovered in the time dependence of the bimolecular recombination rate $\beta(t)$, there are some differences. First of all, the observed kink in the logarithm mobility versus delay time is not reproduced in $\beta(t)$, which seems to follow a power law decay over the whole measured time scale. Moreover, the slopes of the $\beta(t) \sim t^{-(\gamma-1)}$ is decreasing with decreasing temperature, meanwhile the slope of the $\mu(t) \sim t^{-\alpha}$ follows the opposite trend (see Fig. 4.10). A likely reason for this discrepancy is that the mobility using the photo-CELIV technique is determined at a certain non-zero electric field as it is shown Fig. 4.7 B. The recombination, on the other hand is measured at zero field condition (flat bands), therefore a meaningful comparison between $\beta(t)$ and $\mu(t)$ requires the calculation of the zero-field μ values at various delay times (see Chapter 4.3.3). Finally, the bimolecular recombination rate ($k_B=1/\tau_B$) is calculated using eq.

4.4, and plotted versus inverse temperature in Fig. 4.11. The relationship indicates Arrhenius type activation with activation energy of 77 meV.

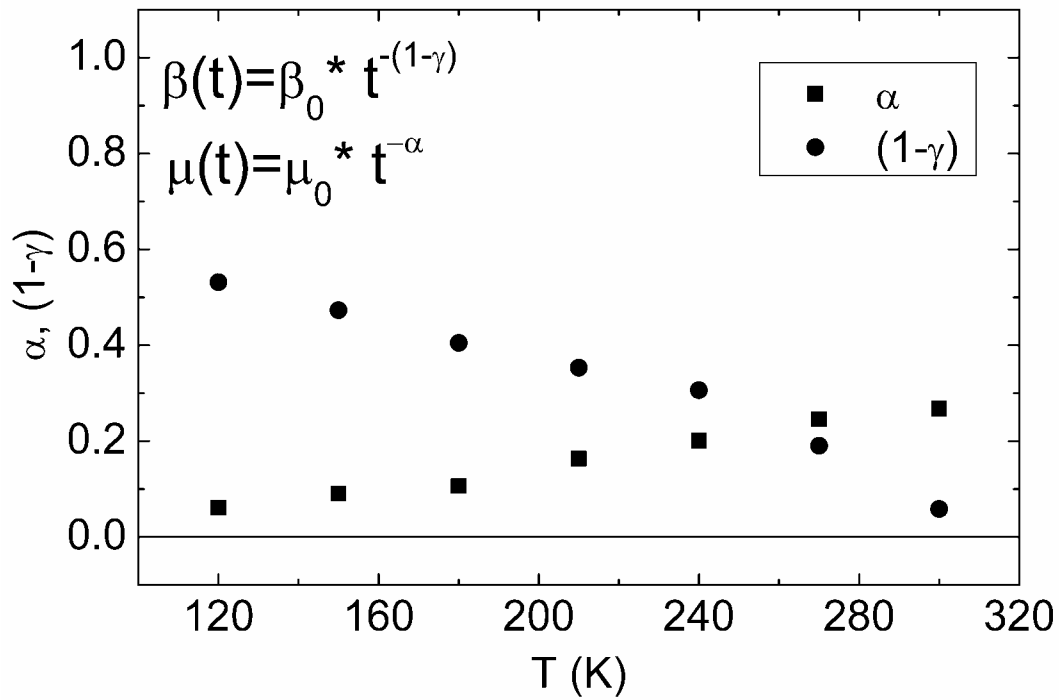


Figure 4.10: The temperature dependence of the slope of the time dependence of mobility (α) as well as the bimolecular recombination rate ($1-\gamma$).

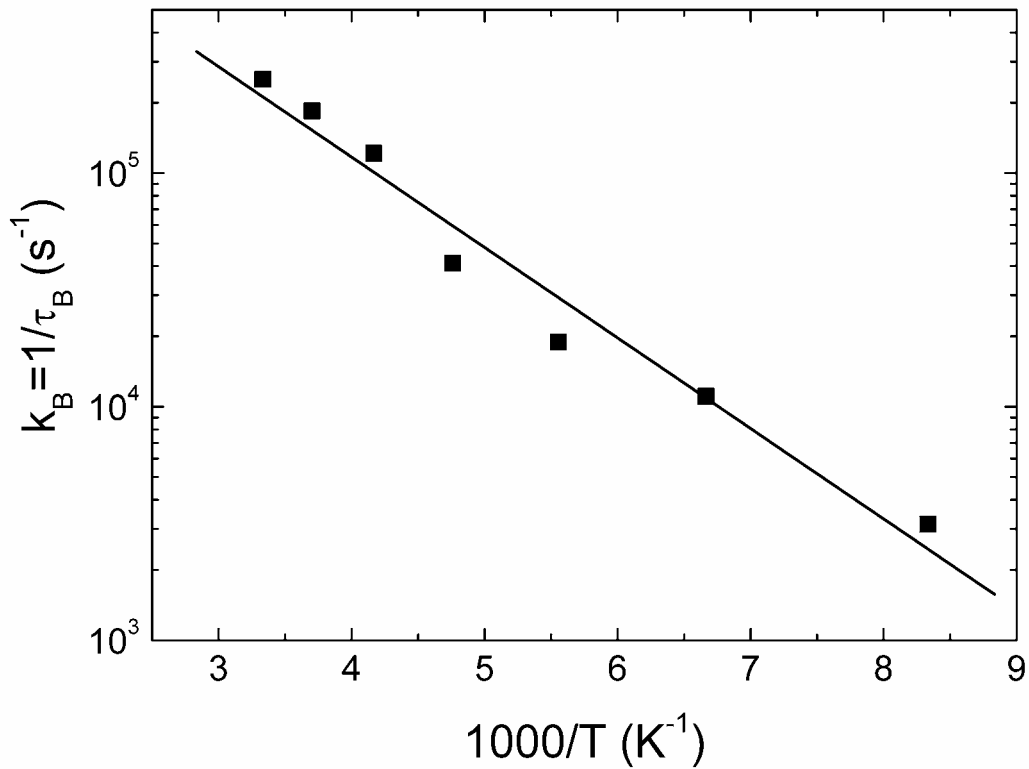


Figure 4.11: The temperature dependence of the bimolecular recombination rate.

4.3.2 Charge carrier concentration dependence of the mobility

The time dependent mobility in Fig. 4.7 A may be related to the charge carrier concentration (occupational density) dependence of the mobility, since less charge carriers are extracted at longer time delays due to charge carrier recombination. Alternatively, it may be related to the time dependent energy relaxation of the charge carriers towards the tails states of the distribution. To check the effect of charge carrier concentration alone, the charge carrier mobility was studied by fixing the delay time between the light pulse and the voltage pulse, and changing the light intensity by using optical density filters. Fig. 4.12 shows the recorded photo-CELIV transients at various light intensities at 300 K, and at 150 K. The delay time between the light pulse and the voltage pulse was 5 μs at 300 K, and 500 μs at 150 K. The time to reach the maximum of the extraction current (t_{max}) at 300 K is almost independent of the light intensity. At 150 K, the t_{max} shifts to longer times as the light intensity is decreased. Similarly to the room temperature measurements in Chapter 3.2.2, the maximum of the extraction current does not change significantly by decreasing the light intensity by two orders of magnitude ($\sim 1 \mu\text{J}/\text{cm}^2$ / pulse (OD 2), and starts to decrease constantly below this threshold intensity.

Transient absorption studies identified a fast ($<1\mu\text{s}$), and a slow (μs –ms) component of the recombination dynamics of the photoinduced charge carriers in the blend of MDMO-PPV:PCBM.²⁹ At short timescales ($<1\mu\text{s}$), a light intensity dependent and mostly temperature independent recombination mechanism was identified, followed by a power law decay with an exponent $\alpha=0.45$ on the μs to ms timescale at room temperature. It was observed that the amplitude of the power law tail saturated with increasing light intensity at around $1\mu\text{J}/\text{cm}^2/\text{pulse}$. These features of the recombination dynamics have been reproduced using a Monte Carlo simulation technique based on a multiple trapping model within a bimodal density of states.⁹⁷ It was assumed that the mobile charge carriers generated initially within the intrinsic density of states (above mobility edge) undergo fast recombination or alternatively, are trapped within a manifold of exponential distribution of trap states (below mobility edge) with a concentration of 10^{17}cm^{-3} .³⁰

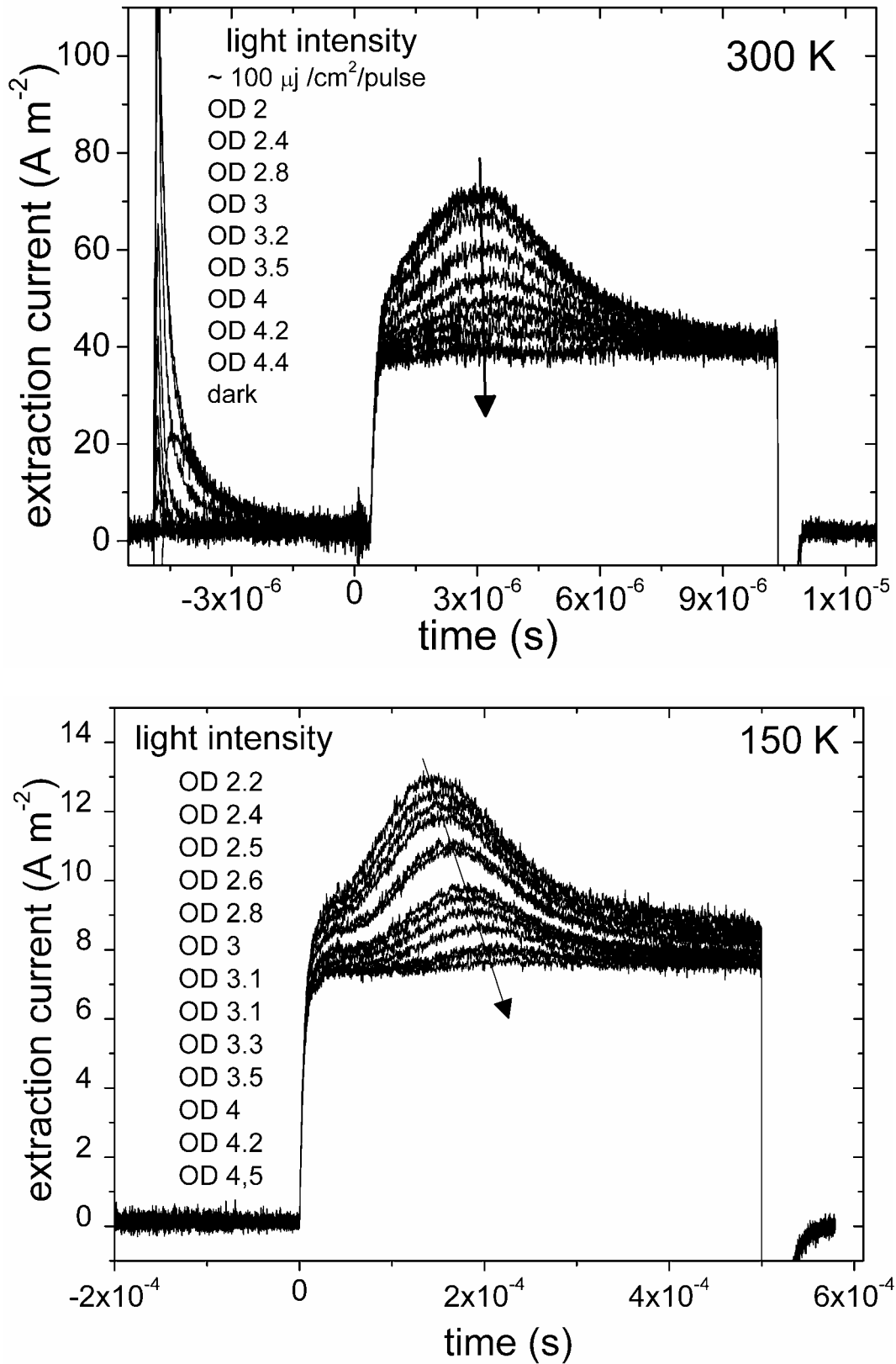


Figure 4.12: Recorded Photo-CELIV transients at various light intensities at 300 K and 150 K.

The shortest delay time in the photo-CELIV measurement was 1 μs , therefore in the photo-CELIV measurements the charge carrier mobility and recombination of the long-lived charge carriers is probed. The observed saturation of the extraction current at higher light intensities is then consistent with the reported transient absorption studies. The observed (weak) temperature dependence of $n(0)$ in Fig. 4.8 may be related to a weak temperature dependence of the initial, fast recombination ($>1\mu\text{s}$).

The mobility versus the concentration of charge carriers calculated from A, the light intensity dependent photo-CELIV curves and B, delay time dependent photo-CELIV curves is shown Fig. 4.13 at various temperatures. The mobility is mostly concentration independent at room temperatures, and becomes slightly dependent at lower temperatures with an almost constant slope. The concentration dependence of mobility obtained from the delay time dependent measurement does not correspond to the concentration dependence of mobility from intensity dependent measurements, especially at higher concentrations (short delay times). This result indicates that the more strongly increasing mobility at short times in the $\log \mu$ versus t_{del} plots (Fig. 4.6) cannot be attributed to the concentration dependence of mobility alone. The possible effect of spatially non-uniform charge generation was also checked by changing the excitation wavelength of the laser. Instead of 532 nm, the 355 nm excitation wavelength was used, where the absorption coefficient is different. However changing the excitation wavelength did not change the time dependence of the mobility at short delay times. Therefore, it is attributed to fast relaxation of the charge carriers towards a manifold of states below the mobility edge, followed by a slower decay within the trap states.

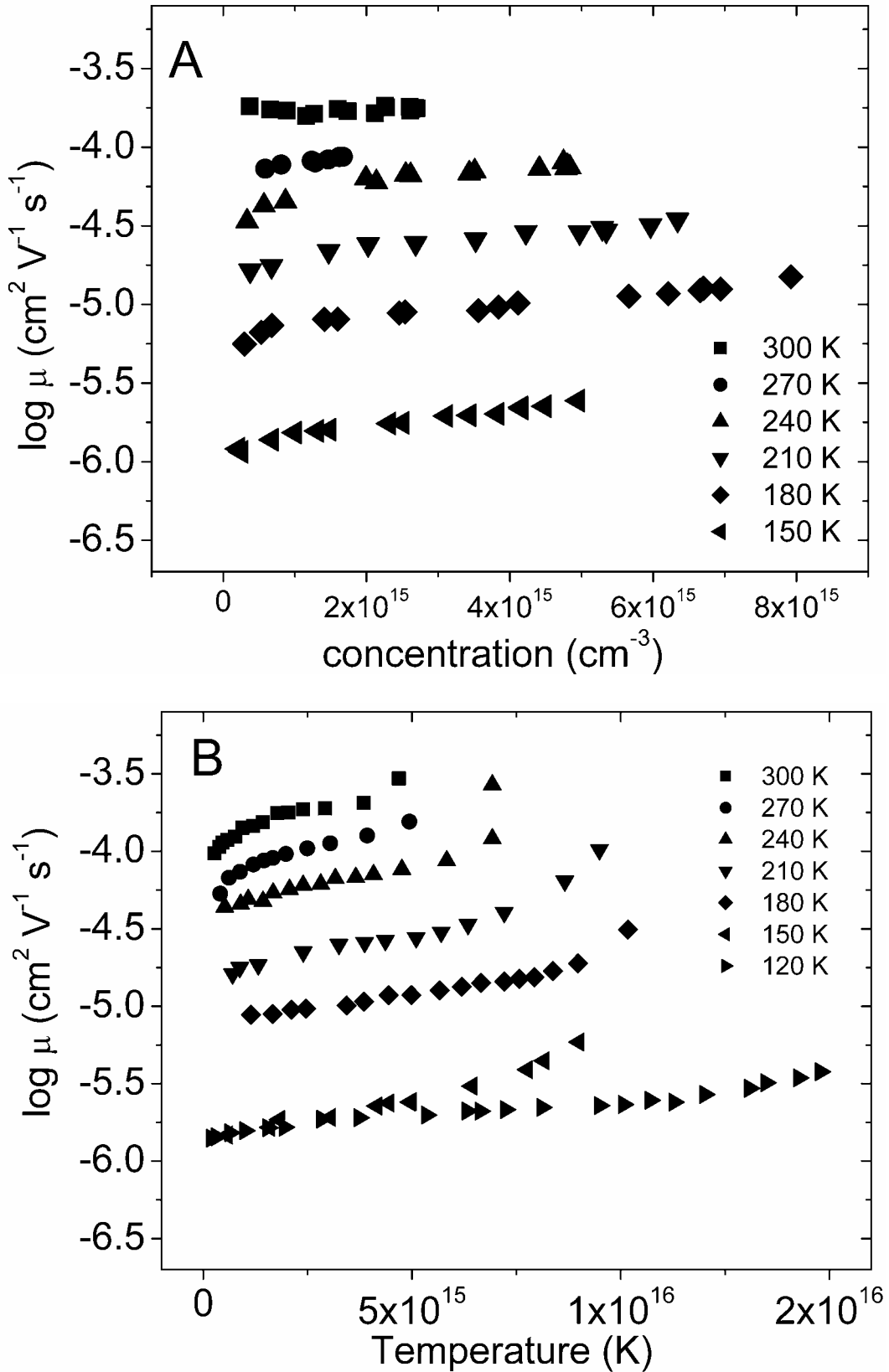


Figure 4.13: The mobility versus charge carrier concentration obtained from A, light intensity dependent photo-CELIV measurements; B, delay time dependent photo-CELIV measurement.

4.3.3 Voltage (field) dependence of the mobility

In this experiment, the voltage (field) dependence of mobility was investigated at constant delay time and light intensity. Fig. 4.14 shows the recorded photo-CELIV curves versus the maximum of the applied voltage at fixed delay time and light intensity at 300 K, and 150 K. The delay time was 15 μs at 300 K, and 500 μs at 150 K. The maximum of the extraction current shifts to longer times as the maximum of the voltage pulse decreases at all temperatures, which is indicative of the voltage (field) dependence of the charge carrier mean velocity. It is observed that the field dependence of the mobility depends on the delay time. The field dependence at short delay times is weaker than at longer time delays, or even a negative dependence as it is shown in Fig. 4.4.

The mobility is plotted versus the square root of the electric field at various temperatures in Fig. 4.15. The field dependence follows the typical Poole-Frenkel-like dependence at all temperatures. The slope of the field dependence ($\beta = \delta \log \mu / \delta E^{1/2}$) is decreasing with decreasing temperature. The mobility values taken at a constant $5.2 \times 10^5 \text{ V cm}^{-1}$ electric field along the solid line is plotted versus $1000/T$ in Fig. 4.16, and a linear relationship is found. The activation energy of the mobility can be calculated using the phenomenological description of Gill's formula (Chapter 1.3, eq. 1.3). From the slope of the linear fit in Fig 4.16, the apparent activation energy ($\Delta - \beta_{\text{PF}} E^{1/2}$) of 120 meV is calculated. Alternatively, the temperature and electric field dependence of mobility can be analyzed within the framework of disorder formalism, which predicts a non-Arrhenius type activation of the mobility extrapolated to zero electric field as $\log \mu(E=0) \sim T^{-2}$. The $\log \mu(E=0)$ is plotted in the inset of Fig. 4.16 versus $1000/T^2$, and the observed dependence is approximated by a linear fit at higher temperatures. From the linear fit, $\sigma = 72 \text{ meV}$ is calculated. It is clearly seen that the last two points deviates significantly at lower temperatures. The electric field dependence was measured at longer time delays at all temperatures, therefore it is assumed that the field dependence of the mobility within the tail of the distribution is measured. The deviation from the temperature dependence of disorder formalism maybe attributed to non-dispersive to dispersive transition as introduced in Chapter 3.2. Alternatively, it may indicate that functional form of the density of localized states is not of a Gaussian-shape. The rather good fit using the Arrhenius-type

temperature dependence ($1/T$) may indicate that charge carrier mobility within an exponential density of states is probed as it was suggested previously based a multiple trapping model.

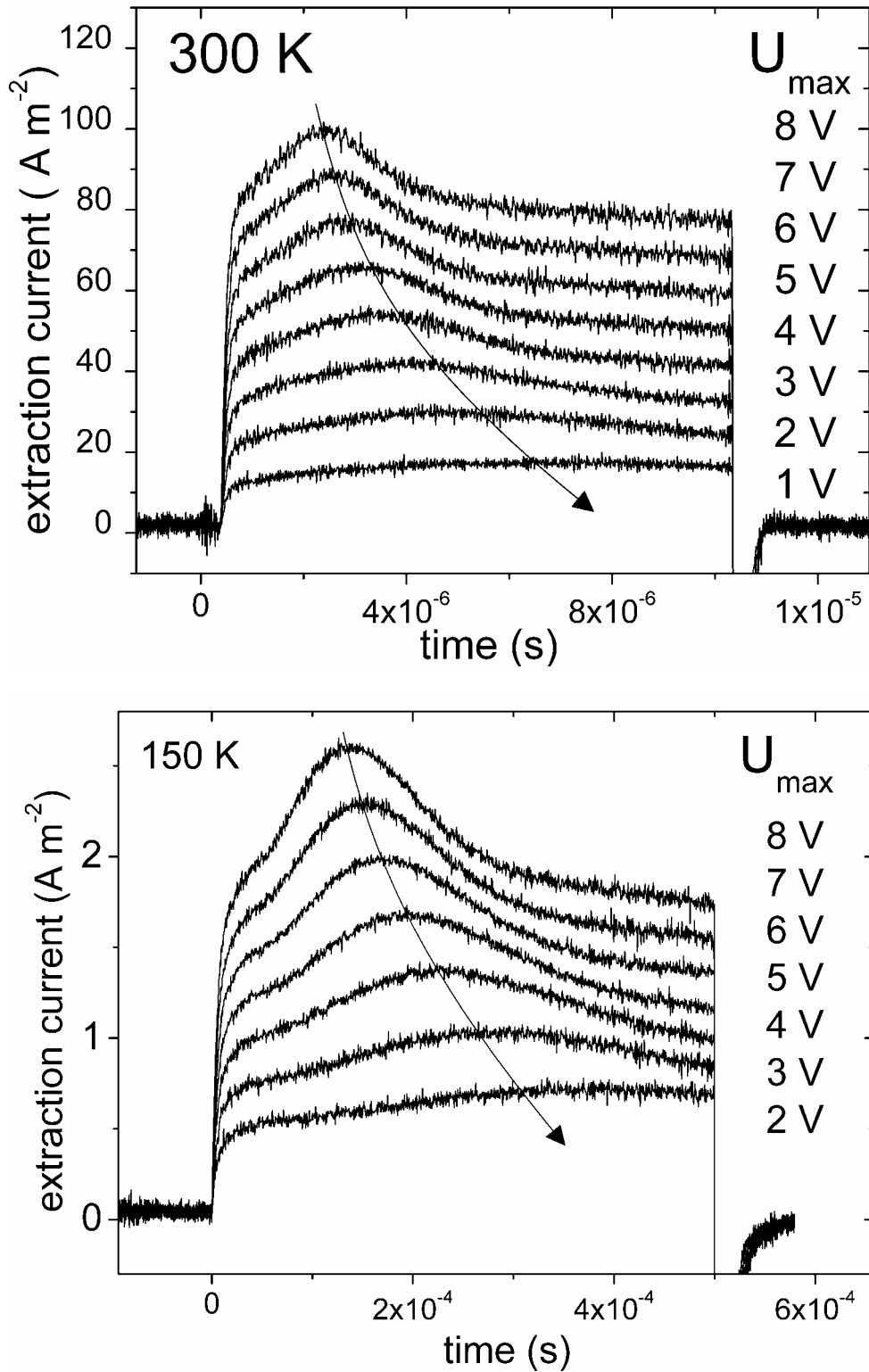


Figure 4.14: Photo-CELIV transients recorded at fixed delay time and light intensity, as a function of the maximum of the voltage pulse at 300 K, and 150 K.

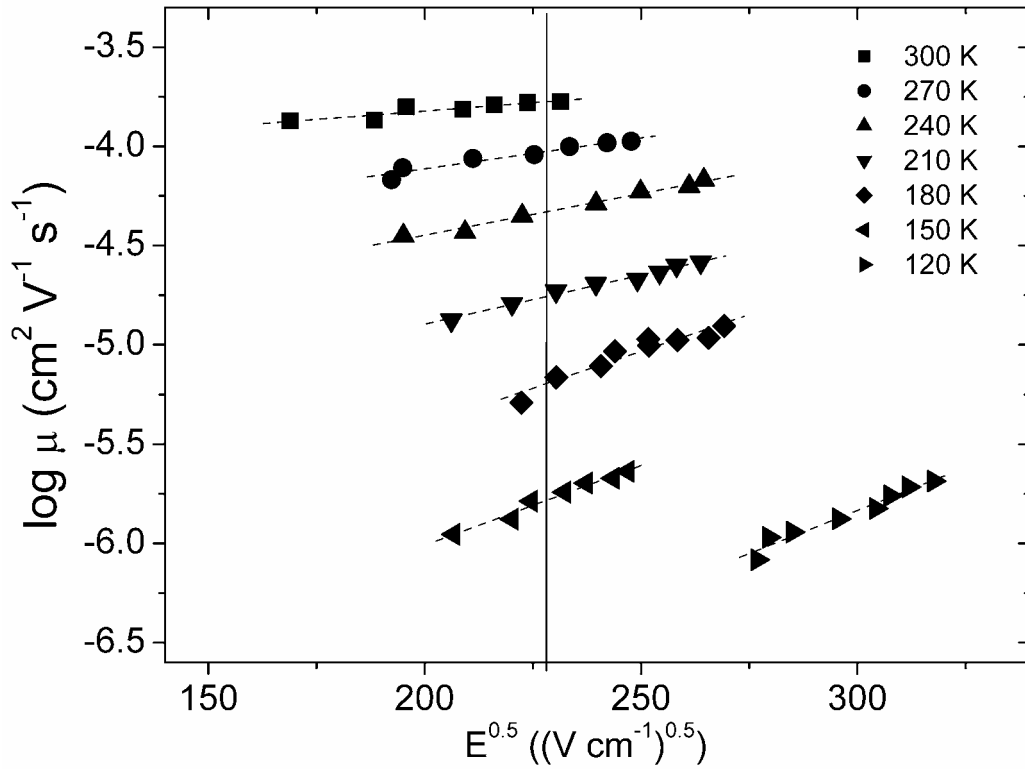


Figure 4.15: The logarithm mobility versus square root of the electric field at various temperatures.

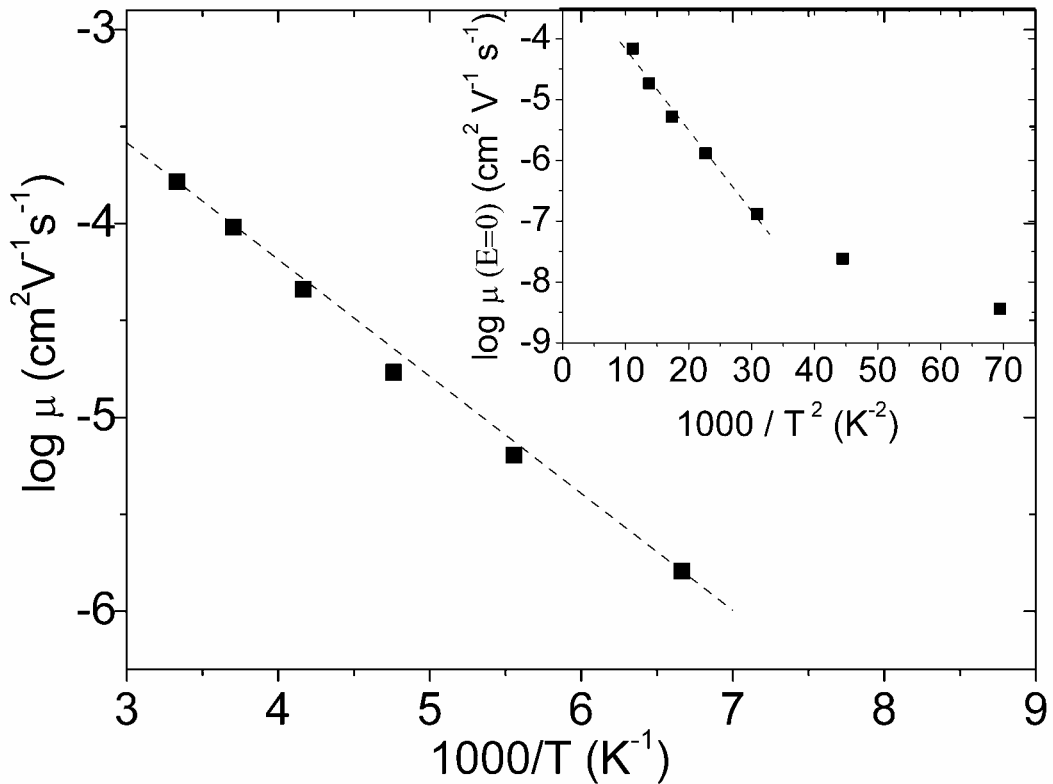


Figure 4.16: Arrhenius plot of the mobility at $E=5.2 \times 10^5 \text{ V cm}^{-1}$. Inset: Logarithm of zero field mobility versus inverse temperature squared.

Moreover, Fig. 4.15 clearly shows that the field dependence of the mobility is increasing with decreasing temperatures. It was shown that the electric field is not constant during the delay time dependent measurements in Fig. 4.7, which can have an influence on the slope of the $\mu \sim t^{-(1-\gamma)}$, especially at lower temperatures, where the field dependence of mobility is more pronounced.

4.4 Summary

In summary, the novel technique of photoinduced charge carrier extraction by linearly increasing voltage (photo-CELIV) has been introduced to determine the charge carrier mobility (μ) and the lifetime (τ) of the photogenerated charge carriers in bulk heterojunction solar cells. The photo-CELIV transients are non-dispersive at room temperature. The mobility and the bimolecular recombination rate are found to be time dependent, especially at lower temperatures. Such time dependent mobility and recombination may be related to energy relaxation of the charge carriers towards the lower lying, trap states of the distribution.

The simultaneous determination of mobility and lifetime of the charge carriers gives surprising results when compared to previous transient absorption (TA) studies. The photo-CELIV technique indicates that the majority of charge carriers is mobile and can be extracted in the photo-CELIV technique. This finding is not consistent with the results obtained by Monte Carlo simulation of the transient absorption data which assumed a 10^{17} cm^{-3} concentration of traps with at least two orders of lower mobility. The apparent discrepancy between the photo-CELIV experiments and the TA may be attributed to the fact that recombination of all the charge carriers including the immobile ones is probed in the transient absorption experiment. On the other hand, only charge carriers with reasonable mobility are extracted in the photo-CELIV experiment. From the end of the extraction pulse current it is estimated that the number of un-extracted, deeply trapped charge carriers is minimal at room temperature. This is not the case at lower temperatures, when significant portion of the charge carriers are not extracted within the applied frequency window.

A more complete understanding of the recombination dynamics could be obtained using the combination of a transient absorption and the photo-CELIV technique. In this proposed experiment, the change in the absorption of the sample

(ΔOD) is monitored as a function of delay time with and without charge carrier extraction as illustrated in Fig. 4.17. By the combination of these two techniques, the mobile carriers are probed by the photo-CELIV, meanwhile the optical signature of the un-extracted, immobile charge carrier can be detected by the TA experiment. Moreover, it would be also interesting to directly compare the concentration decay measured by the transient absorption experiment as well as from the delay time dependent photo-CELIV technique.

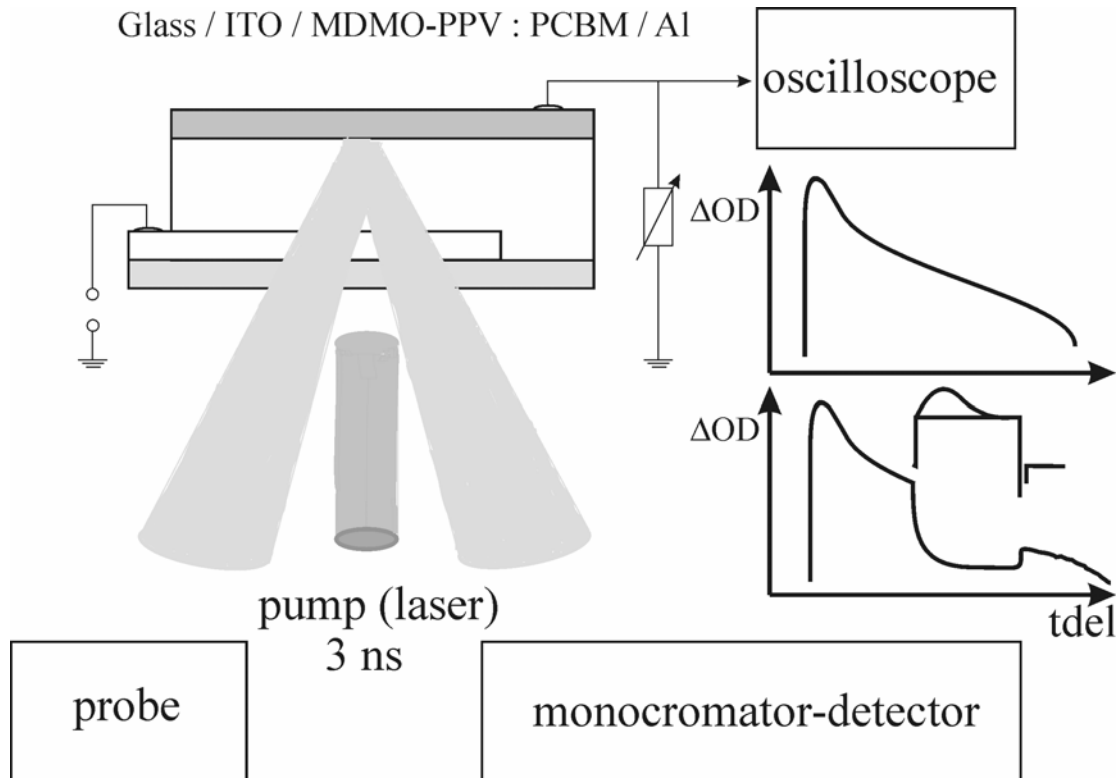


Fig. 4.17: The proposed experiment based on the combination of transient absorption and photo-CELIV. The change in the sample absorption due to photoexcitation by a sort laser pulse is monitored with our without charge extraction. From the extraction current, the mobility and can be determined. By comparing the ΔOD signals with and without extrcation, the amount of deeply trapped charge carriers can be calculated.

Chapter 5

5. Bulk Heterojunction Solar Cells

5.1 Regioregular MDMO-PPVs

The current density vs. voltage curve of bulk heterojunction solar cells based on the 1:4 weight ratio mixture of the 70:30 MDMO-PPV polymer with the fullerene acceptor PCBM is compared with RRa-MDMO-PPV in Fig. 5.1, and the parameters characterizing the photovoltaic performance are summarized in Table 5.1. The current density vs. voltage curve of the RRa-MDMO-PPV was taken from ref [32]. The active layer of both devices was app. 100 nm thick. Although the short-circuit current and the open-circuit voltage are quite similar for the two devices, the bulk heterojunction solar cell based on 70:30 MDMO-PPV exhibit higher power conversion efficiency of 2.65 % under simulated AM 1.5 conditions due to the very high (0.71) filling factor. A mathematical simulation of the current density vs. voltage curves shown in the inset of Fig. 5.1 has been performed based on the simple one-diode equivalent circuit model as illustrated in Fig. 5.2 expressed by the formula:

$$J = J_0 \left(\exp \left(\frac{V - JR_{RS}}{nk_B T} \right) - 1 \right) + \frac{V - JR_{RS}}{R_p} - J_{SC} \quad (5.1)$$

where J [$A\ cm^{-2}$] and V [V] are the current density and voltage values, J_0 [$A\ cm^{-2}$] is the reverse bias dark current, R_s [$\Omega\ cm^{-2}$] is the series resistance, R_p [$\Omega\ cm^{-2}$] is the parallel resistance and J_{sc} [$A\ cm^{-2}$] is the short-circuit current density under illumination.

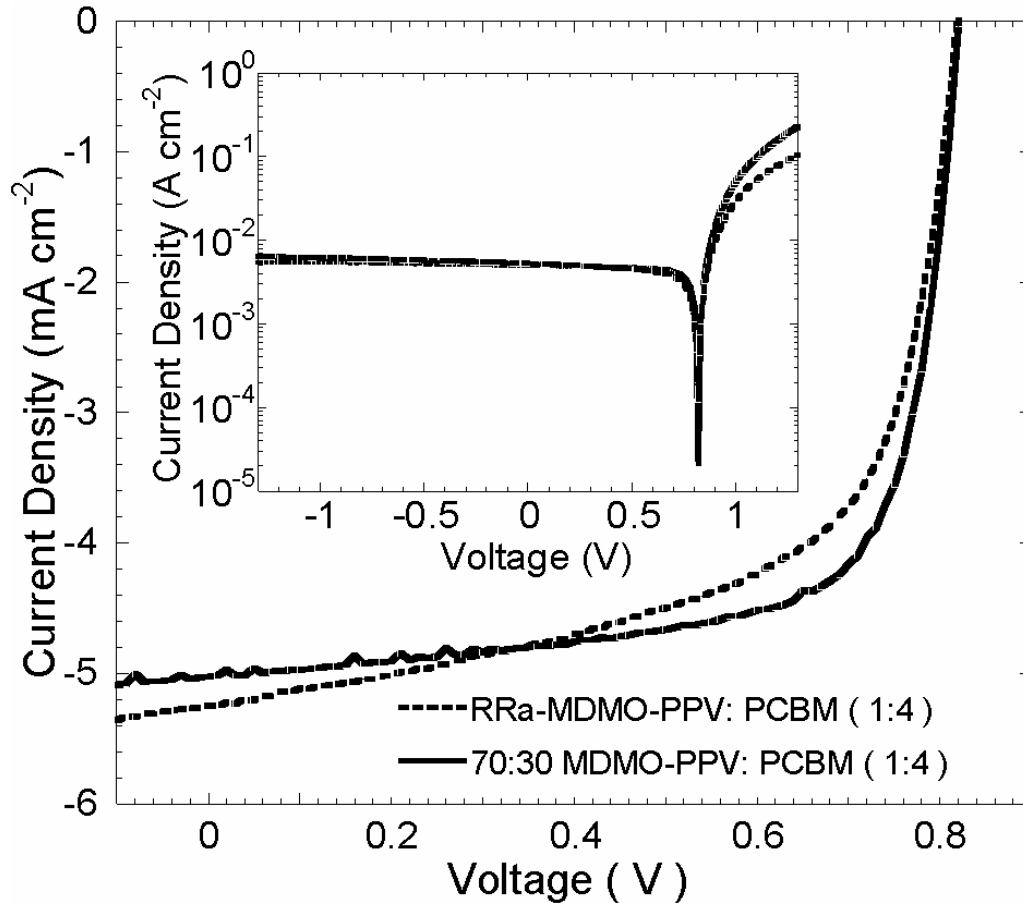


Figure 5.1: The current density versus voltage curves of bulk heterojunction solar cells based on the 70:30 MDMO-PPV (solid line) and RRa-MDMO-PPV (dashed line).

The equation has been numerically solved, and the parameters obtained by the best fit are summarized in Table 5.1.

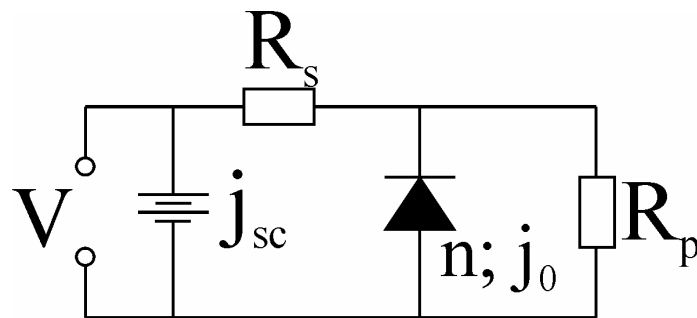


Figure 5.2: Equivalent one diode model of bulk heterojunction solar cells.

The factor of 2.3 lower series resistance together with the factor of 2.3 higher parallel resistance are responsible for the improved filling factor, and the improved photovoltaic performance of the 70:30 MDMO-PPV based device. The factor of 2.3 times higher parallel resistance most likely results from better film quality (*e.g.* less

shunts and shorts). The factor of 2.3 times lower series resistance, on the other hand, can be related to an improved mobility of the photogenerated charge carriers in the photoactive blend of 70:30 MDMO-PPV copolymer with PCBM. This result agrees well with the time of flight mobility data obtained for the pure 70:30 MDMO-PPV.

TABLE 5.1: Photovoltaic performance of the bulk heterojunction solar cells, and the parameters of eq. 5.1 obtained by numerical calculation.

	J_{sc}	V_{oc}	FF	$\eta_{AM\ 1.5}$	J_0	R_s	R_p	n
	$mA\ cm^{-2}$	V		% ^b	$mA\ cm^{-2}$	$\Omega\ cm^{-2}$	$\Omega\ cm^{-2}$	
1	5.0	0.8	0.71	2.65	6×10^{-7}	1.3	2150	1.9
2	5.25	0.82	0.61	2.5	6×10^{-7}	3	950	2

*Sample 1 and 2 stands for 70:30 MDMO-PPV and RRa-MDMO-PPV, respectively.

^b Calculated using eq. 2.1, $m=0.751$.

5.2 Thickness Dependence Parameters of Bulk Heterojunction Solar Cells

It is expected that the short circuit current of bulk heterojunction solar cells rises with increasing active layer thickness due to the increased absorption. The thickness dependence of the maximum short circuit current of bulk heterojunction solar cells has been obtained by optical modeling taking into account interference effects due to multiple reflections between the subsequent layers.⁹⁸ According to $d \geq l_d = \mu \times \tau \times E$, on the other hand, electrical losses due to recombination are expected when the thickness of the active layer exceeds the drift distance of the charge carriers, where $E = V_{oc}/d$ is the electric field. Based on these arguments, the thickness dependence of the short circuit current of bulk heterojunction solar cells should give an estimate of the drift distance of the charge carriers, which then can be compared to the $\mu\tau$ product determined by the photo-CELIV technique.

As it is emphasized, the performance of bulk heterojunction solar cells is morphology dependent; therefore the proposed comparative study can only be meaningful if the morphology of the active layer is unchanged by changing the thickness of the active layer. The same solution of MDMO-PPV:PCBM (1:4) by weight (chloroform, 0.5 mg polymer/ml solution) was used to prepare all the films, and the spin speed during the spin coating was varied between 1000 rpm and 6000 rpm. It is expected that this procedure is more suitable for the proposed thickness dependent experiment as compared to *e.g.* varying the total concentration, or the solvent.

The thickness of the active layer versus the spin speed is shown in Fig. 5.3. The thickness is around 125 nm at 6000 rpm, and increases nonlinearly to 280 nm at 1000 rpm. The films prepared at lower spin speeds were somewhat less uniform, therefore 8 devices have been measured, and the results averaged. The average power conversion efficiency of the bulk heterojunction solar cells using 125 nm active layer is around 2.5 % (Fig. 5.3), which drops to app. 1.7 % if the thickness is 280 nm. The power conversion efficiency was calculated according to eq. 2.1, and the mismatch factor was $m=0.95$.

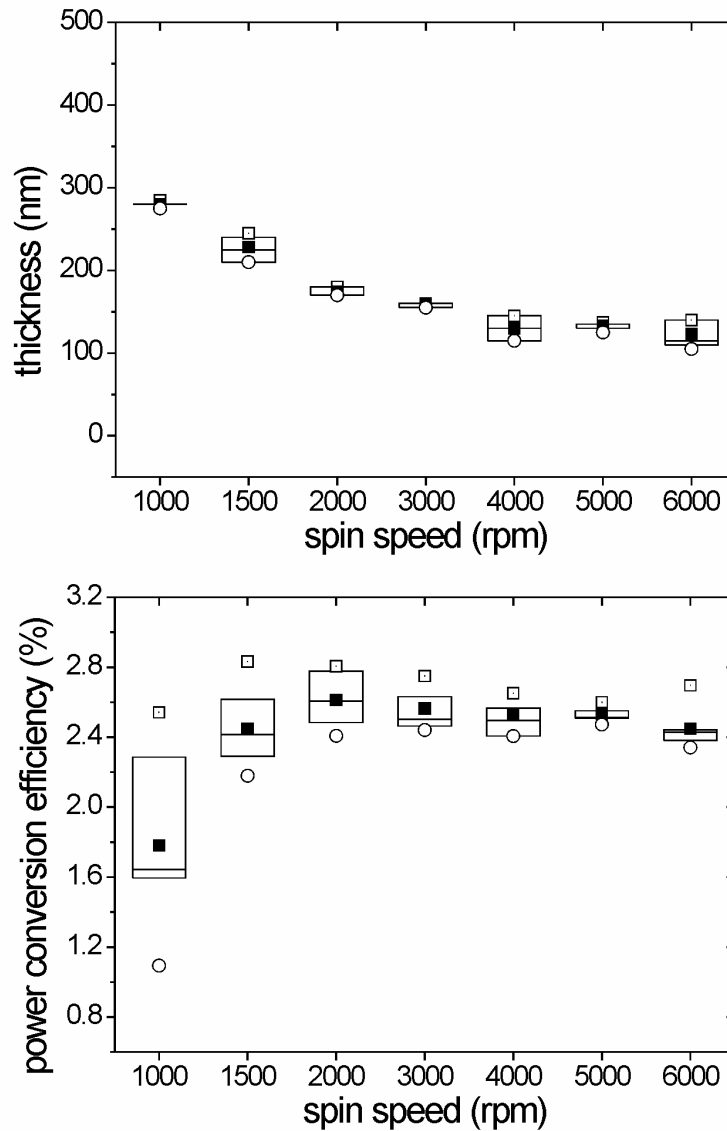


Figure 5.3: The average thickness and the power conversion efficiency of bulk heterojunction solar cells versus the spin speed during spin coating for MDMO-PPV:PCBM bulk heterojunction solar cells.

The parameters I_{sc} , V_{oc} , FF, and the injection current density at +2 V are shown in Fig. 5.4. The average short circuit current density increases slightly as the thickness of the active layer is increased ($\sim 5.2 \text{ mA cm}^{-2}$ at 125 nm). It is maximal at 225 nm ($\sim 6 \text{ mA cm}^{-2}$), and drops when it is 280 nm. The measured V_{oc} is constant $\sim 800 \text{ mV}$ for all active thickness. The filling factor, on the other hand, drops constantly from 0.6 to 0.4 as the thickness of the active layer is increased, which correspond nicely to the reduced injection current density at +2V. From this data it is evident that the drop in

the power conversion efficiency at 280 nm is attributed mainly to the reduced filling factor, which decreases stronger than the slightly increased short circuit current.

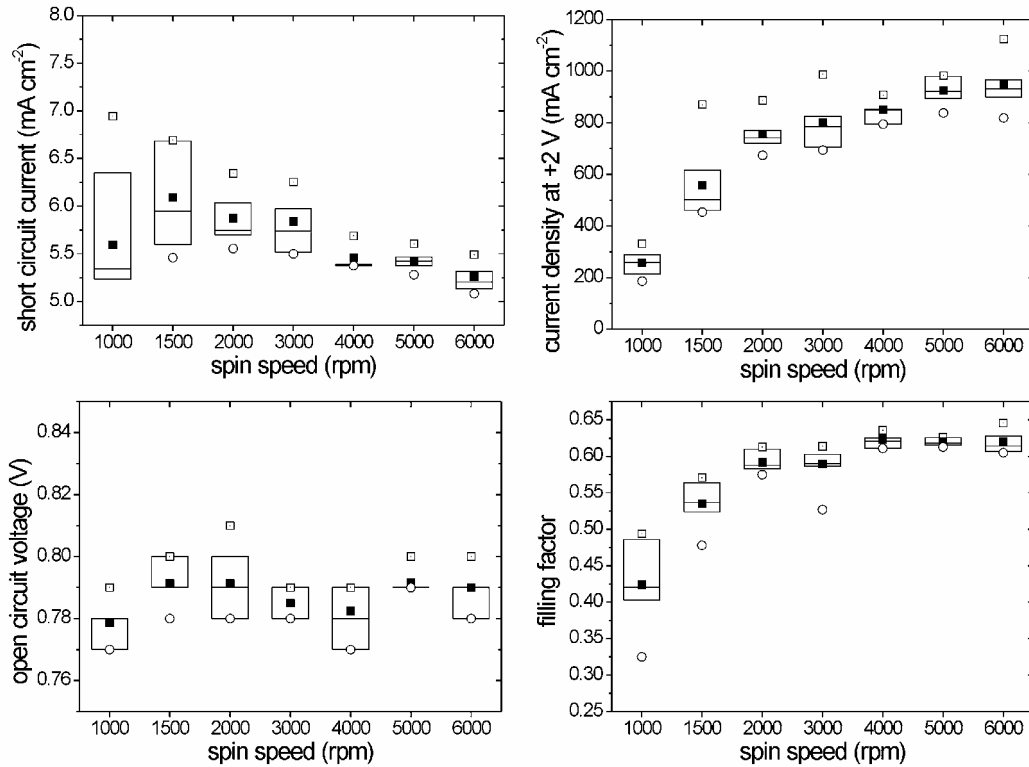


Figure 5.4: The average short circuit current density, injection current density at +2V, open circuit voltage and filling factor versus the spin speed during spin coating.

The current density versus voltage curves recorded for the bulk heterojunction solar cells with various thicknesses are shown in a semilog representation in Fig.5.5. The thinner devices exhibit rectification ratios of approximately 3-4 orders of magnitude in the dark and 2 orders of magnitude under illumination. The rectification ratio is reduced by 1 order of magnitude due to smaller injection current as the thickness of the active layer is increased. The 4th quadrant of the current density versus voltage curves are shown in Fig 5.6. The reduction of the filling factor with increasing film thickness is clearly observed.

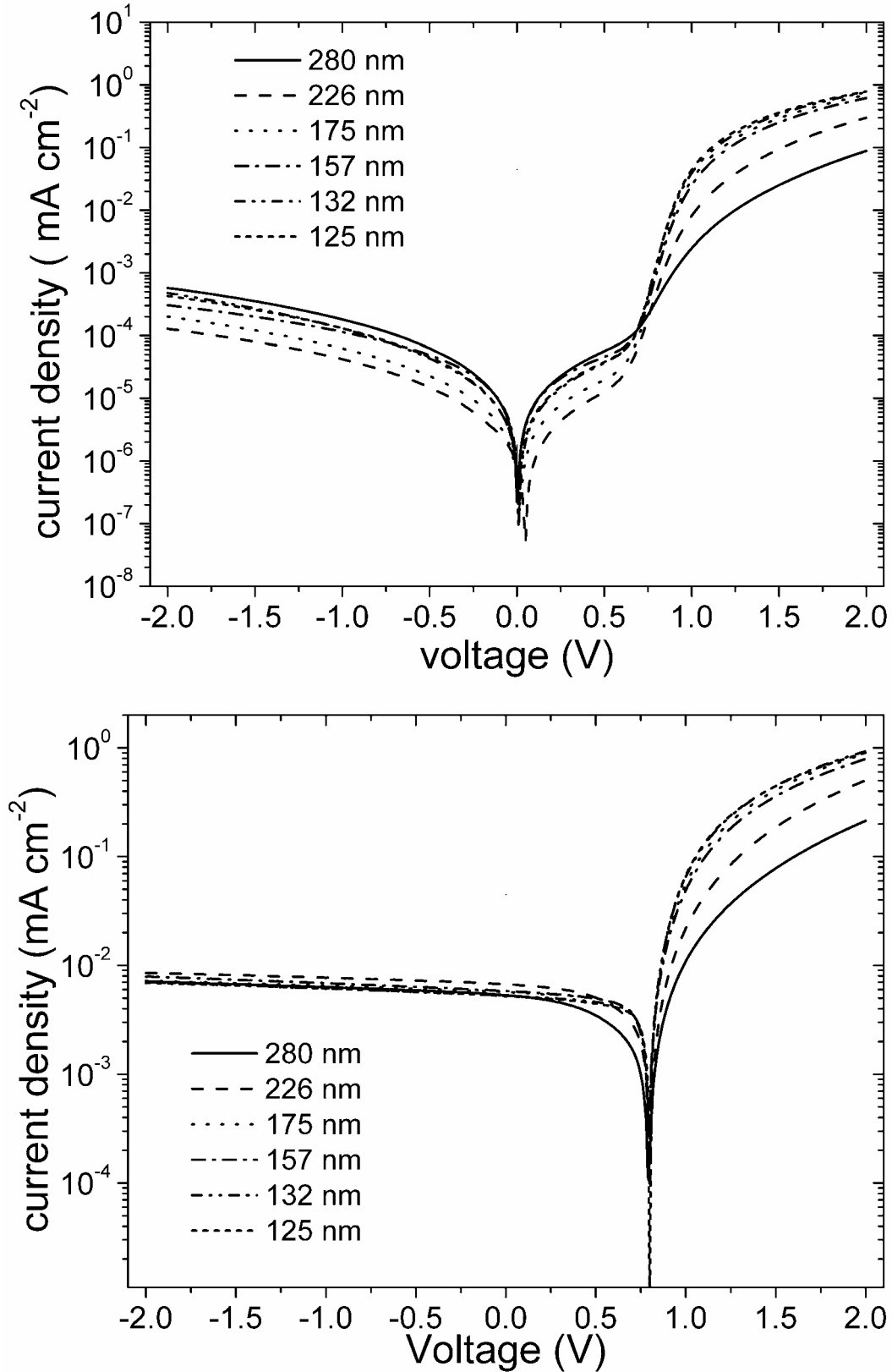


Figure 5.5: The current density versus voltage curves of bulk heterojunction solar cells with varying active layer thickness in the dark and under illumination.

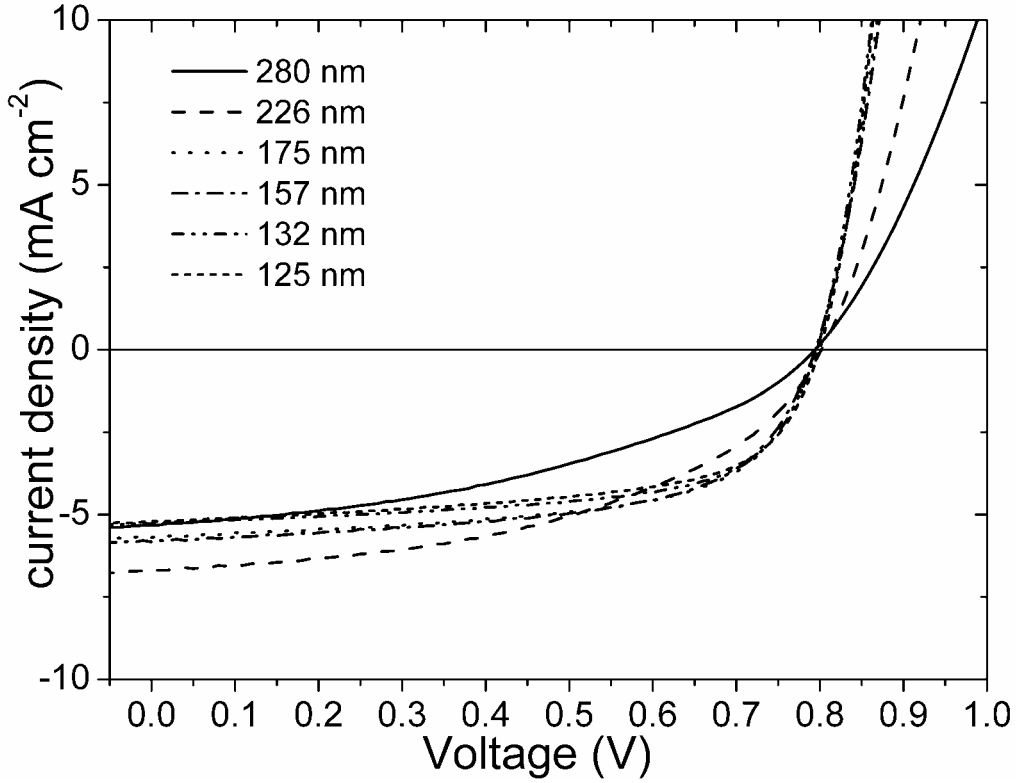


Figure 5.6: The current density versus voltage curves of bulk heterojunction solar cells with varying active layer thickness under illumination.

The current density versus voltage curves under illumination are analyzed by a modified version of a simple one diode model shown in Fig. 5.2. This modified model has been introduced by Schilinsky et al. to explain the illumination intensity dependent J-V curves of bulk heterojunction solar cells based on P3HT:PCBM blends.⁹⁹ The model takes into account the applied voltage (V_{ext}) dependent reduction of the charge collection of the photogenerated charge carriers at the electrodes. As the external voltage is increased towards flat band conditions, the electric field in the device is reduced. Accordingly, only charge carriers created within the reduced drift distance $l_d = \mu \times \tau \times (V_{oc} - V_{ext}) / d$ will contribute to the short circuit photocurrent. In other words, the photocurrent (j_{sc}) in eq. 5.1 is not constant, but depends on the applied voltage (V_{ext}) according to:

$$j_{light}(V_{ext}) = \begin{cases} -|I_{sc}| & \text{if } \mu\tau \times (-V_{ext} + V_{oc}) / d > d \\ |I_{sc}| & \text{if } \mu\tau \times (V_{ext} - V_{oc}) / d > d \\ |I_{sc}| \times \mu\tau \times (-V_{ext} + V_{oc}) / L^2 & \text{else} \end{cases} \quad (5.2)$$

Important predictions of eq. 5.2 are that the sign of the photocurrent changes when $V_{ext} > V_{oc}$, and that the short circuit current is reduced when V_{ext} is raised towards V_{oc} . According to eq. 5.2, the high filling factor of the devices with 125 nm thickness indicates that only a small electric field $(V_{oc} - V_{ext})/d$ is sufficient to collect most of the photogenerated charge carriers from the whole device (the photocurrent reaches $\sim 5 \text{ mA cm}^{-2}$ at $\sim 0.6 \text{ V}$, corresponding to $\sim 0.2 \text{ V}/125 \text{ nm}$ electric field). On the contrary, the photocurrent density is steadily increasing till $\sim 0 \text{ V}$ (corresponding to a field of $\sim 0.8 \text{ V} / 226 \text{ nm}$) when the device thickness is increased to 226 nm.

The charge carrier mobility from Fig. 4.4 is $\mu = 2 \times 10^{-4} \text{ cm}^2 \text{V}^{-1} \text{s}^{-1}$, and the lifetime from Fig. 4.11 is $\tau_B \sim 3 \text{ } \mu\text{s}$, therefore $\mu\tau$ is:

$$\mu \times \tau = 2 \times 10^{-4} \text{ cm}^2 \text{V}^{-1} \text{s}^{-1} \times 3 \times 10^{-6} \text{ s} = 6 \times 10^{-10} \text{ cm}^2 \text{V}^{-1}$$

using the above $\mu\tau$ value, the maximum thickness of the active layer ($d < l_d$) can be calculated as:

$$d = \sqrt{\mu \times \tau \times V_{oc}} = \sqrt{6 \times 10^{-10} \text{ cm}^2 \text{V}^{-1} \times 0.8 \text{ V}} = 220 \text{ nm}$$

According to this result, the short circuit current density of bulk heterojunction solar cells should not drop significantly with thickness $< 220 \text{ nm}$, or in other words, bimolecular recombination of the charge carriers should not limit the device at short circuit condition, which is in accordance to the experimental observations in Fig. 5.4.

Furthermore, using $\mu\tau$ value, the maximum applied external voltage (V_{ext}) corresponding to the minimum electric field $((V_{oc} - V_{ext})/d)$ which is necessary to extract all the carriers from the device ($l_d = 1$) can be estimated at various device thicknesses:

$$l_d = \mu \times \tau \frac{(V_{oc} - V_{ext})}{d} = 6 \times 10^{-10} \text{ cm}^2 \text{V}^{-1} \times \frac{(0.8 \text{ V} - V_{ext})}{d}$$

using $d = l_d$:

$$V_{ext} = 0.8 \text{ V} - \frac{d^2}{\mu \times \tau}$$

E.g. if the active layer thickness is $d = 125 \text{ nm}$,

$$V_{ext} = 0.8V - \frac{(125 \times 10^{-7} \text{ cm})^2}{6 \times 10^{-10} \text{ cm}^2 \text{ V}^{-1}} = 0.55V$$

or if the active layer thickness is $d=226$ nm,

$$V_{ext} = 0.8V - \frac{(280 \times 10^{-7} \text{ cm})^2}{6 \times 10^{-10} \text{ cm}^2 \text{ V}^{-1}} = -0.05V$$

These calculations predict high filling factor of the 125 nm thick device, because only 0.25 V/ 125 nm electric field is sufficient to extract most of the carriers from the device. On the other hand, lower filling factor is expected in the 226 nm device, because maximum extraction of the charge carriers occurs only in the third quadrant (-0.05 V) of the current density versus voltage curves. The above calculations neglect several effects, such as trapping of the charge carriers, the field dependence of the mobility or electrical losses due to non-selective contacts. Moreover, it is assumed that $\mu\tau$ is constant with varying active layer thickness, which is not necessarily true due possible changes in the active layer morphology. To delineate the possible effect of the above listed shortcomings, a simulation of the J-V curves according to eq. 5.2 is required. Nevertheless, the determined $\mu\tau$ qualitatively fit the experimental results. This implies that i) the above electric field driven charge carrier collection at the electrodes is justified ii) the $\mu\tau$ product determined by the photo-CELIV measurements can be used to model the actual device operation iii) the main limitation on the device performance with increasing thickness is the decreasing filling factor, attributed to the reduced electric field. Smaller electric field causes shorter drift distances therefore reduced charge collection in thicker devices.

The above conclusions are also supported by observed light intensity dependence of the short circuit photocurrent density.³¹ Scaling factor close to 1 are typically observed, which indicates that the short circuit current is not limited by second-order recombination processes, such as bimolecular recombination.

5.3 Polythiophene – anthraquinone “Double-Cable” Copolymers

Photodiodes have been prepared based on the polythiophene-anthraquinone copolymers. First, LiF / Aluminum electrode was used as the top contact. These devices showed a few $\mu\text{A cm}^{-2}$ short circuit photocurrent, yet the open circuit voltage was very low (200 mV). Also, these devices showed no rectification behavior, which can be attributed to the low injection current from the LiF / Aluminum contact at even large applied forward bias. The LiF / Aluminum contact is typically used in bulk heterojunction solar cells containing C60 derivatives as the electron acceptor. For the “double-cable” polymers containing anthraquinone, the LiF/Al contact may not be suitable. Therefore, a series of devices were prepared using Calcium as the top electrode.

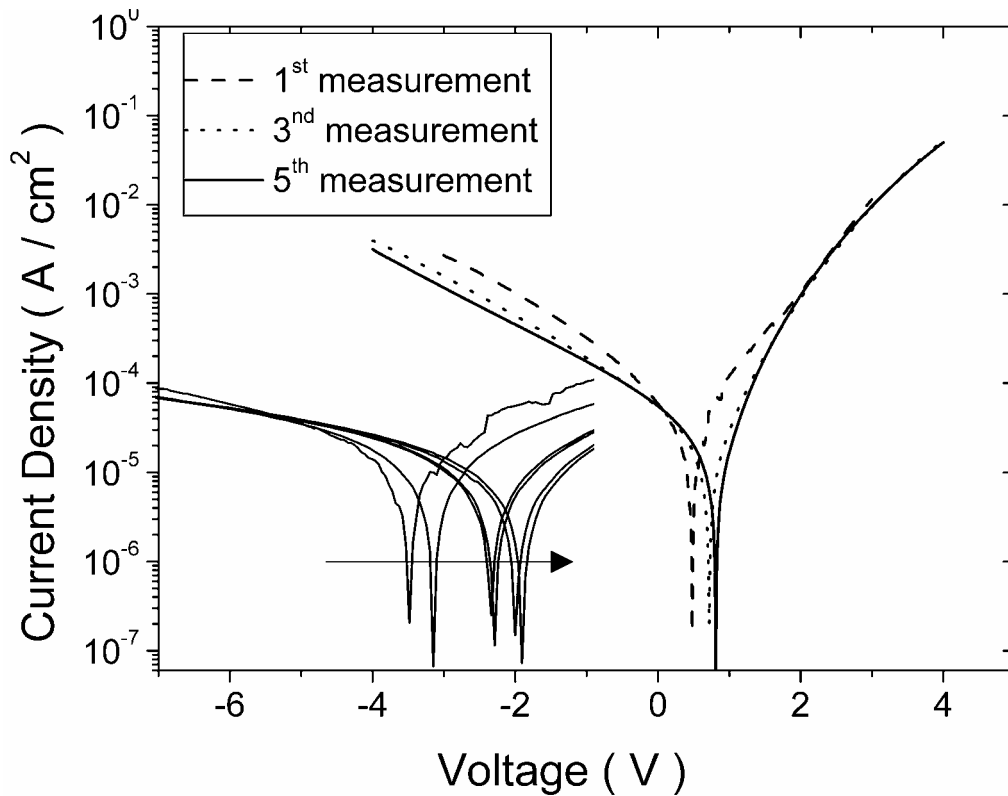


Figure 5.7: The current density versus the voltage curves of photovoltaic devices based on a polythiophene-anthraquinone double cable (PTA 75) upon subsequent measurements.

Fig. 5.7 shows the recorded current density versus voltage curves under 80 mW cm^{-2} white light illumination. These devices show an improved rectification measured at -4 V and $+4 \text{ V}$ due to better injection at positive voltages. Interestingly,

the open circuit voltage is increased between subsequent measurement circles, and saturated at around 880 mV. This may be related to increased shunt resistance of the device.

Although the short circuit current of the devices is still rather low, its magnitude enabled to spectrally resolve it (IPCE). The measured IPCE (Fig. 5.8) follows nicely the absorption of the PTA 75 indicating that the previously observed photoinduced charge transfer (LESR and FT-PIA) is the main charge generation mechanism in these devices.

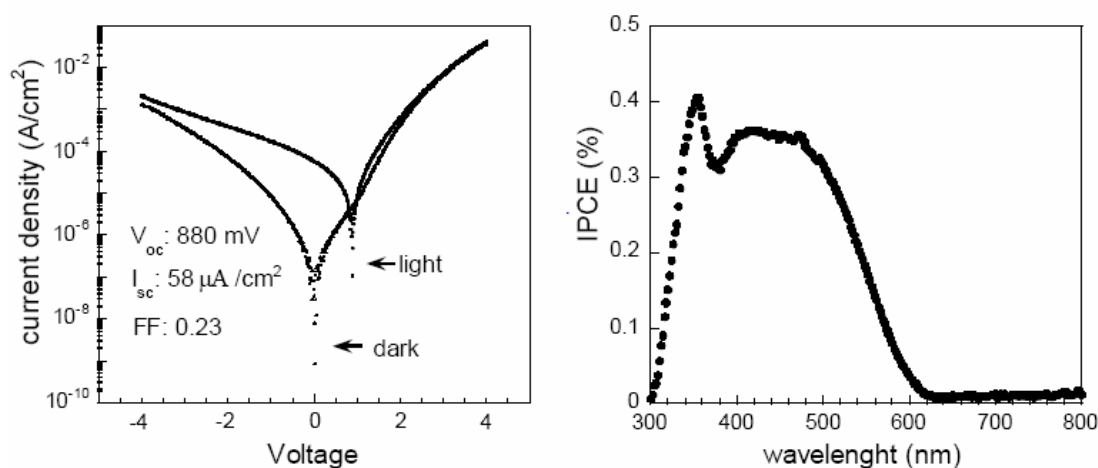


Figure 5.8: The current density versus the voltage curve (left) and the IPCE (right) of the photovoltaic devices based on the polythiophene-anthraquinone double cable (PTA 75).

5.4 Dithienothiophene and Dithienothiophene-S,S-dioxide Copolymers

The absorption coefficient of the dithienothiophene copolymers shown in Fig. 5.9 has been determined by the procedure described in ref. [98]. Generally, the absorption of the films is red shifted for all polymers as compared to the absorption in dilute solutions. The absorption is even more red shifted of the copolymers with S,S-dioxide groups at the center polythiophene ring of the dithienothiophene moiety (Pox polymers). This is due to the increased tendency to aggregate and stack in the solid films, which is also supported by the AFM images shown in Fig. 5.10. The AFM images indicate a rather smooth, amorphous morphology of the P1 (and also P2, not shown), and a more structured surface morphology can be observed for the P1ox (and P2ox, not shown).

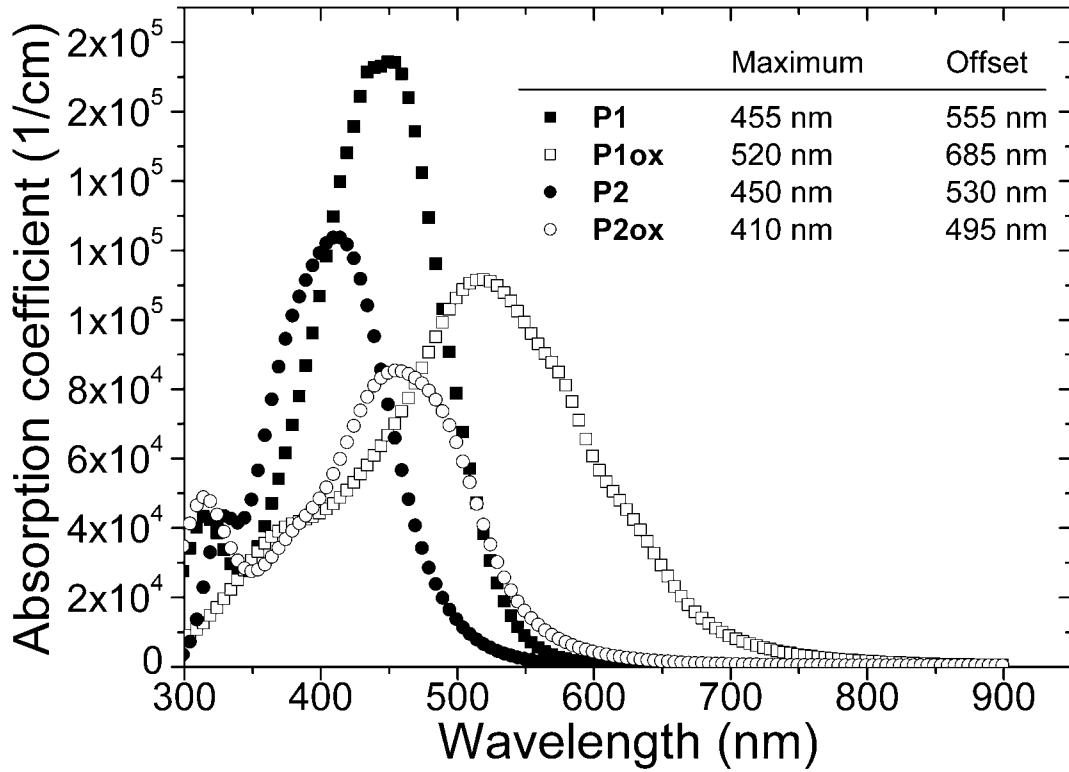


Figure 5.9: The absorption coefficient of the dithienothiophene copolymers.

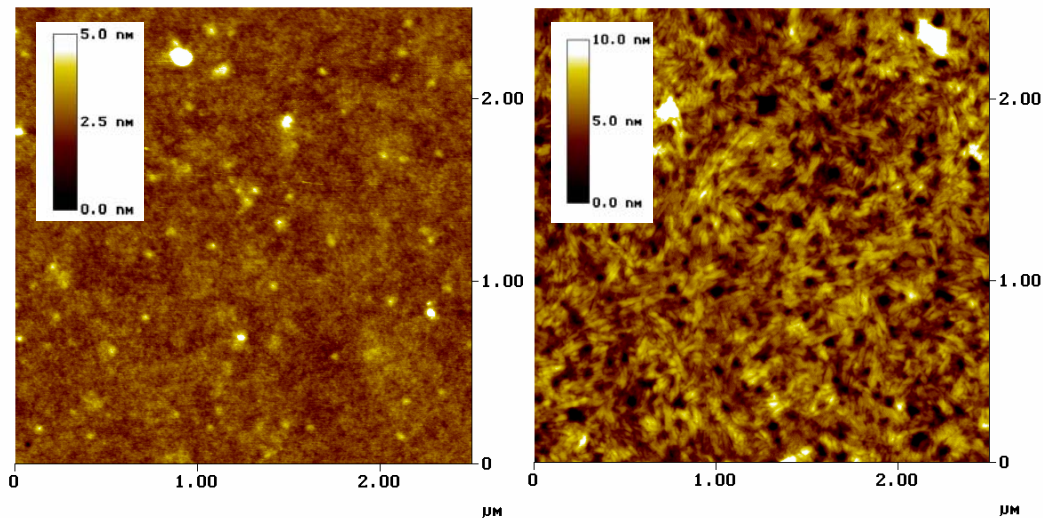


Figure 5.10: AFM images of spin coated films of P1 (left) and P1ox (right).

Bulk heterojunction solar cells have been prepared by mixing the polymers with PCBM, and the current density versus voltage curves of the devices under illumination are shown in Fig 5.11. The device parameters are summarized in the inset. The short circuit current density of the P1 polymer is quite remarkable considering the rather large band gap. Moreover, the V_{oc} and the filling factor are also acceptable. The power conversion efficiency of the P2 cells is only half of that of P1, which is mainly

due to the lower short circuit current of these devices. This is in accordance with the increased band gap, and blue shifted absorption of this polymer. The performance of the P1ox and P2ox polymers is significantly worse. Although their spectral sensitivity is extended to almost 100 nm to the red part of the spectra (see Fig. 5.12), the short circuit current is only 20 % of the P1 polymer, which is probably due to the large scale phase separation, therefore inefficient charge generation in the blend of these polymers. Alternatively, the reduced photocurrent may be due to the lower mobility of the Pox polymers, therefore inefficient charge transport and collection.

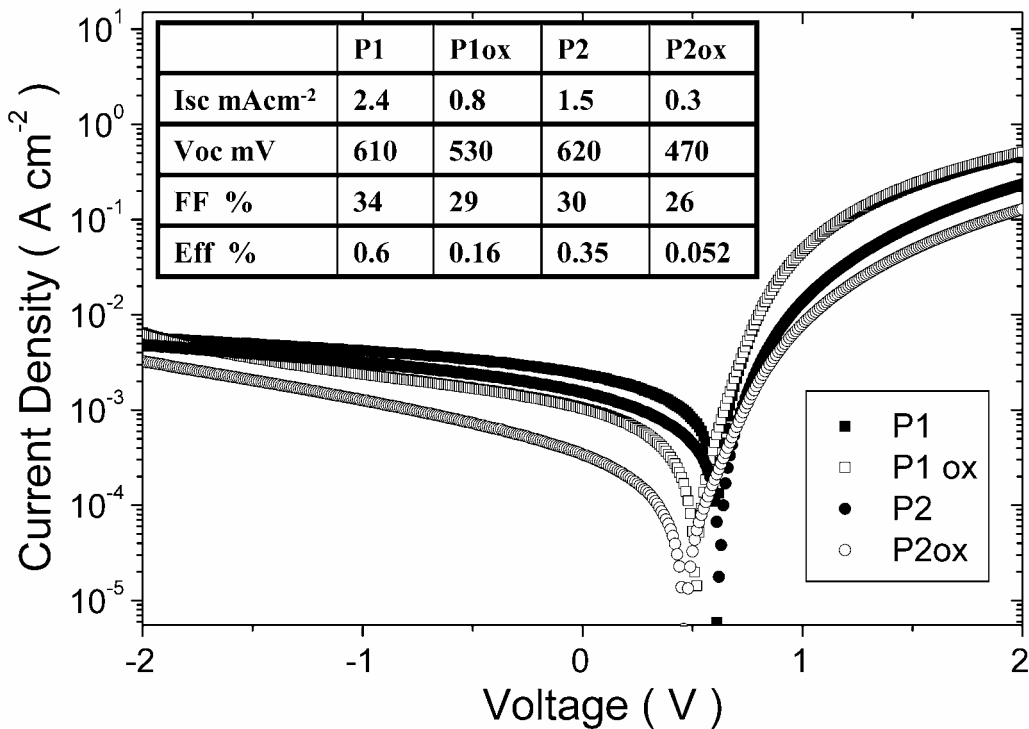


Figure 5.11: The current density versus voltage curves of bulk heterojunction solar cells based on the dithienothiophene copolymers and PCBM.

The charge transport properties of the dithienothiophene copolymers have been investigated using the field effect transistor structure. The polymer layers were spin coated on top of a p-type Si substrate covered with 100 nm thermally grown SiO₂ oxide dielectric. On top of the polymer films, Au was evaporated through a shadow mask to form the top contacts of the field effect transistor. Approximately 20 devices have been prepared on each substrate with varying channel length between 30 μm and 200 μm . The obtained output characteristics of a transistor based on P1 polymer with 30 μm channel width is shown on Fig. 5.13.

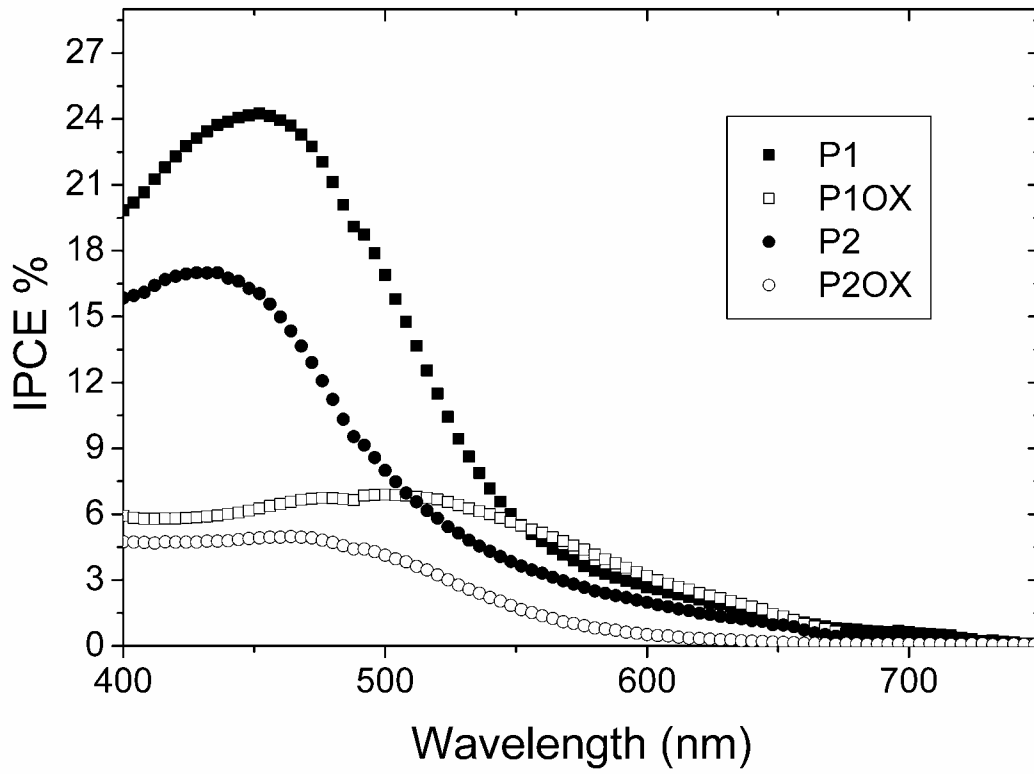


Figure 5.12: IPCE curves measured for bulk heterojunction solar cells based on the dithienothiophene copolymers and PCBM.

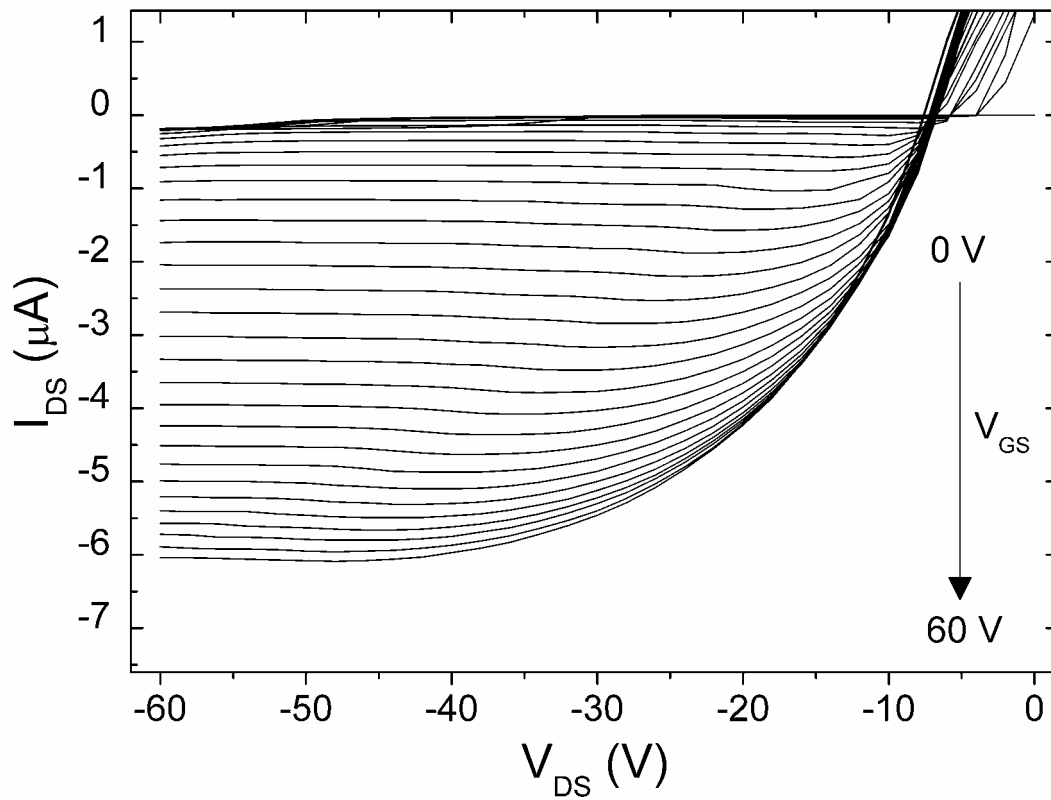


Figure 5.13: Output characteristics of an FET based on P1.

The field effect mobility was calculated from the transfer characteristics shown in Fig. 5.14. The drain-source current was recorded at fixed 60 V drain source voltage as the function of the gate-source voltage. The current in the saturation regime can be analyzed according to:

$$I_{DS} = \frac{W}{2L} \mu C_i (V_{GS} - V_t)^2$$

and from the slope of the $(I_{DS})^{1/2}$ versus V_{GS} , the mobility can be calculated:

$$\sqrt{I_{DS}} = -\sqrt{\frac{W}{2L} \mu C_i} \times V_t + \sqrt{\frac{W}{2L} \mu C_i} \times V_{GS}$$

after rearrangement:

$$\mu = \frac{(\partial(I_{DS})^{0.5} / \partial V_{GS})^2 2L}{WC_i} = 3 \times 10^{-5} \text{ cm}^2 \text{ V}^{-1} \text{ s}^{-1}$$

This value is comparable to other amorphous polymer FETs, but several orders of magnitude lower than in regioregular P3HT, in which stacking of the conjugated chains was shown to improve the charge carrier mobility.

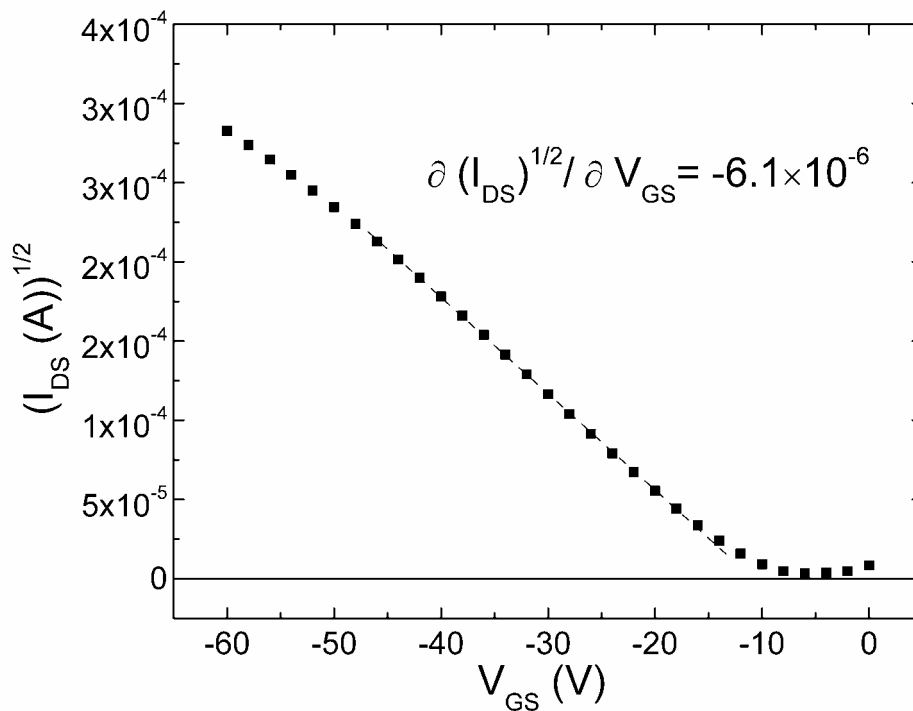


Figure 5.14: Transfer characteristics of an FET based on P1 at fixed 60 V drain-source voltage.

No gate effect was observed in the transistor based on P2, P1ox and P2ox, which may be related to the very low charge carrier mobility in these materials. On the other hand, the poor film forming properties of these polymers may hinder the determination of their intrinsic properties in FET structure.

5.5 PProDot(Hx)₂

The UV-vis absorption spectra recorded in dilute chlorobenzene solution and of the films are displayed in Fig 5.15. Both the absorption and the PL in the films are red shifted, and more structured indicating ordering of the conjugated chains. The very strong PL of the films is efficiently quenched in the mixtures with PCBM, and the typical optical signatures of polarons are detected in photoinduced absorption experiment (not shown). The PL quenching and PIA is a strong indication of photoinduced charge transfer.

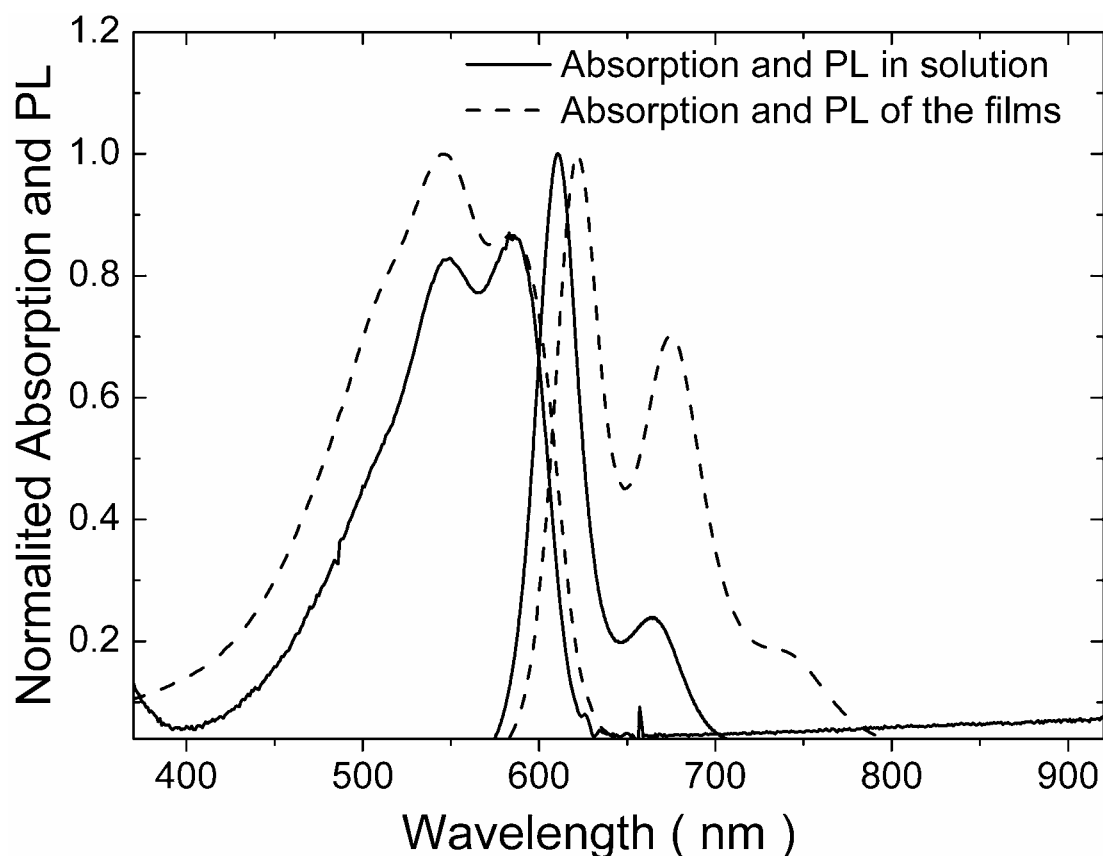


Figure 5.15: UV-vis absorption and PL of PProDot(Hx)₂ polymer in dilute chlorobenzene solution (solid lines) and of the films (dashed lines).

Fig. 5.16 shows the current density versus voltage curves measured in the dark (solid lines) and under illumination (dashed lines) for a bulk heterojunction solar cell based on the 1:2 mixture of PProDot(Hx)₂ and PCBM sandwiched between ITO/PEDOT-PSS and LiF / Aluminum electrodes. The diodes exhibit 3 orders of rectification, which is among the best for bulk heterojunction solar cells. The open circuit voltage of the devices is very low, which cannot be simply explained by the band structure of the devices (HOMO of the polymer is 5.0 eV, LUMO of PCBM 4.3 eV). It indicates that recombination in these materials leading to a voltage drop may limit the device performance.

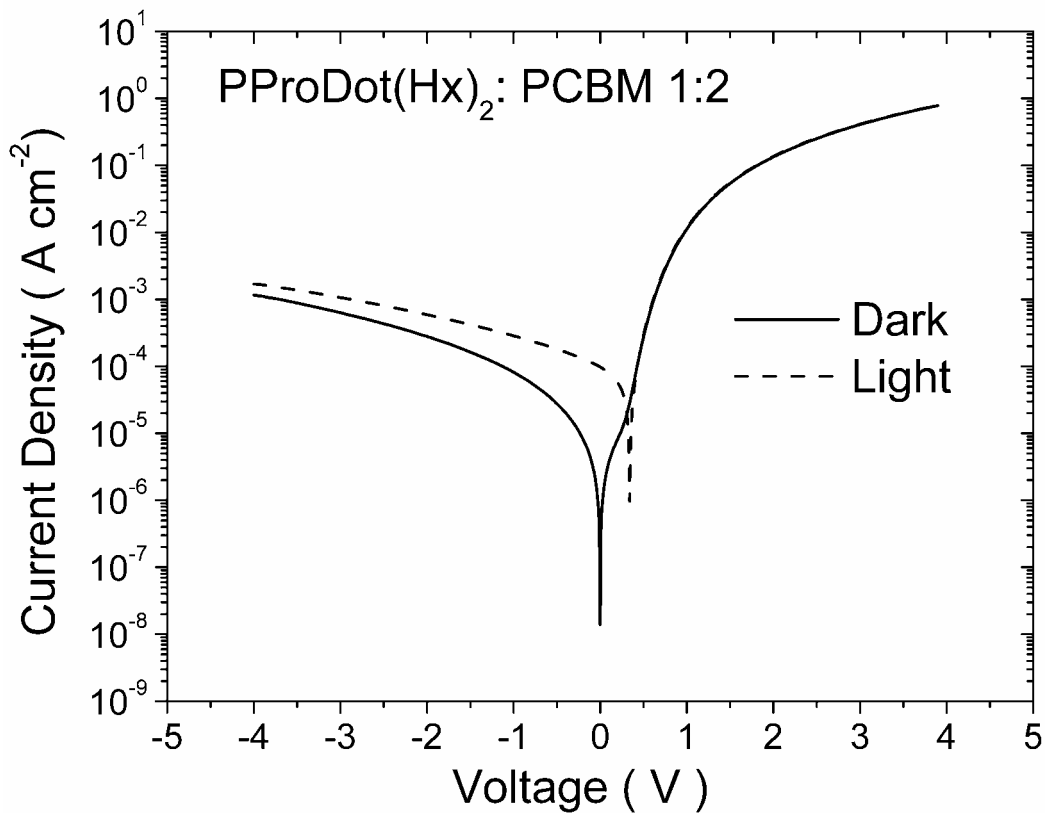


Figure 5.16: Current density versus voltage curves of bulk heterojunction solar cells based on PProDot(Hx)₂ : PCBM films.

Chapter 6

6. Summary and Outlook

Two independent methods for charge carrier mobility determination, namely; a.) time of flight; b.) charge carrier extraction by linearly increasing voltage (CELIV) have been used to study the temperature and electric field dependence of mobility in conjugated polymers. In the ToF method, a sheet of excess carriers generated by a laser flash drifts across the sample. The comparative study between regioregular and regiorandom MDMO-PPV showed that the morphology of the polymer films plays a crucial role in determining the charge transport properties. The improved charge transport properties of the regioregular MDMO-PPV has been utilized in fabrication of bulk heterojunction solar cells with improved efficiency and a very high 0.7 filling factor.

The CELIV method probes the motion of charges generated by homogeneous doping throughout the bulk. By applying both ToF and CELIV techniques in the same poly(3-hexylthiophene) with or without doping, it has been shown that these techniques are mutually consistent. A fundamental issue is the observation of the negative electric field dependence of mobility at moderate electric fields by both experimental techniques. The comparison of these two principally different techniques confirmed that the negative electric field dependence of mobility is an intrinsic feature of the investigated materials. Large degree of positional disorder equivalent to the large spread of intersite coupling matrix elements are proposed to be responsible for this negative electric field dependence of mobility as suggested by the disorder model.

The novel technique of photoinduced charge carrier extraction by linearly increasing voltage (photo-CELIV) has been introduced to simultaneously determine

the charge carrier mobility (μ) and lifetime (τ) of the charge carriers in bulk heterojunction solar cells. The measured $\mu\tau$ values can be used to describe the recorded current density –voltage curves of bulk heterojunction solar cells with varying active layer thickness. Although it is estimated that recombination of the charge carrier should not limit the device operation at short circuit conditions if the active layer thickness < 250 nm, the power conversion efficiency is reduced because of the decreasing filling factor of the thicker devices. The optimum performance is found using active layer thickness not exceeding 200 nm.

Finally, the simultaneous determination of the charge carrier mobility and lifetime of the charge carriers by the photo-CELIV technique opens up new possibilities for studying time-dependent (dispersive) relaxation processes of charge carriers in non-crystalline solids. Such relaxation processes have been studied for other photoexcitations *incl.* singlet and triplet excitons in luminescence materials by site selective fluorescence and time resolved luminescence studies.¹⁰⁰ Herein, the time dependent relaxation of charge carriers is clearly observed in MDMO-PPV:PCBM mixture. A combined transient absorption and photo-CELIV experiment is proposed to gain more insight into dispersive relaxation processes.

Moreover, the photo-CELIV technique can be used for thin devices with only a few hundred nanometer thickness. This is a clear advantage as compared to the ToF technique, where the preparation of micrometer thick samples is problematic for several promising, but not easily processable materials. One class of such novel functional materials is the “double-cable” polymers. The charge transport studies using the photo-CELIV technique is proposed to accelerate the understanding of charge carrier mobility and recombination in these materials.

References

- [1] C. W. Tang, Two-layer organic photovoltaic cell, *Appl. Phys. Lett.*, **48**, 183 (1986).
- [2] H. Shirakawa, E. J. Louis, A. G. MacDiarmid, C. K. Chiang and A. J. Heeger, Synthesis of electrically conducting organic polymers: halogen derivatives of polyacetylene (CH)_x, *J. Chem. Soc. Chem. Comm.*, **16**, 578 (1977).
- [3] H. Tomozawa, D. Braun, S. Phillips and A. J. Heeger, Metal-polymer Schottky barriers on cast films of soluble poly(3-alkylthiophenes), *Synthetic Metals*, **22**, 63 (1987).
- [4] R. H. Friend, R. W. Gymer, A. B. Holmes, J. H. Burroughes, R. N. Marks, C. Taliani, D. D. C. Bradley, D. A. Dos Santos, J. L. Brédas, M. Lögdlund and W. R. Salaneck, Electroluminescence in conjugated polymers, *Nature*, **121**, 397 (1999).
- [5] Z. Bao, A. Dodabalapur and A. J. Lovinger, Soluble and processable poly(3-hexylthiophene) for thin films field-effect applications with high mobility, *Appl. Phys. Lett.*, **69**, 4108 (1996).
- [6] C. J. Brabec, N. S. Sariciftci and J. C. Hummelen, Plastic Solar Cells, *Adv. Funct. Mater.*, **11**, 15 (2001).
- [7] C. J. Brabec, F. Padinger, J. C. Hummelen, R. A. J. Janssen and N. S. Sariciftci, Realization of Large Area Flexible Fullerene – Conjugated Polymer Photocells: A route to plastic solar cells, *Synthetic Metals*, **102**, 861 (1999).
- [8] S. E. Shaheen, R. Radspinner, N. Peyghambarian, G. E. Jabbour, Fabrication of bulk heterojunction plastic solar cells by screen printing, *Appl. Phys. Lett.*, **79**, 2996 (2001).
- [9] T. Ishikawa, M. Nakamura, K. Fujita and T. Tsutsui, Preparation of organic bulk heterojunction photovoltaic cells by evaporative spray deposition from ultradilute solution, *Appl. Phys. Lett.*, **84**, 2424 (2004).
- [10] M. Pope and C. E. Swenberg, *Electronic Processes in Organic Crystals and Polymers*, Oxford University Press 2nd ed., New York, 1999.

-
- [11] *Primary photoexcitations in conjugated polymers: Molecular excitons versus semiconductor band model*, N. S. Sariciftci (ed), World Scientific, Singapore, 1997.
- [12] V. I. Arkhipov and H. Bässler, Exciton dissociation and charge photogeneration in pristine and doped conjugated polymers, *Phys. Stat. Sol. (a)*, **201**, 1152 (2004).
- [13] C. H. Lee, G. Yu, D. Moses, K. Pakbaz, C. Zhang, N. S. Sariciftci, A. J. Heeger and F. Wudl, Sensitization of the photoconductivity of conducting polymers by C60: Photoinduced electron transfer, *Phys. Rev. B*, **48**, 15425 (1993).
- [14] N. S. Sariciftci, L. Smilowitz, A. J. Heeger, F. Wudl, Photoinduced electron transfer from a conducting polymer to buckminsterfullerene, *Science*, **258**, 1474 (1992).
- [15] Dyakonov, G. Zorinants, M. Scharber, C. J. Brabec, R. A. J. Janssen, J. C. Hummelen and N. S. Sariciftci, Photoinduced charge carriers in conjugated polymer-fullerene composites studied with light-induced electron-spin resonance, *Phys. Rev. B*, **59**, 8019 (1999).
- [16] L. Smilowitz, N. S. Sariciftci, R. Wu, C. Gettinger, A. J. Heeger and F. Wudl, Photoexcitation spectroscopy of conducting-polymer-C60 composites: Photoinduced electron transfer, *Phys. Rev. B*, **47**, 13 835 (1993).
- [17] B. Kraabel, D. McBranch, N. S. Sariciftci, D. Moses and A. J. Heeger, Ultrafast spectroscopic studies of photoinduced electron transfer from semiconducting polymer to C60, *Phys. Rev. B*, **50**, 1854 (1994).
- [18] X. Wei, Z. V. Vardeny, N. S. Sariciftci and A. J. Heeger, Absorption-detected magnetic-resonance studies of photoexcitations in conjugated-polymer/C60 composites, *Phys. Rev. B*, **53**, 2187 (1996).
- [19] N. S. Sariciftci, D. Braun, C. Zhang, V. I. Srdanov, A. J. Heeger, G. Stucky and F. Wudl, Semiconducting polymer-buckminsterfullerene heterojunctions: Diodes, photodiodes, and photovoltaic cells, *Appl. Phys. Lett.*, **62**, 585 (1993).
- [20] N. S. Sariciftci and A. J. Heeger, Photophysics, Charge Separation and Device Applications of Conjugated Polymer/Fullerene Composites, in *Handbook of Conductive Molecules and Polymers*, H. S. Nalwa (Eds), Vol 1, John Wiley and Sons Ltd., 1997.

-
- [21] C. Waldauf, P. Schilinsky, J. Hauch and C. J. Brabec, Material and device concepts for organic photovoltaics: Towards competitive efficiencies, *Thin Solid Films*, **451-452**, 503 (2004).
- [22] S. A. Choulis, J. Nelson, Y. Kim, D. Poplavskyy, T. Kreouzis, J. R. Durrant and D. D. C. Bradley, Investigation of transport properties in polymer/fullerene blends using time-of-flight photocurrent measurements, *Appl. Phys. Lett.*, **83**, 3812 (2003).
- [23] W. Geens, T. Martens, J. Poortmans, T. Aernouts, J. Manca, L. Lutsen, P. Heremans, S. Borghs, R. Mertens and D. Vanderzande, Modelling the short-circuit current of bulk heterojunction solar cells, *Thin Solid Films*, **451-452**, 498 (2004).
- [24] V. D. Mihailetschi, J. K. J. van Duren, P. W. M. Blom, J. C. Hummelen, R. A. J. Janssen, J. M. Kroon, M. T. Rispens, W. J. H. Verhees and M. M. Wienk, Electron transport in a methanofullerene, *Adv. Func. Mater.*, **13**, 43 (2003).
- [25] S. A. Choulis, J. Nelson, S. M. Tuladhar, S. Cook, Y. Kim, J. R. Durrant and D. D. C. Bradley, Transport and recombination dynamics studies of polymer/fullerene based solar cells, *Macromol. Symp.*, **205**, 1 (2004).
- [26] N. A. Schultz, M. C. Scharber, C. J. Brabec and N. S. Sariciftci, Low-temperature recombination kinetics of photoexcited persistent charge carriers in conjugated polymer/fullerene composite films, *Phys. Rev. B*, **64**, 245210 (2001).
- [27] M. C. Scharber, C. Winder, H. Neugebauer and N. S. Sariciftci, Anomalous photoinduced absorption of conjugated polymer/fullerene mixtures at low temperatures and high frequencies, *Synthetic Metals*, **141**, 109 (2004).
- [28] C. Arndt, U. Zhokhavets, G. Bobsch, C. Winder, C. Lungenschmied, N. S. Sariciftci, Investigation of excited states in polymer/fullerene solar cells by means of photoinduced reflection- /absorption spectroscopy, *Thin Solid films*, **451 – 452**, 60 (2004).
- [29] I. Montanari, A. F. Nogueira, J. Nelson, J. R. Durrant, C. Winder, M. A. Loi, N. S. Sariciftci and C. J. Brabec, Transient optical studies of charge recombination dynamics in a polymer/fullerene composite at room temperature, *Appl. Phys. Lett.*, **81**, 3001 (2002).
- [30] A. F. Nogueira, I. Montanari, J. Nelson, J. R. Durrant, C. Winder, N. S. Sariciftci and C. J. Brabec, Charge recombination in conjugated polymer/fullerene blended films studied by transient absorption spectroscopy, *J. Phys. Chem. B*, **107**, 1567 (2003).

-
- [31] I. Riedel, J. Parisi, V. Dyakonov, L. Lutsen, D. Vanderzande and J. C. Hummelen, Effect of temperature and illumination on the electrical characteristics of polymer-fullerene bulk-heterojunction solar cells, *Adv. Func. Mater.*, **14**, 38 (2004).
- [32] S. E. Shaheen, C. J. Brabec, N. S. Sariciftci, F. Padinger, T. Fromherz and J. C. Hummelen, 2.5% efficient organic plastic solar cells, *Appl. Phys. Lett.*, **78**, 841 (2001).
- [33] T. Martens, J. D'Haen, T. Munters, Z. Beelen, L. Goris, J. Manca, M. D'Olieslaeger, D. Vanderzande, L. De Schepper and R. Andriessen, Disclosure of the nanostructure of MDMO-PPV:PCBM bulk hetero-junction organic solar cells by a combination of SPM and TEM, *Synthetic Metals*, **138**, 243 (2003).
- [34] J. K. J. van Duren, X. Yang, J. Loos, C. W. T. Bulle-Lieuwma, A. B. Sieval, J. C. Hummelen and R. A. J. Janssen, Relating the morphology of Poly(*p*-phenylene vinylene)/methanofullerene blends to solar-cell performance, *Adv. Funct. Mater.*, **14**, 425 (2004).
- [35] H. Hoppe, M. Niggemann, C. Winder, J. Kraut, R. Hiesgen, A. Hinsch, D. Meissner and N. S. Sariciftci, Nanoscale morphology of conjugated polymer/fullerene-based bulk-heterojunction solar cells, *Adv. Funct. Mater.*, **14**, 1005 (2004).
- [36] T. Martens, Z. Beelen, J. D'Haen, T. Munters, L. Goris, J. Manca, M. D'Olieslaeger, D. Vanderzande, L. De Schepper and R. Andriessen, Morphology of MDMO-PPV:PCBM bulk heterojunction organic solar cells studied by AFM, KFM, and TEM, *Proc. of SPIE*, Vol. 4801 (2002).
- [37] A. Cravino and N. S. Sariciftci, Double-cable polymers for fullerene based organic optoelectronic applications, *J. Mater. Chem.*, **12**, 1931 (2002), and references therein
- [38] A. Cravino and N. S. Sariciftci, Molecules as bipolar conductors, *Nature Materials*, **2**, 360 (2003).
- [39] C. Winder and N. S. Sariciftci, Low bandgap polymers for photon harvesting in bulk heterojunction solar cells, *J. Mater. Chem.*, **14**, 1077 (2004).
- [40] P. M. Borsenberger and D. S. Weiss, *Organic Photoreceptors for Xerography*, Marcel Dekker, Inc., New York, 1998.
- [41] L. B. Schein, Temperature independent drift mobility along the molecular direction of As₂S₃, *Phys. Rev. B*, **15**, 1024 (1977).

-
- [42] H. Scher and E. W. Montroll, Anomalous transit-time dispersion in amorphous solids, *Phys. Rev. ,B* **12**, 2455 (1975).
- [43] W. D. Gill, Drift mobilities in amorphous charge-transfer complexes of trinitrofluorenone and poly-*n*-vinylcarbazole, *J. Appl. Phys.*, **43**, 5033 (1972).
- [44] A. Peled and L. B. Schein, Hole mobilities that decrease with increasing electric fields in a molecularly doped polymer, *Chem. Phys. Lett.*, **153**, 422 (1988).
- [45] M. Novo, M. van der Auweraer, F. C. DeSchuyver, P.M. Borsenberger and H. Bässler, Anomalous field dependence of the hole mobility in a molecular doped polymer, *Phys. Stat. Sol. (b)*, **177**, 223 (1993).
- [46] H. Kageyama, K. Ohnishi, S. Nomura and Y. Shirota, Negative electric-field dependence of hole mobility for a molecular glass of tri(*o*-terphenyl-4-yl) amine, *Chem. Phys. Lett.*, **277**, 137 (1997).
- [47] H. Bässler, Charge transport in disordered organic photoconductors, *Phys. Stat. Sol. (b)*, **175**, 15 (1993).
- [48] A. Miller and E. Abrahams, Impurity Conduction at Low Concentrations, *Phys. Rev.* **120**, 745 (1960).
- [49] B. Movaghar, M. Grünewald, B. Ries, H. Bässler and D. Würtz, Diffusion and relaxation of energy in disordered organic and inorganic materials, *Phys. Rev. B*, **33**, 5545 (1986).
- [50] L. Pautmeier, R. Richert and H. Bässler, Hopping in a Gaussian distribution of energy states: transition from dispersive to non-dispersive transport, *Phil. Mag. Lett.*, **59**, 325 (1989).
- [51] C. Im, H. Bässler., H. Rost and H. H. Hörhold, Hole transport in polyphenylene vinylene-ether under bulk photoexcitation and sensitized injection, *J. Chem. Phys.*, **113**, 3802 (2000).
- [52] H. C. F. Martens, P. W. M. Blom and H. F. M. Schoo, Comparative study of hole transport in poly(p-phenylene vinylene) derivatives, *Phys. Rev. B*, **61**, 7489 (2000).
- [53] A. J. Heeger, S. Kivelson, J. R. Schrieffer and W. P. Su, Solitons in Conductive Polymers, *Rev. Mod. Phys.*, **60**, 781 (1988).

-
- [54] G. H. Gelinck, J. M. Warman and G. J. Staring, Polaron pair formation, migration, and decay on photoexcited poly(phenylenevinylene) chains, *J. Phys. Chem.* **100**, 5485 (1996).
- [55] H. Bässler, Charge transport in random organic semiconductors, in *Semiconducting Polymers: Chemistry, Physics and Engineering*; G. Hadziioannou, P. F. van Hutten, (Eds), Wiley VCH, Weinheim 2000.
- [56] S. Nagamatsu, S. S. Pandey, W. Takashima, T. Endo, M. Rikukawa and K. Kaneto, Photocurrent transport in processable poly(3-alkylthiophene), *Synthetic Metals*, **121**, 1563 (2001).
- [57] T-A. Chen, X. Wu and R. D. Rieke, Regiocontrolled synthesis of poly(3-alkylthiophenes) mediated by Rieke Zinc: Their characterization and solid-state properties, *J. Am. Chem. Soc.*, **117**, 233 (1995).
- [58] H. Sirringhaus, P. J. Brown, R. H. Friend, M. M. Nielsen, K. Bechgaard, B. M. W. Langeveld-Voss, A. J. H. Spiering, R. A. J. Janssen, E. W. Meijer, P. Herwig and D. M. de Leeuw, Two-dimensional charge transport in self-organized, high mobility conjugated polymers, *Nature* **401**, 685 (1999).
- [59] R. Österbacka, A. Pivrikas, G. Juška, K. Genevičius, K. Arlauskas and H. Stubb, Mobility and density relaxation of photogenerated charge carriers in organic materials, *Curr. Appl. Phys.*, **4**, 534 (2004).
- [60] D. Moses, J. Wang, G. Yu and A. J. Heeger, Temperature-independent photoconductivity in thin films of semiconducting polymers: Photocarrier sweep-out prior to deep trapping, *Phys. Rev. Lett.*, **80**, 2685 (1998).
- [61] C. Melzer, E. J. Koop, V. D. Mihailetschi and P. W. M. Blom, Hole transport in poly(phenylene vinylene)/Methanofullerene bulk-heterojunction solar cells, *Adv. Funct. Mater.*, **14**, 865 (2004).
- [62] G. Juška, K. Arlauskas, M. Viliūnas and J. Kočka, Extraction current transients: A new method of study of charge transport in microcrystalline silicon, *Phys. Rev. Lett.*, **84**, 4946 (2000).
- [63] N. F. Mott and E. A. Davis, *Electronic processes in non-crystalline materials*, Clarendon Press, Oxford, 1971.

-
- [64] R. Menon, C. O. Yoon, D. Moses and A. J. Heeger, Metal-Insulator transition in doped conducting polymers, in *Handbook of conducting polymers*, T. A. Skotheim, R. L. Elsenbaumer, J. R. Reynolds (Eds), Marcel Dekker, Inc., New York, 1998.
- [65] C. D. Dimitrakopoulos and P. R. L. Malenfant, Organic thin films transistors for large area electronics, *Adv. Mater.*, **14**, 99 (2002) and ref. therein.
- [66] M. A. Lampert and P. Mark, *Current Injection in Solids*, Academic Press, New York, 1970.
- [67] D. Poplavskyy and J. Nelson, Nondispersive hole transport in amorphous films of methoxy-spirofluorene-arylamine organic compounds, *J. Appl. Phys.*, **93**, 341 (2003).
- [68] P. W. M. Blom, M. C. J. M. Vissenberg, Dispersive hole transport in poly(*p*-phenylene vinylene), *Phys. Rev. Lett.*, **80**, 3819 (1998).
- [69] P. W. M. Blom, M. J. M. de Jong and J. J. M. Vleggaar, Electron and hole transport in poly(*p*-phenylene vinylene) devices, *Appl. Phys. Lett.*, **68**, 3308 (1996).
- [70] M. Redecker, H. Bässler and H. H. Hörhold, Determination of the hole mobility in organic light emitting diodes via transient absorption, *J. Phys. Chem. B*, **101**, 7398 (1997).
- [71] M. Redecker and H. Bässler, Optical detection of charge carriers in organic light-emitting diodes, *Appl. Phys. Lett.*, **69**, 70 (1996).
- [72] G. Juška, K. Genevičius, K. Arlauskas, R. Österbacka and H. Stubb, Charge transport at low electric fields in π -conjugated polymers, *Phys. Rev. B* **65**, 233208 (2002).
- [73] G. Juška, K. Arlauskas, M. Viliūnas, K. Genevičius, R. Österbacka and H. Stubb, Charge transport in π -conjugated polymers from extraction current transients, *Phys. Rev. B*, **62**, R16 235 (2000).
- [74] M. M. Erwin, J. McBride, A. V. Kadavanich and S. J. Rosenthal, Effects of impurities on the optical properties of poly-3-hexylthiophene thin films, *Thin Solid Films*, **409**, 198 (2002).
- [75] L. Lutsen, P. Adriaensens, H. Becker, A. J. van Breemen, D. Vanderzande and J. Gelan, New synthesis of a soluble high molecular weight poly(arylene vinylene): Poly[2-methoxy-5-(3,7-dimethyloctyloxy)-*p*-phenylene vinylene]. Polymerization and device Properties, *Macromolecules*, **32**, 6517 (1999).

-
- [76] A. J. Mozer, P. Denk, M. C. Scharber, H. Neugebauer, N. S. Sariciftci, P. Wagner, L. Lutsen and D. Vanderzande, Novel regiospecific MDMO-PPV copolymer with improved charge transport for bulk heterojunction solar cells, *J. Phys. Chem. B*, **108**, 5235 (2004).
- [77] S. Luzzati, A. J. Mozer, P. Denk, M. C. Scharber, M. Catellani, N. O. Lupsac, F. Giacalone, J. L. Segura, N. Martin, H. Neugebauer and N. S. Sariciftci, Tuning of the photoinduced charge transfer process in donor-acceptors “double cable” copolymers, *Organic Photovoltaics IV.*, Z. H. Kafafi, P. A. Lane (eds), Proceedings of the SPIE, Vol. 5215 41 (2004).
- [78] A. Cravino, H. Neugebauer, S. Luzzati, M. Catellani, A. Petr, L. Dunsch and N. S. Sariciftci, Positive and negative charge carriers in doped or photoexcited polydithienothiophenes: A comparative study using Raman, infrared and electron spin resonance spectroscopy, *J. Phys. Chem. B*, **106**, 3583 (2002).
- [79] M. Catellani, B. Boselli, S. Luzzati and C. Tripodi, Dithienothiophene and dithienothiophene-S,S-dioxide copolymers for photovoltaics, *Thin Solid Films*, **403-404**, 66 (2002).
- [80] B. D. Reeves, C. R. G. Grenier, A. A. Argun, A. Cirpan, T. D. McCarley and J. R. Reynolds, Spray Coatable Electrochromic Dioxythiophene Polymer with High Coloration efficiencies, in press.
- [81] A. J. Mozer, P. Denk, M. C. Scharber, H. Neugebauer, N. S. Sariciftci, P. Wagner, L. Lutsen, D. Vanderzande, A. Kadashchuk, R. Staneva and R. Resel, Novel Regiospecific MDMO-PPV Polymers with Improved Charge Transport Properties for Bulk Heterojunction Solar Cells, *Synthetic Metals*, submitted 2004.
- [82] T.-Q. Nguyen, J. B. Schwartz, R. D. Schaller, J. C. Johnson, L. F. Lee, L. H. Haber and R. J. Saykally, Near-field scanning optical microscopy (NSOM) studies of the relationship between interchain interactions, morphology, photodamage, and energy transport in conjugated polymer films, *J. Chem. Phys.*, **110**, 4068 (1999).
- [83] A. Kadashchuk, Y. Skryshevski, Y. Piryatinski, A. Vakhnin, E. V. Emelianova, V. I. Arkhipov and H. Bässler, Thermally stimulated photoluminescence in poly(2,5-dioctyloxy p-phenylene vinylene), *J. Appl. Phys.*, **91**, 5016 (2002).

-
- [84] F. Padinger, R. S. Rittberger and N. S. Sariciftci, Effects of Postproduction Treatment on Plastic Solar Cells, *Adv. Funct. Mater.*, **13**, 1 (2003).
- [85] P. Schilinsky, C. Waldauf and C. J. Brabec, Recombination and loss analysis in polythiophene based bulk heterojunction photodetectors, *Appl. Phys. Lett.*, **81**, 3885 (2002).
- [86] M. S. A. Abdou, F. P. Orfino, Z. W. Xie, M. J. Deen and S. Holdcroft; Reversible charge transfer complexes between molecular oxygen and poly(3-alkylthiophene)s, *Adv. Mater.*, **6**, 838 (1994).
- [87] S. Hoshino, M. Yoshida, S. Uemura, T. Kodzasa, N. Takada, T. Kamata and K. Yase, Influence of moisture on device characteristics of polythiophene-based field-effect transistors, *J. Appl. Phys.*, **95**, 5088 (2004).
- [88] V. I. Akhipov and A. I. Rudenko, *Philos. Mag. B* **45**, 18 (1982).
- [89] P. M. Borsenberger, R. Richert and H. Bässler, Dispersive and nondispersive charge transport in a molecularly doped polymer with superimposed energetic and positional disorder, *Phys. Rev. B*, **47**, 4289 (1993).
- [90] I. I. Fishchuk, A. Kadashchuk, H. Bässler and M. Abkowitz, Low field charge-carrier hopping transport in energetically and positionally disordered organic materials, *Phys. Rev. B*, submitted 2004.
- [91] A. J. Mozer and N. S. Sariciftci, Negative electric field dependence of charge carrier drift mobility in conjugated, semiconducting polymers, *Chem. Phys. Lett.*, **389**, 438 (2004).
- [92] S. S. Pandey, W. Takashima, S. Nagamatsu, T. Endo, M. Rikukawa and K. Kaneto, Regioregularity vs Regiorandomness: effect of photocarrier transport in poly(3-hexylthiophene), *Jpn. J. Appl. Phys.*, **39**, 94 (2000).
- [93] A. Hirao, H. Nishizawa and M. Sugiuchi, Diffusion and drift of charge carriers in molecularly doped polymers, *Phys. Rev. Lett.*, **75**, 1787 (1995).
- 94 G. Juška, N. Nekrasas, K. Genevicius, J. Stuchlik and J. Kocka, Relaxation of photoexcited charge carrier concentration and mobility in $\mu\text{c-Si:H}$, *Thin Solid films*, **451-452**, 290 (2004).

-
- [95] K. Kaneto, K. Hatae, S. Nagamatsu, W. Takashima, S. S. Pandey, K. Endo, and M. Rikukawa, Photocarrier mobility in regioregular poly(3-hexylthiophene) studied by the time of flight method, *Jpn. J. Appl. Phys.*, **38**, 1188 (1999).
- [96] A. J. Mozer, N. S. Sariciftci, A. Pivrikas, R. Österbacka, G. Juška and H. Bässler, Charge carrier mobility in regioregular poly(3-hexylthiophene) probed by transient conductivity techniques: A comparative study, *Phys. Rev. B*, accepted November 2004.
- [97] J. Nelson, Diffusion-limited recombination in polymer-fullerene blends and its influence on photocurrent collection, *Phys. Rev. B*, **67**, 155209 (2003).
- [98] H. Hoppe, N. Arnold, D. Meissner and N. S. Sariciftci, Modeling of optical absorption in conjugated polymer/fullerene bulk heterojunction plastic solar cells, *Thin Solid Films*, **451-452**, 589 (2004).
- [99] P. Schilinsky, C. Waldauf, J. Hauch and C. J. Brabec, Simulation of light intensity dependent current characteristics of polymer solar cells, *J. Appl. Phys.*, **95**, 2816 (2004).
- [100] M. Scheidler, B. Cleve, H. Bässler and P. Thomas, Monte Carlo simulation of bimolecular exciton annihilation in an energetically random hopping system, *Chem. Phys. Lett.*, **225**, 431 (1994).

APPENDIX

Curriculum Vitae

Attila Janos Mozer

Nationality: Hungarian
Date of Birth: 20th of January in 1977

January 2002 –December 2004 PhD studies at Linz Institute for Organic Solar Cells,
Johannes Kepler University Linz

September 1995 - February 2002 Master Degree in Chemical Engineering,
Department of Plastics and Rubber Technology,
Faculty of Chemical Engineering, Budapest
University of Technology and Economics

Scholarships:

2000-2001 Master Thesis at Osaka University, Japan,
Faculty of Applied Chemistry,
supervisor: Professor Y. Shirota

1999-2000 University of New Hampshire, USA

Professional Experiences:

2002- 2003 Konarka Austria GmbH, young researcher
position within the EUROMAP network

PUBLICATIONS:**Pier Reviewed inc. accepted:**

1. Attila J. Mozer, Patrick Denk, Markus C. Scharber, Helmut Neugebauer, N. Serdar Sariciftci, Pawel Wagner, Laurence Lutsen and Dirk Vanderzande, *Novel Regiospecific MDMO-PPV Copolymer with Improved Charge Transport for Bulk Heterojunction Solar Cells*, J. Phys. Chem. B, **108**, 5235, 2004.

2. Attila J. Mozer and Niyazi Serdar Sariciftci, *Negative electric Field Dependence of Charge carrier Drift Mobility in Conjugated, Semiconducting Polymers*, Chem. Phys. Lett., **389**, 438, 2004.

3. Attila J. Mozer, Niyazi Serdar Sariciftci, Almantas Pivrikas, Ronald Österbacka, Gytis Juška and Heinz Bässler, *Charge carrier mobility in regioregular poly(3-hexylthiophene) probed by transient conductivity techniques: A comparative study*, Physical Review B, accepted: November, 2004.

Submitted:

1. Attila J. Mozer, N. S. Sariciftci, L. Lutsen, D. Vanderzande, G. Juška, R. Österbacka, *Charge carrier transport and recombination in bulk heterojunction solar cells studied by the Photo-CELIV technique*, Appl. Phys. Lett. submitted: September 2004.

Conference Proceedings:**Published:**

1. S. Luzzati, A. J. Mozer, P. Denk, M. C. Scharber, M. Catellani, N. O. Lupsac, F. Giacalone, J. L. Segura, N. Martin, H. Neugebauer and N. S. Sariciftci, Tuning of the

photoinduced charge transfer process in donor-acceptors “double cable” copolymers, *Organic Photovoltaics IV.*, Z. H. Kafafi, P. A. Lane (eds), Proceedings of the SPIE, Vol. 5215 41 (2004).

Submitted:

1. A. J. Mozer and N. S. Sariciftci, Polymer based photovoltaic materials and devices, Proceedings of the IPS-15 Conference, Paris.
2. A. J. Mozer, P. Denk, M. C. Scharber, H. Neugebauer, N. S. Sariciftci, P. Wagner, L. Lutsen, D. Vanderzande A. Kadashchuk, Rosina Staneva, Roland Resel *Novel Regiospecific MDMO-PPV Polymers with Improved Charge Transport Properties for Bulk Heterojunction Solar Cells*, Synthetic Metals, submitted: July 2004.

CONFERENCE ATTENDANCE:

Upcoming:

November 2004: MRS Meeting in Boston, USA

Oral Presentation: Negative Electric Field Dependence of Charge Carrier Mobility in Regioregular Poly(3-hexylthiophene) Probed by Transient Conductivity Techniques.

Past:

June 2004: International Conference on Synthetic Metals (ICSM 2004), Wollongong, Australia

Oral Presentation: A Novel Regiospecific MDMO-PPV Copolymer with Improved Charge Transport for Bulk Heterojunction Solar Cells.

Poster Presentation: Negative Electric Field Dependence of the Mobility of Photoinduced Charge Carriers in Regioregular Poly(3-hexylthiophene).

2004 May: 205th Annual Meeting of the Electrochemical Society, San Antonio, USA

Oral Presentation: Negative Electric Field Dependence of the Mobility of Photoinduced Charge Carriers in Regioregular Poly(3-hexylthiophene).

October 2003: ECOER'03 Imperial Collage, London

Oral Presentation: Synthesis and Characterization of Novel Regiospecific MDMO-PPV Copolymer with Improved Charge Transport.

SCHOOLS:

February 2004: Winterschool on Organic Electronics (OEWS'04), Donnersbach, Austria.

September 2003: 2003 European Summerschool on Quantum Solar Energy Conversion, Hirschegg, Austria.

March 2002: Alan J. Heeger's Lectures Physics and Chemistry of Conjugated Polymers, Kirchberg, Austria